A Novel Microfluidic Ultrasonic Flow Rate Sensor for Wearable Sweat Sensing

TU Delft

Rens Ursem

A novel microfluidic ultrasonic flow rate sensing modality for wearable sweat sensing

Rens F. R. Ursem

A thesis presented for the degree of
Master Biomedical Engineering
Track: Medical Devices

Student number:	5092655	
Project duration:	February – December, 2024	
Research group:	Electronic Instrumentation	
Graduation committee:	Dr. ir. A. Bossche,	TU Delft, supervisor
	Prof. P. J. French,	TU Delft
	Dr. ir. A. S. M. Steijlen,	TU Delft
	Ing. J. Bastemeijer,	TU Delft
	Assoc. Prof. M. K. Ghatkesar,	TU Delft

Cover: The Ripple Effect - The Savvy Director

"Let's first build on existing knowledge and then find out what we did wrong."

R.B.H. de Zeeuw

Dedicated to my grandfather.

Acknowledgements

I would like to extend my thanks to Andre Bossche, Jeroen Bastemeijer, and Annemarijn Steijlen for their supervision, insightful discussions, and guidance, which helped me enhance both my engineering and academic skills throughout this project.

I am also grateful to Paddy French for chairing my defense, and to Murali Ghatkesar for his interest in the project and his role on my committee.

A special thanks goes to Guillermo Presa Magriña for generously providing his 3D printing setup, even without prior acquaintance. His printer significantly accelerated my progress and allowed for rapid prototyping, offering a level of freedom I deeply appreciate.

Lastly, I want to express my sincere gratitude to Robbert Nederhoff for being an exceptional colleague and a true pleasure to work with throughout this journey.

Rens Ursem
Delft, December 2024

Summary

This thesis explores the development of a novel platform for reliable sweat rate measurements, which are crucial for maximising the potential of sweat analysis. Accurate sweat rate measurements allow for the compensation of sweat rate effects on the sweat matrix and have significant clinical relevance. The initial sections cover the physiology of sweat to highlight the importance of sweat rate, followed by a review of existing wearable flow rate sensing methods.

The research that follows focuses on designing a cost-efficient microfluidic flow rate sensor, introducing an innovative resonance-based weighting concept. The prototype integrates an off-the-shelf piezoelectric sensor with a 3D-printed microfluidic structure and double-sided adhesive. The 3D-printed design is further optimised to enhance sensor performance. Additional design elements, like a wick and vent, are investigated to facilitate sample renewal and reservoir drainage whilst preventing leakage.

The system demonstrates a frequency shift proportional to flow rate, with testing performed using a syringe pump. By artificially inducing sweat, on-body sweat rate measurements were performed with the sensor's results closely aligning with the reference measurements. This work advances the field of wearable sensing technologies by presenting an innovative piezoelectric-based flow rate sensor for sweat analysis, demonstrating its feasibility and emphasising its potential for future development.

Contents

Acknowledgements ii

Summary iii

1 Introduction 1
- 1.1 Sweat Physiology . . . 2
  - 1.1.1 An introduction to the sweat gland . . . 2
  - 1.1.2 Sweat mechanism . . . 3
  - 1.1.3 Sweat Topology . . . 4
  - 1.1.4 Sweat stimulation . . . 6
- 1.2 Microfluidic sweat rate sensors . . . 6
  - 1.2.1 Relevance of sweat rate . . . 6
  - 1.2.2 Filling Principles . . . 9
  - 1.2.3 State-of-the art flow rate sensors for sweat . . . 12

2 Requirements & criteria 18
- 2.1 Scope . . . 18
- 2.2 Requirements . . . 19
- 2.3 Criteria . . . 21
  - 2.3.1 Criteria weighting . . . 22

3 Concept selection 24
- 3.1 Concepts and criteria scoring . . . 24
  - 3.1.1 Capacitive moisture gradient with evaporation interface . . . 24
  - 3.1.2 Compartment filling . . . 25
  - 3.1.3 Resonance weighing . . . 26
  - 3.1.4 Result of scoring . . . 27
  - 3.1.5 Concept development . . . 27

4 Theoretical Framework 29
- 4.1 Introduction . . . 29
- 4.2 Microfluidics . . . 29
  - 4.2.1 Transport in a microfluidic channel . . . 29
  - 4.2.2 Promoting and directing flow in a channel . . . 30
- 4.3 Piezoelectric sensors . . . 31
  - 4.3.1 The piezoelectric effect . . . 31
  - 4.3.2 Resonance behaviour . . . 31

4.3.3 The quartz crystal microbalance . . . 32

5 Experimental embodiment 37
5.1 3D printing . . . 37
5.2 Sensor selection and characterisation . . . 39
5.2.1 Integration of microfluidic structure . . . 41
5.3 Design iterations: sensing area . . . 43
5.3.1 Measurement protocol . . . 45
5.3.2 Optimisation methods . . . 47
5.3.3 Optimisation results . . . 49
5.3.4 Channel Resettability: Wick concept . . . 51
5.3.5 Multiflow measurements and reproducibility . . . 54
5.3.6 Discussion . . . 54
5.4 Wearable development: collection area . . . 56
5.4.1 Basis design . . . 56
5.4.2 Results . . . 58

6 Characterisation and analysis algorithm 60
6.1 Development of characterisation and flow rate estimation algorithm . . . 60
6.1.1 Characterisation algorithm . . . 60
6.1.2 Flow rate estimation algorithm . . . 64

7 Wearable Testing of Prototype 67
7.1 Wearable Testing . . . 67
7.1.1 Methods . . . 67
7.1.2 Final iterations . . . 67
7.1.3 Results . . . 69
7.1.4 Discussion . . . 71

8 Conclusion 73

9 Future Outlook 74
9.1 Further development . . . 74
9.1.1 Resonance weighing as a flow rate sensing modality . . . 75
9.2 Other applications . . . 75

Appendix A Concept scoring 76
A.1 Concept Scoring . . . 76
A.1.1 Capacitive moisture gradient with evaporation interface . . . 76
A.1.2 Compartment filling . . . 77
A.1.3 Resonance weighing . . . 78

Appendix B Preliminary testing 81
B.1 Contact Angles . . . 81
B.2 Printing set-up . . . 82
B.3 CUSA sensor . . . 83

Appendix C Testing with microfluidic substrates **85**
C.1 Orientation dependency filling 85
C.2 Day-to-day variation 86
C.3 Scale test results 86
C.4 Qualitative dynamic system model 87
C.5 Teeth design experiment 89

Appendix D Towards a wearable sensor **90**
D.1 Raw data 90
D.2 Capillary effect in resin 92
D.3 Iontophoresis protocol 93
D.4 Smoothing 94
D.5 Sigmoid fit 95
D.6 Flow rate assessment 96
D.7 Flow rate estimates on existing data 97

Chapter 1

Introduction

This chapter will contain (adapted) excerpts from a review:
"Worth Your Sweat: Wearable Microfluidic Flow Rate Sensors for Meaningful Sweat Analytics" R. Ursem, A. Steijlen, M. Parrilla, J. Bastemeijer, A. Bossche and K. De Wael, Lab on a Chip, "under review".

These parts are reproduced, because they provide a good introduction in the sweat rate sensing and will be marked by a coloured outline.

Wearable sweat sensors can provide a non-invasive, continuous method of monitoring health [1, 2]. This is because sweat can be easily collected from the skin for drug monitoring and physiological analysis [3, 4, 5, 6, 7]. The non-invasive nature of sweat sensing facilitates greater patient comfort, as it reduces the need for invasive blood analysis. Using sweat for analysis can also enable decentralised monitoring of patients in the clinic and at home.
Various types of sensors have been used for the analysis of the composition of sweat. Among them, colorimetric sensors and electrochemical sensors have been widely used due to their miniaturisation-ability and simplicity [2, 8, 9, 10, 11]. With the use of electrochemical sensors, sweat can be swiftly analysed after collection using techniques such as potentiometry and voltammetry. However, electrochemical measurements can be difficult to interpret due to the susceptibility to irregular flow rates, interferents, pH, or temperature, which might alter the analytical output of the sensors. On the other side, colorimetric sensors might be susceptible to subjective interpretation and varying light conditions (when not employing standardisation conditions) [12, 13].
While non-invasive health monitoring has attractive prospects, first, wearable sweat sensors have to face several multidisciplinary challenges in their development. These challenges include mechanical, chemical and electronic engineering principles. For example, the devices have to ensure wearer comfort and excellent contact for collection, often by matching the skin's elastic properties. Besides, wearable sweat sensors require microfluidics to handle small volumes due to the low perspiration rates. All the while, the sensors must offer great sensitivity to the target analyte, which is usually only present in low concentrations, and they must be robust in the presence of interferents [2].
Relative to other biofluids for analytical purposes, sweat itself actually has quite a suitable matrix [2]. Sweat, however, does not have a constant composition. Rather, its contents

vary according to the sweat rate. The sweat rate varies per person based on age, diet, sex, ethnicity and environment [14]. The natural sweating response can vary within a person depending on the state of physical activity, psychogenic stress and body location [15]. Even when sweating is artificially stimulated, the sudomotor response varies between individuals. This is important to consider since sweat rate can influence the concentration of the analyte in sweat. Normalising for sweat rate can account for this variability. Sweat rate sensors thus play a critical role in developing a platform for monitoring biomarkers or (therapeutic) drugs in sweat.

1.1 Sweat Physiology

The production of sweat and the variables determining the sweat contents will be discussed here to understand the challenge of sweat diagnostics and relevance of including sweat rate in it. Sweating mainly serves as thermoregulation by evaporating from the skin, as when one is exposed to physical exercise or hot environments [16], but sweat glands can also be activated when exposed to psychogenic stresses [15]. Most importantly, some constituents of sweat can be adopted for sweat-based diagnostics. The chloride (Cl^-) content of sweat is a well-known biomarker for cystic fibrosis, for instance [16]. However, many other potential biomarkers and medicines could be monitored in sweat with further research, as will be discussed later. First, the type of sweat glands will be explained.

1.1.1 An introduction to the sweat gland

The human body showcases three types of sweat glands: eccrine, apocrine and apoeccrine sweat glands [16]. Eccrine sweat glands have the highest prevalence on the body, covering nearly the entire surface of the body. They also secrete the highest volume of sweat directly out of the skin, consisting predominantly of water with NaCl as their major solute [17]. Apocrine sweat glands are only located at specific parts such as in the axillary, areolar and perineal regions. They start to function under the influence of sex hormones during puberty. These glands produce viscous, lipid-rich sweat, also containing proteins, sugar and ammonia. Upon breakdown by bacteria, this sweat becomes malodorous. Moreover, the apocrine gland is larger than the eccrine gland and its duct does not open to the epidermis directly. Rather, the duct leads to a hair follicle. It is thought that these glands are scent glands for pheromone production, although this trait is now rudimentary [16].

A third, 'hybrid' type of sweat gland also exists, which is the apoeccrine sweat gland and they share properties with both eccrine and apocrine glands. They are intermediate in size and resemble eccrine glands in that they secrete sweat directly onto the skin surface. They develop from eccrine sweat glands between the ages of 8-14 years and by the age of 16-18 they can constitute up to 45% of the total axillary glands. The apoeccrine are also similar to eccrine glands in their secreted contents, namely in that they produce an abundance of salt water secretions. However, because these glands are located in the axillary region, which is inefficient for evaporation, they are unlikely to significantly contribute to thermoregulation [16].

1.1.2 Sweat mechanism

Figure 1.1 shows the anatomy of an eccrine sweat gland and the sweating mechanism. The eccrine sweat gland consists of a secretory coil in the dermis, where the primary sweat is produced. Hereafter, the coil leads to a duct which plays a role in the resorption of salts. Distally, the ducts terminates into a pore in the stratum corneum. The secretory coil consists of three cell types: clear, dark and myoepithelial cells. The clear cells in Figure 1.1 secrete the primary sweat, nearly isotonic with blood plasma. Na-K ATPase activity is high in these cells to maintain a difference in osmolarity between the lumen of the sweat duct and the surrounding, apical cells. This active process is essential to promote an influx of water into the coil through osmosis [16, 18]. While their function is not well understood, dark cells might have a regulatory function for clear cells and support duct cell function as well [16]. However, they could potentially act as clear cells themselves [18]. The myoepithelial cells serve as structural support against the hydrostatic pressure exerted by the produced sweat [16].

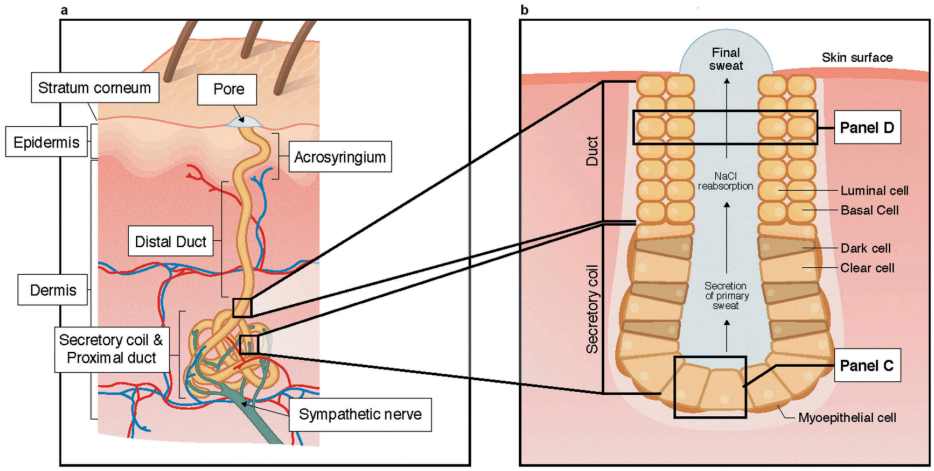

Figure 1.1: a. Schematic view of the anatomy of an eccrine sweat gland. b. Closer view of the sweat gland at the cellular level. Reprinted from [16]

The physiological process of sweat generation and secretion can be summarised in three phases:

1. The signal

Signals from the central nervous system reach the sympathetic cholinergic nerve endings innervating the sweat gland coil. The production of sweat is mediated by the neurotransmitter acetylcholine.

2. The secretion

Upon binding of a stimulative compound, an influx of K^+ and Cl^- ions occurs in the lumen of the secretory coil. The clear cells start to drain as they now become hypotonic. This triggers Na-K-2Cl cotransport and Na-K ATPase on the basolateral membrane, as well as Na^+ efflux through the apical membrane. Consequently, the Cl^- efflux provides an electrochemical gradient for the migration of Na^+. As a result, water fills the coils to equilibrate: primary sweat. This preliminary fluid then starts to fill the duct [16, 18].

Analyte	Sweat concentration (mmol/L)
Sodium	10 - 90
Chloride	10 - 90
Potassium	2 - 8
Lactate	5 - 40
Urea	4 - 12
Glucose	0.01 - 0.20
Bicarbonate	0.5 - 5.0
Ammonia	1 - 8

Table 1.1: Typical concentration of sweat constituents [16].

3. The reabsorption
The proximal part of the duct is predominantly where the resorption takes place. Without resorption, the large volumes of sweat which are used for thermoregulation, would cause a rapid loss of electrolytes. Hence, to retain electrolytes, Na^+ and Cl^- are actively reabsorbed once the primary sweat is forced up from the coil into the sweat ducts through osmotically induced pressure. The reabsorption is managed by two channel types: the epithelial sodium channel for sodium (ENaC) and the cystic fibrosis (CF) transmembrane regulator (CFTR) for chloride. Interestingly, the rate of Na^+ and Cl^- is flow dependent in such fashion that higher sweat rates have proportionally lower reabsorption rates, which produces a higher final electrolyte content [18].

Finally, the sweat reaches the end of the duct at the skin's surface, where it evaporates for its cooling effect. Yet, it can also be re-absorbed into dry skin. The pressure generated in the sweat gland is estimated at around 70kPa [18]. Through the Young-Laplace equation **??**, it is calculated that with this pressure, one could push sweat through even a super-hydrophobic pore with a diameter of 4 μm [18]. Typical sweat rates range from 0.12 μL/cm^2/min up to around 1 μL/cm^2/min [15]. Interestingly, the flow from a single sweat gland is thought not to be constant. Rather, it delivers sweat in a pulsating manner [18], and the activity of a sweat gland varies with body region, as will be discussed in the next section (See Figure1.3). Typical ranges have been determined for the (ionic) contents of sweat, which can be seen in Table 1.1.

1.1.3 Sweat Topology

Not only is there a difference in sweat secretion under various conditions (rest versus exercise), the amount of sweat secretion is also influenced by the skin location. The distribution of the sweat glands is far from homogenuous between different body regions. Gland densities vary from 16 to 530 glands per cm^2 per region [17, 15]. In total, a person has 2 to 4 million sweat glands.

The part of the body with the highest amount of sweat gland is the hands and feet, with the digits having the highest local density, as seen in Figure 1.2. The arms, back and forehead have approximately the same gland densities, standing at 4 times less than fingers. However, also the sweat *rates* can differ per region. In the resting and active state, the buttocks, legs and back have the highest output per gland, see Figure 1.3.

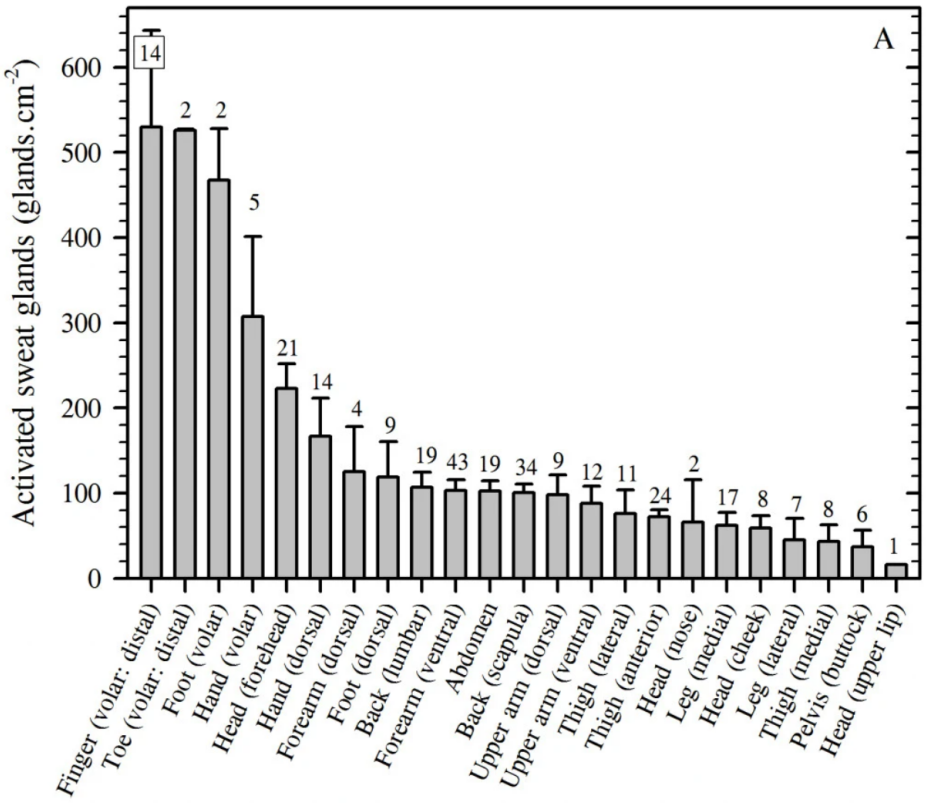

Figure 1.2: Amount of active glands per body region. Reprinted from [15].

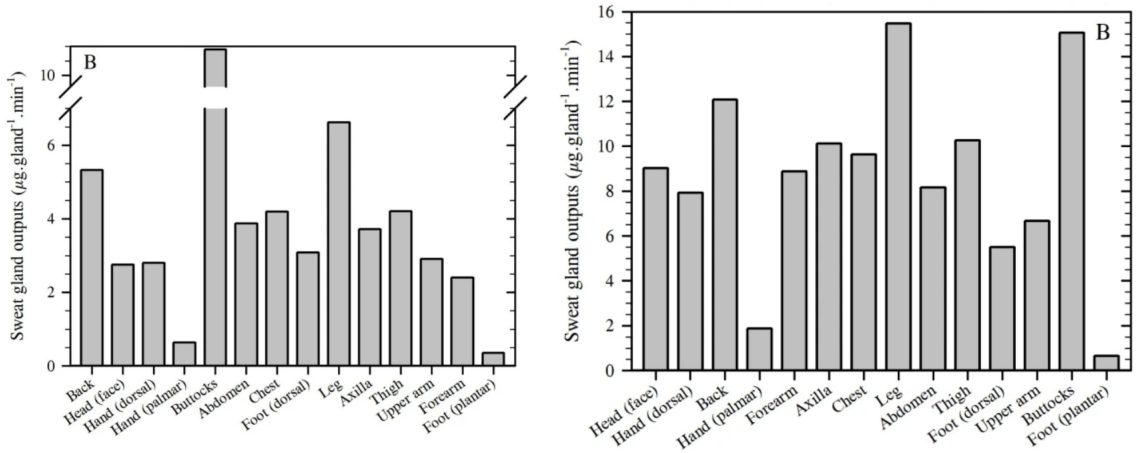

(a) Sweat output in rest

(b) Sweat output in activity

Figure 1.3: Difference in sweat outputs under resting (a) and active conditions (b) per body region. Reprinted from [15].

The chest and head double in sweat gland output in the active state compared to the resting state. The feet and hands have a rather low output, but this is offset by the amount of active sweat glands in the region. Therefore, the sweat rates are described per surface

area, which was measured by ventilated capsules in 2013 [15]. The forehead, fingers, back and ventral forearm have a relatively high local sweat rate of $0.4\,\mathrm{mg/(cm^2 \cdot min)}$. In exercise, there are mixed results, some claiming that the chest has the highest sweating rate [19, 17], while others claim that the head and extremities provide the highest sweat rate [15]. Generally, passive heating elevate the sweating rates to a lesser extent than exercise [14, 15]. Unlike heating or exercise conditions, the secreted sweat volumes are extremely low at rest($< 10\mu$L) [3].

1.1.4 Sweat stimulation

Through artificial stimulation of the sweat glands, it is possible to collect sweat in a sedentary environment. As exercise might not be an option for everyone, this is critical in the medical context [2]. Iontophoresis is a promising technique where a current is generated between two electrodes on the skin by applying a voltage , but it can cause skin irritation with long term usage [2]. Beneath the electrodes is a iontophoretic agonist which is directed into the skin due to the electric field, see Figure 1.4. The sweat stimulant then promotes sweat production in the glands. The duration of increased sweating depends on the compound. Metacholine and pilocarpine promote sweating for around an hour, with the former reaching sweat rates up to 100 nL/min/cm^2 [3]. Recently, the use of carbachol as a iontophoretic compound was investigated. This facilitated a longer, more stable sweat response, suited for long-term continuous monitoring of sweat [2, 20]. At lower dosages, it was possible to achieve >24 hour localised stimulation due to the slow metabolisation of carbachol, although this was only achieved for male participants [20].

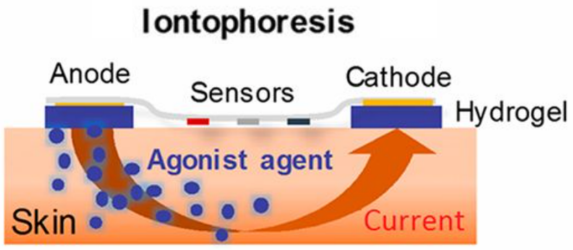

Figure 1.4: The working principle of iontophoresis. Adapted from [3]

Nevertheless, one should note that this method of stimulation only targets one pathway of sweat gland secretion, namely the cholinergic pathway. With exercise or heat strain, other pathways are involved [21]. This could explain why there is a discrepancy in forearm sweating rate when comparing exercise or thermal stress with pilocarpine iontophoresis [14].

1.2 Microfluidic sweat rate sensors

1.2.1 Relevance of sweat rate

Where blood analysis can provide consistency in results for many biomarkers across a wide population, sweat is more dynamic, because the contents of sweat (99% water) and the

sweat secretion rate are influenced by age, fitness, diet, sex, ethnicity and body site [14]. This renders it rather difficult to identify proper healthy ranges of analytes. Moreover, sweat rate partially determines the composition of sweat. This is on one hand because the resorption rate of Na^+ and Cl^- cannot compete with the sweat production rate, and on the other hand because other analytes in sweat are diluted at higher sweat rates [16]. It is therefore particularly important to include sweat rate measurements to perform meaningful sweat analysis.

At rest, sweat production per gland is limited to nanolitres per minute, which is hard to analyse. Thus, sweat production can be stimulated naturally through exercise or heat, or artificially by iontophoresis. The differences in sweat rate persist ranging from 0.12 μL/cm^2/min up to around 1 μL/cm^2/min [15]. Critically, there seems to be a significant difference between sweat rates of male and female subjects, which can be attributed to differences in body mass and metabolic heat production [16, 20]. Yet, this underlines that only considering sweat composition could affect the interpretation of results for a major part of the population. Healthcare would thus greatly benefit from wearable sweat sensors and continuous sweat analysis without a potential bias towards sex.

This means also incorporating sweat rate sensors in the biochemical analysis [22], as it can account for the variability to a great extent [23]. Harshman *et al.* (2021)[23] investigated the sweat composition and rates of 11 men who were subjected to 2 exercise routines for sweat collection on the forearms. Interestingly, they noted a variance between the left and right forearm sweat rate, but most importantly: after a sweat ion conductivity analysis and global metabolomic analysis they found that, respectively, 77.8% and 72.7% of the variation in their measurements could be corrected with sweat rate normalisation, reiterating the importance of accurate localised sweat rate determination for generating reliable results [23].

For cystic fibrosis, sweat analysis is clinically adopted as a diagnostic tool [14, 6], but therapeutic drug monitoring in sweat can also be promising. For brevity, a few novel applications are mentioned below, all requiring a sweat rate sensor for reliable results.

People that could benefit from sweat analysis, are patients with obesity who are receiving antibiotic treatment. Due to a higher fat mass, antibiotic absorption is impaired. This requires frequent monitoring of the drug levels in blood [24, 25]. Doing this in sweat would provide a convenient, non-invasive and laboratory-independent way of monitoring the drug level. Not only is sweat monitoring an easier alternative than measuring antibiotics in blood, but it might also convey more information for better decision-making processes. Antibiotic tissue penetration can vary within patients and sweat antibiotic levels are downstream from the site of infection. This means that the antibiotics have passed the tissue before entering the sweat. Thus, the concentration of the antibiotics in sweat may resemble the antibiotic levels at the site of infection more closely than in blood, which can be deemed upstream [26]. Still, standardisation of sweat measurements must be considered for the potential use in drug monitoring [27, 23].

In combination with measuring ionic concentration, sweat rate can also be used to estimate a person's hydration status [6, 28]. This is not only convenient in sports for the determination of the dehydration threshold and the optimal hydration point for max-

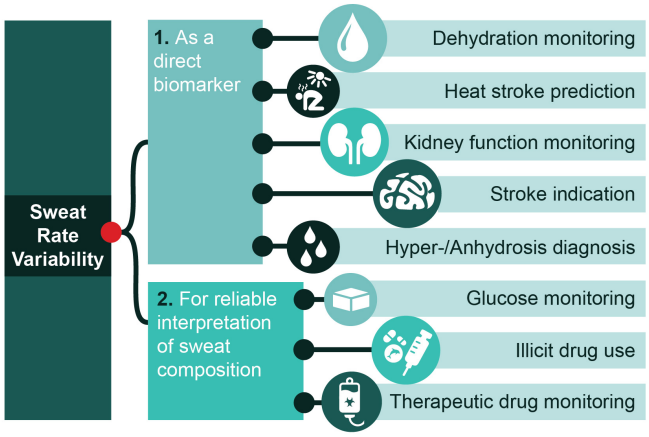

Figure 1.5: Examples and opportunities for sweat rate sensor applications.

imising physical output (Figure 1.5). There are also many benefits in healthcare. For example, knowing one's fluid balance can be critical in heart- and kidney failure [6]. In dialysis patients, knowing the hydration is critical but hard to monitor. Some patients become anuric or have very low urine production due to impaired kidney function, which results in a low frequency of analysis [29]. Other methods, such as imaging the inferior vena cava or using bio-impedance spectroscopy can also be adopted [30, 31]. As sweating is continuous, though significantly reduced in some groups of dialysis patients [32], sweat sensors could provide a new, simple method of determining fluid status in dialysis patients in the future. In addition, in the case of certain pathologies, sweat rate may also be altered and thus be used as an indicator, such as hyperhidrosis, anhidrosis, kidney failure or impaired kidney function and strokes [33, 6]. For other opportunities where a sweat rate sensor is necessary for sweat composition analysis, the reader is referred to these reviews [2, 10].

Research in both the physiological and technological measurement of sweat is necessary to provide reliable diagnostics by using wearable sweat sensors. To this end, a wearable microfluidic sweat sensor should include both a chemical sensor and a flow rate sensor, as composition and flow are intertwined. While microfluidic flow sensors are commonly used in other fields of study, sweat has added complexity due to the low excretion volumes and low and irregular flow rates. Resting thermoregulatory sweat is produced at 0.5 nL/min/gland at its minimum [15]. In activity, this can increase significantly to rates up to 15 nL/min/gland depending on site [15, 33]. While a higher production of sweat reduces the time of analysis, physical exercise cannot serve as a viable means for the medical monitoring of bed bound patients or those with limited mobility. To induce more sweat production and thus flow, artificial sweat stimulants such as pilocarpine, acetylcholine or carbachol via a iontophoresis patch can be used [3, 20, 34].

Moreover, sweat is subject to dynamic changes, which is quite different to the relative stability of blood levels. This means that it is difficult to determine a person's metabolic state from merely the composition of sweat. Not only are there practical complications e.g. evaporation and contamination on the skin surface, many physiological factors also

contribute to the dynamics of sweat composition. As mentioned earlier, different flow rates cause different concentrations of sodium and chloride due to limited resorption. Moreover, sweat rate is dependent on ethnicity, gender, age [35], diet, environmental factors and physical activity [6, 22, 16], with men having higher sweating rates [20], although this is related to higher body mass [16]. This renders it quite the challenge to find reliable data for diagnostics and underlines the importance of the ability to measure more than solely the sweat composition. For this reason, sweat rate sensors have been developed.

1.2.2 Filling Principles

Sweat samples can be collected by utilising absorbent patches, bags and gloves [2, 5, 36]. Another way to collect sweat is through microfluidic patches on the skin. Microfluidics enhances sample collection by minimising sample leakage, evaporation and contamination, whilst also improving the accuracy of the measurements. Microfluidic channels limit evaporation and allow for an accurate, fixed volume of sweat to be processed, which improves the reliability of the analysis [9]. Using a flow also limits contamination through constant renewal of the fluid. While microfluidic channels are typically etched in glass or silica, this is not practical for a wearable microfluidic sweat sensor. In patch form, a wearable sweat sensor needs to conform to the flexibility of the body for user comfort and a robust attachment to the skin. The material of the patch contacting the skin should therefore match the properties of the skin [9]. In addition, it should be able to harness microfluidic channels for fluid transport and storage. Traditionally, microfluidic flow can be controlled with the use of valves and complex external control modules and pumps. For our application, these would not be compatible. This means that for portable sweat detection, novel driving forces must be investigated [37]. An overview of these driving forces can be found in Figure 1.6.

Capillary action

The capillary effect is inherent to microfluidic channels. Due to cohesive and adhesive forces, sweat is spontaneously drawn in the channels. This effect can be further enhanced by using hydrophilic coatings [38]. Moreover, by using smart geometries, one can even direct sweat for sequential filling of reservoirs and leakage prevention [39, 40, 41]. The capillary effect and its uses are explained in detail in Chapter 3. Although capillary pressure facilitates filling, it does not facilitate fluid discharge after filling, which impairs long-term measurements.[17] This is because capillary action only occurs at a three-phase contact surface (solid-liquid-gas) [42, 17]. For this reason, the capillary effect can be combined with evaporation to empty the channels to enable continuous measurement, as will be discussed later.

Hydration interface

To improve sweat collection, a hydration interface is typically used. A hydration interface can be created by placing a hydrophilic porous medium, such as filter paper, or a hydrogel at the inlet or outlet [43, 42], as is depicted in Figure 1.6B. In doing so, a pressure difference between sweat and the hydration interface is created, either by capillary porosity

or osmotic pressure [37]. The hydrophilic porous material is typically positioned at the collection area of the patch to promote the continuous uptake of sweat. This consequently fills the microchannel with reduced sampling time and improves sampling efficiency (Figure 1.6Bii) [37, 44]. Instinctively, to maximise the number of accessible sweat glands and analyte volume, a large collection area is ideal for a microfluidic patch. As a downside, this also creates a large dead volume to be filled first before advancing into the channel. Nyein *et al.* tackled this problem by using a hydrophilic filler overlaying a hydrogel [44]. This resulted in a faster filling, as the filler and gel minimised dead space and enabled quicker sweat extraction. This was earlier demonstrated by Shay *et al.* [43]. A hydration interface could thus be an important addition to minimise filling time.

The downside of using hydrogels is that they become dry or contaminated after several hours of use. This requires regular replacement of the hydrogel and might limit its use to single-use sweat patch designs [37]. In addition, they can possibly dilute the sweat composition, which is why Nyein *et al.* opted for only a thin hydrogel layer in their design [44].
Fu *et al.* recently developed a microfluidic sweat patch based on capillary forces and evaporation, with a hydration interface as intermediate [42]. To increase the evaporation efficiency, a porous graphene slab was used at the end of the channel. Sweat was absorbed from the channel and driven to evaporate by the increased evaporation area of the porous graphene. A regular rinse of the porous graphene was suggested for reusability and long-term use [42]. The employment of such microstructures is an interesting approach as it enhances sweat discharge and might be a future direction in sweat patches.

Surface Tension Gradient

In order to facilitate quick filling of the microchannels, the hydrophilicity of the channel material is a key factor. Associated with hydrophilicity is surface tension. It is defined as the tension of a surface film of a liquid to minimise the surface area (Figure 1.6Bi) [48]. At the microfluidic scale, the surface tension of a fluid plays a leading role and depends on the surface material and the liquid [48]. Zhang *et al.* introduced a surface tension gradient in a smartphone-based wearable electrochemical sensor to monitor copper ions in sweat [4]. This gradient acts as a passive driving force for the sweat in synergy with the capillary action, accelerating loading time. Another demonstration of the potential of a surface gradient force is in an optical textile-based sweat sensor [49]. Like the two-faced Roman deity, Janus textile is a fabric that contains a hydrophobic side facing the skin and a hydrophilic region on the opposite side [49, 45]. Because of this feature, the sweat is forced to the hydrophilic surface in unidirectional fashion (Figure 1.6Ciii). Liu *et al.* also used Janus textiles to collect sweat. Here, sweat was guided towards microchannels in between textile layers (Figure 1.6Ciii) [45]. Similar to the hydrogels to promote channel filling and minimise empty space, this two-faced fabric could also serve the same goal, rapidly directing sweat towards the channels, by their steep surface gradient instead of osmosis or capillary action.

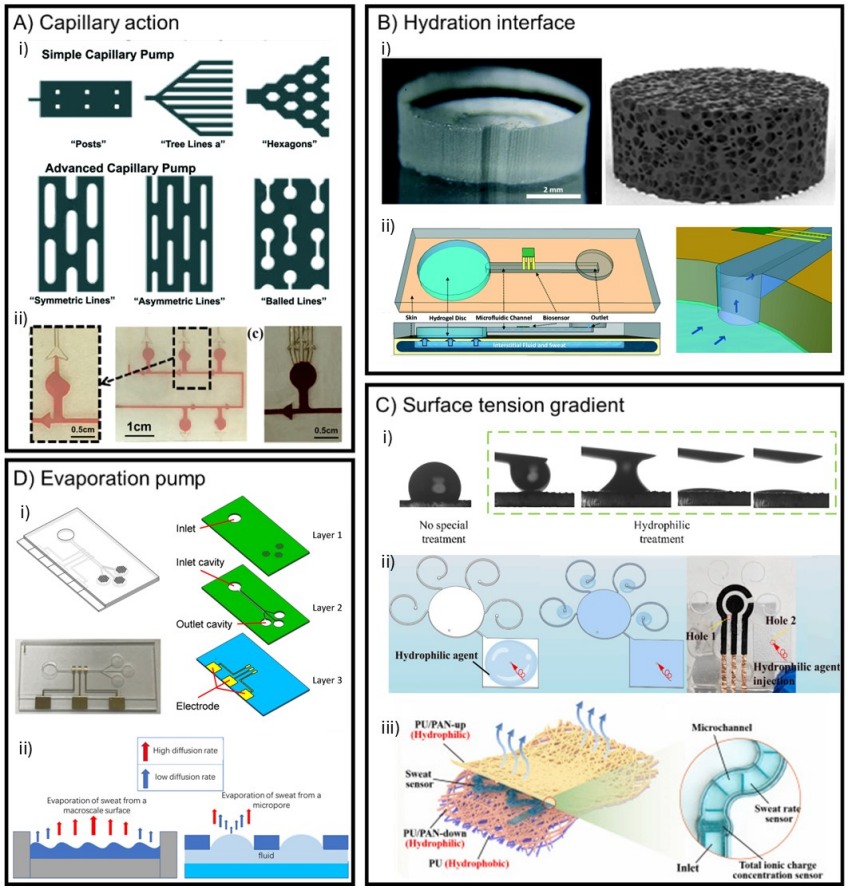

Figure 1.6: Filling principles in microfluidic sweat patches. A) Techniques to promote and direct flow, showcasing i) simple and advanced capillary pumps to facilitate quicker filling Reproduced from.[38] Copyright 2018, *Lab Chip*. ii) The implementation of burst valve to direct flow. Reproduced from.[40] Copyright 2023, *Biosensors*. B) Hydration interfaces to draw sweat and minimise dead volume. i) Respectively, a hydrogel and porous graphene to illustrate the common mechanisms, osmotic pressure and capillary porosity for hydration interfaces, reproduced from Shay *et al.*, 2017[43] and Fu *et al.*, 2024[42], respectively. Copyright 2017, *Lab Chip* and Copyright 2024, *Biomicrofluidics*. ii) Implementation of a hydrogel at the inlet of a microfluidic patch, Reproduced from.[43] Copyright 2017, *Lab Chip*. C) Illustrations of surface tension (gradients). i) Difference between a hydrophobic and a hydrophilically treated surface, resulting in a low surface tension, Reproduced from.[42] Copyright 2024, *Biomicrofluidics*. ii) Loading of a hydrophilic agent to create a gradient in surface tension. The agent is injected in the outlet, Reproduced from.[4] Copyright 2024, *Talanta*. iii) A Janus textile with a hydrophobic and hydrophilic side, containing a PDMS microfluidic channel for sweat (rate) analysis), Reproduced from.[45] Copyright 2023, *Biosensors and Bioelectronics*. D) Examples of an evaporation pump mechanism i) Implementation of micropore arrays at the end of a microfluidic patch for sweat analysis, Reproduced from.[46] Copyright 2019, *Micromachines*. ii) Illustration of mechanism behind evaporation pumps, where diffusion rates are elevated at the edge, opposite to the macroscale, adapted with permission.[47, 37] Copyright 2011, *Lab Chip* and Copyright 2020, *Nanotechnology and Precision Engineering*.

Evaporation Pump

Another method of promoting flow is incorporating an evaporation pump into the design of a microfluidic patch (Figure 1.6Di). By combining evaporation action with capillary action, a continuous sweat collection flow can be supported or sped up without the need for an external driving force. This is often achieved by placing micropores at the outlet of the microfluidic chip or patch. By designing an array of micropores instead of one large surface, the evaporation is enhanced massively (100x for the same area), pertaining to higher diffusion rates at the edge of the pore (Figure 1.6Dii) [37, 47]. However, an accumulation of electrolytes at the evaporation pump can limit the lifetime of the pump. Niu *et al.* recently developed a wearable electrochemical sweat sensor inspired by tree transpiration. They designed a leaf-like outlet adopting evaporation and secretion through 'air holes' to improve performance. The sweat production rate is increased by a microheater (45 to 47°C), whilst also subjecting volunteers to exercise. It is reported to achieve a 16 μL/min sweat collection efficiency [50]. However, no further elaboration on the outlet design and its effects on the flow rate in the patch is provided. Fu *et al.* designed an evaporation pump using a porous medium [42]. On one hand, the porous graphene creates a hydration interface with the channel, as discussed previously. On the other hand, the porous graphene creates a (micro)pore interface with the air when the channel is filled, significantly increasing the contact area of sweat with air due to its porosity. To test for reliability, 5 μL droplets were added to the evaporation series. The evaporation rate remained fairly constant at a rate of around 0,4 μL/min/mm^2. This was sufficient to measure physically active participants during 180 min. For long continuous use, a regular rinse of the evaporation pump with a small amount of water is suggested [42].

1.2.3 State-of-the art flow rate sensors for sweat

In physiological research, gravimetric methods such as absorbent patches and ventilated capsules are adopted frequently. The former method uses the collection of a certain sweat mass over time to determine flow rate, while the latter is able to continuously measure sweat rate based on humidity after actively evaporating the sweat by nitrogen gas or dry air [51, 36].
To measure flow rate in a wearable sweat sensor, the means are limited, as there is no room for large equipment and the use of probes can interfere with the measurement. Therefore, methods for determining real-time flow rate with the ability to be miniaturised have been developed for the integration in wearable devices. These methods include: I) Impedimetric methods, II) Image analysis, III) Volume dispensing systems and IV) Calorimetric methods.

Impedimetric and capacitive measurements: Discrete and Continuous methods

Typically, impedance measurements are adopted to measure flow rate based on channel filling. Electrodes can be integrated into the channels of a microfluidic sweat patch. When the channels are filled with sweat, the electrodes are covered and the conductance

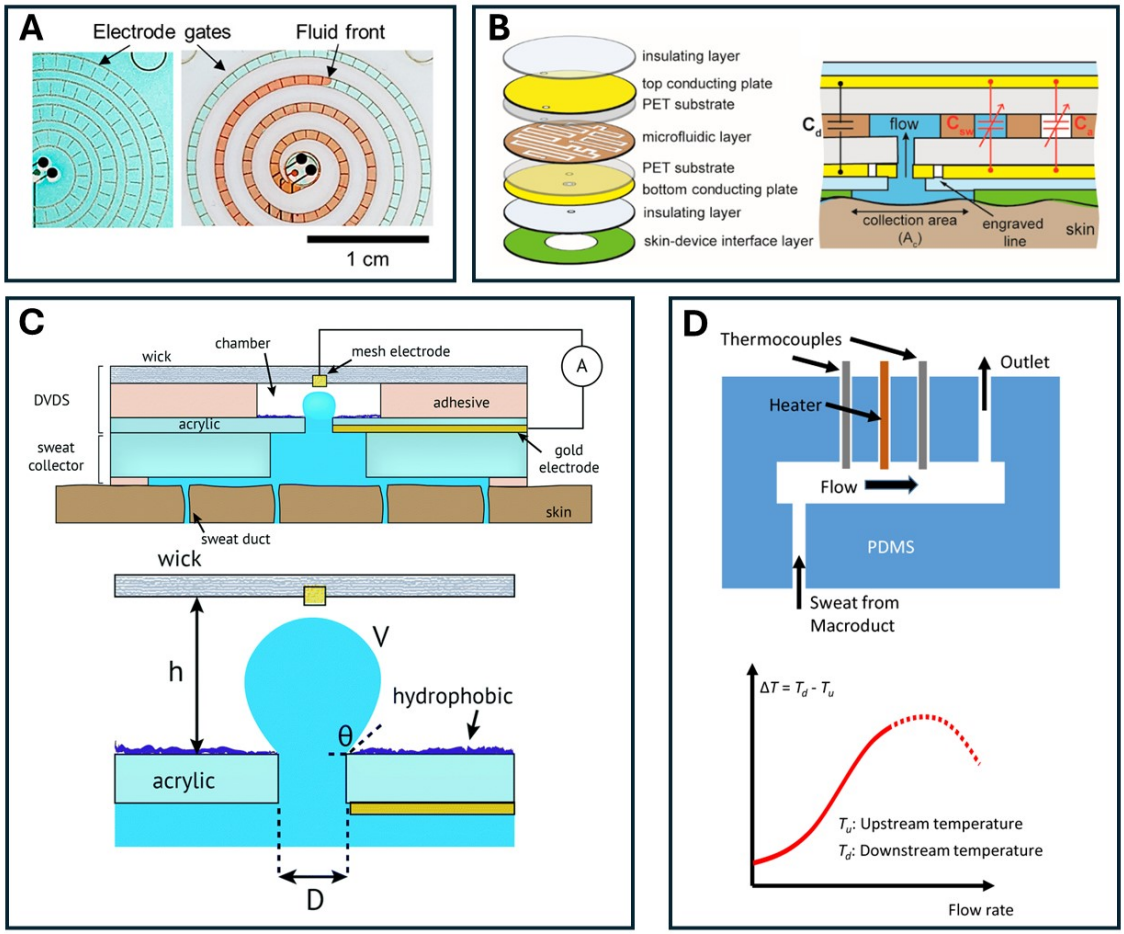

Figure 1.7: Schematic overview of the presented flow rate measurement techniques (excluding the indirect derivation from the sweat composition). A) Illustration of impedimetric measurement showing interdigitated electrodes in a spiral channel with a propagating fluid, Reproduced from [52] Copyright 2022, *ACS Sens.* B) Illustration of a continuous capacitive flow rate sensor, where the microfluidic channel resides in between the conducting plates, changing the capacitance as result of different ratios of sweat (Csw) and air (Ca). Reproduced from.[53] Copyright 2020, *ACS Sens.* C) A schematic overview of a volume dispensing system, illustrating the droplet before an absorption event with the wick takes place. The height (h), contact angle (θ) and diameter (D) of the opening influence the absorption frequency with a given flow rate. Reproduced from.[54] Copyright 2018, *Lab Chip.* D) Illustration of the calorimetric method, consisting of a heater equally spaced between two thermocouples. Reproduced from.[55] Copyright 2018, *Sensors.*

will increase, which can be easily registered with an impedance measurement. In early designs, the electrodes were placed parallel to the microfluidic channel. Upon further filling, the reduced impedance could be calibrated for real-time sweat rate measurements [56]. However, the sweat rate measurement is less accurate due to its susceptibility to changes in sweat composition [52, 51], as it does not only measure fluid volume but also the resistivity of the fluid itself, which might be subject to change.
A way to circumvent this is by opting for an interdigitated set-up [52], which is also how Bariya *et al.* improved on a previous continuous design [56]. The electrodes are now screen-printed perpendicular to the microchannel and the changes between the electrode pairs are monitored (Figure 1.7A). This results in a discrete measurement: the fluid front passes electrode spokes, which results in a qualitative conductance peak, instead of a continuous signal. A higher flow rate can be identified in the form of a higher number of checkpoint crossings within a certain time period. The flow rate is retrieved based on calibrating the crossing frequency with known flow rates [52]. This method is the most commonly used in sweat rate sensor patches [52, 57, 44, 58, 41].
Despite being relatively simple and easy to incorporate in a sweat sensor, the time of measurement is ultimately dependent on the channel length and the sweat rate. Because of inter-individual differences in sweat secretion rates, the monitoring time would differ per patient. Another concern is that of contamination of the channels over various measuring cycles. This results in measurement failure due to irregular filling of the channels [52]. For the development of a reusable device, this problem should be tackled, for instance via periodic flushing of the channels with water.
A creative solution was found by Lin *et al.*, where they measured the propagation of a microbubble as it passed sensing electrodes for iontophoretically- and exercise-induced sweat profiles [59]. The bubble is generated through electrolysis and then transported along the channel guided by the sweat flow. It provides a means of measuring flow, even when the microfluidic channel is completely filled. This method of discrete impedimetric sensing showed good agreement with the expected physiological response of the tested subjects in both conditions, measuring sweat rates from 8 μL/min down to approximately 0.7 μL/min [59].
Liu *et al.* designed a patch that relies on interdigitated electrodes, but without the limit of channel size by providing an adaptively resettable microfluidic patch [41]. As the channel fills, the sweat sequentially passes the electrodes. When the sweat reaches the outlet, it interacts with the absorbent to separate the fluid volume. In addition, the authors use a vent structure to maintain the air-liquid pressure equilibrium for better separation in the microchannel. To prevent leakage, stop valves are employed. These are hydrophobically treated and have a geometry with a bursting pressure that surpasses that of the microchannel. Therefore, the sweat will proceed along the main microchannel without leakage. Moreover, the design is reusable. The absorbent wick can easily be replaced. This design could process over 300 μL of sweat in a single measurement, outperforming other sensors [41]. Interestingly, it is compatible with different absorbents, and it is claimed to remain stable under various body movements and interference [41].
A continuous capacitive method for flow rate measurement can also be used (Figure 1.7B) [53]. This technique uses parallel capacitor plates above and below the layer containing the microfluidic channels, offering simple fabrication. The capacitor presents a linear re-

lationship between the capacitance change and flow rate as more sweat fills the channels between the plates. The results show similarity to the commonly used Macroduct collection device [53]. However, similar to continuous impedimetric measurements, it is expected that a change in ionic contents during measurement also contributes to the measured capacitance [60]. With more complex manufacturing and geometries, real time capacitive flow measurements can be very precise with the ability to measure sub-nanoliter changes for microfluidic applications [61]. However, for multiple measurements, this method is susceptible to interference from sweat residue in the microchannels, compromising the technique [52]. The sensitivity to variable sweat composition remains to be examined.

Volume dispensing systems

Another recently developed method for establishing flow rate measurements is digital volume dispensing systems (DVDS), as introduced by Francis *et al* [54, 62, 28]. It is a discrete method that relies on the temporary shorting of periodic droplets generated between two electrodes with a small, constant voltage applied (0.5 V). Sweat passes the first electrode as it enters the droplet chamber. The bottom of this chamber contains the inlet hole and a superhydrophobic surface to promote a consistent spherical shape of the droplet (Figure 1.7C). A second electrode is placed on the top part of the chamber. The top part consists of an absorbent material which wicks the droplet as soon as it comes in contact with the absorbent. The height of the chamber mainly controls the volume of the droplet. This system shows great durability and reliability: it can continuously operate for up to around 200 hours at 0.1 nL/min (syringe pump) without missing an event. A similar, yet different approach was taken by Wang *et al*[28]. They incorporated a vertical fluid rate sensor in a wearable platform which also detected electrolyte concentration. While this method also relies on a wicking material to break surface tension and absorb droplets, the droplet is allowed to fill the chamber completely until it touches the absorption layer. This creates a relatively constant volume to be absorbed. An electrode is placed at either side of the chamber, measuring conductivity. The diameter of the chamber and the distance of the electrodes to the absorption layer were optimised to provide a maximum conductance signal [28].

Image analysis

Another distinct approach is using visual inspection to give an indication of the flow rate [17, 63]. For example, Nie *et al.* developed an evaporation based digital microflow meter that operates in the range of 30-250 nL/min [17]. The outlet consists of an array of micropores. For certain flow rates, not all pores will be reached as the flow rate equals the evaporation rate before that time. The flow rate can thus be determined from the amount of visibly wetted micropores. atzeu *et al.* made use of the existing infrastructure of the Macroduct Sweat Collector to create another visual method for determining flow rate [63]. By placing black food colouring at the entrance of the collector, they coloured the sweat. This created a contrast which could be filmed as it propagated.[63] This colorimetric method does not rely on the electric properties of sweat, as opposed to electrochemical methods, which makes this technique attractive [62]. In addition, it does not require the integration of a power unit, because all analysis can be done off-site by camera or

mobile phone [62, 64]. Due to the simplicity of the colorimetric method, its use has been widespread. The Rogers Research Group has over 5 years experience with the use colorimetric sweat sensors and have recently contributed bringing a colorimetric sweat rate sensor to market [8, 65, 66]. The single-use patch is intended for athletes to visualise and measure fluid loss and make personalised hydration recommendations for better recovery [66]. Colorimetric method has also been employed to analyse sweat composition by binding biomarkers, altering the colour in a chemical process [2]. It does, however, face some challenges. Like the interdigitated electrodes, this method is ultimately dependent on channel volume, and the dye must not interfere with other measurements. However, by adding a texture on a PDMS surface for instance, the use of dyes can even be omitted [67]. Reeder *et al.* designed a manually resettable patch for the hydration of athletes. The patch adopts the optical properties of the PDMS microstructures in such fashion that an empty and filled segment of the channel can be discerned [67]. Manual inspection of the patch remains necessary, posing a potential drawback of this method.

Calorimetric methods.

The final method to introduce is the calorimetric method where energy is added to the system (Figure 1.7D) [68, 69, 55]. Kwon *et al.* achieved this in the form of a small thermal actuator, accompanied by a thermoresistors up- and downstream to the heater [68]. It is able to continuously measure the flow rate through the temperature difference between the thermoresistors in a short linear channel [68]. If no flow is present, the heat would be dissipated in a symmetrical manner. If the flow is present, a temperature difference will be measured between the up- and downstream thermistor. This method was extensively tested for reliability under various conditions such as temperature changes, airflow, mechanical oscillations (5Hz, 2mm amplitude), and 1 hour of testing. By using a separate reference thermistor, any environmental effects on the thermistors could be corrected in this way. This method enabled flow rates from 0-5 μL/min to be measured [68]. As the flow rate reaches a critical maximum, the cooling effect of fluid flow exceeds the heating effect [33, 55].
Similar to the DVDS, the calorimetric method does not rely on channel length or the electric properties of sweat to provide a signal. Besides, it needs integration of a power supply. Measuring flow rate by temperature difference and sweat composition via colorimetry can be done simultaneously. When combined with other biochemical sensors, the influence of temperature variation at the site of the biochemical sensor must be considered for accurate analysis.

Conclusion

Four distinct modalities have been introduced to assess sweat rate, covering the electrochemical, thermal, mechanical and optical domains. Continuous and discrete capacitive and impedimetric methods measure fluid propagation and are the simplest to apply, but are limited by volume capacity. Continuous capacitive and impedimetric measurements could be sensitive to the fluctuations of ionic content as well [52]. Discrete impedimetric methods are more selective to the flow rate and the most widely used in patch designs. To deal with the dependency on channel volume, one can tailor the channel shape to

the expected sweating rate [44] or create a resettable design as recently demonstrated for both the colorimetric/visual analysis method [67] and interdigitated electrodes [41]. The latter was truly continuous, because it was self-adaptable due to the wick at the end of the channel, creating a new attractive design of a widely adopted technique for continuous monitoring.
Self-resettability is also implemented in the DVDS that use a wick and a pair of electrodes to detect the periodic absorption of a droplet and subsequently deduct the flow rate [41]. Digital volume dispensing systems are capable of long-term, real-time measurements, but have more complex fabrication requirements. DVDS are compact and generate droplet wicking events from which the flow rate is deducted. The calorimetric method provides the same benefits as DVDS. It only needs a linear channel to continuously measure flow, but efficient power integration is required [33]. It measures flow rate based on the temperature difference between two thermopiles, equally spaced from a heater. In doing so, the calorimetric method has shown robustness under various conditions such as mechanical vibrations and temperature changes [68].

When moving towards a wearable solution for measuring sweat rate, new user-centred requirements or constraints may be considered, such as resistance to motion, or ease-of-use. This will be discussed in the next chapter.

Chapter 2

Requirements & criteria

2.1 Scope

Wearable sweat sensors can be widely implemented in sports medicine, geriatric care and healthcare. The environment for which the sensor will be developed is critical, as they pose different requirements. A sports sensor will be exposed to frequent, larger movements on a small timescale, also experiencing larger mechanical stresses than a bedside sweat monitoring device. Manual inspection of the filling is possible, but not desirable during a performance run, for instance. In our case, the focus will lie on the context of therapeutic drug monitoring (TDM) in a clinical setting. In doing so, the medical use of the sweat sensor could be expanded to more than solely the diagnosis of cystic fibrosis (CF). However, because clinical patients should not be subjected to exercise or high thermal stresses due to their condition, the amount of sweat for analysis is limited to resting sweat (0.2 nL/min/gland). To boost sweat production, artificial sweat stimulants are used. These increase sweat rates, but, as mentioned in the previous section, these agents can also alter sweat composition by increasing the sweat rate, which must be accounted for in the interpretation of the measurement [70, 33, 13].

This is just one example of the trade-offs that have to be considered in the design of a wearable sweat sensor. Another trade-off lies within the geometry of the device. To direct sweat into microfluidic channels where sensors are located, dead volume in the collection area must first be filled. Accompanied by the low sweat rates, this can take multiple hours until reaching the channels. On the other hand, a large collection area covers more sweat glands, boosting flow and throughput. The low sweat rates can be increased by artificially stimulating the gland, but the measurements become less representative of an individual's own resting sweat rate [44].

Sweat sensors and sweat collectors are already being studied excessively and flow rate sensors for sweat to a lesser extent. This is despite the fact that they provide crucial information for the interpretation of the results, as analyte concentrations can depend on the sweat rate. To this end, the aim of this project is to design and build a reliable sweat rate sensor for therapeutic drug monitoring, illustrated in Figure 2.1. A sweat patch will be made in order to accommodate the flow sensor and to fit into the design of said flow sensor.

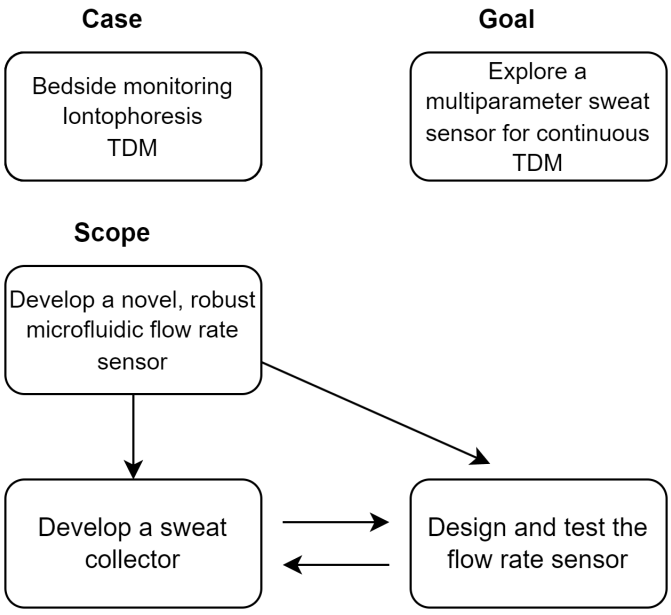

Figure 2.1: Diagram of project goals.

2.2 Requirements

In order to achieve this, the following requirements have been formulated:

1. **Measure flow rate real-time independently**
   The sweat sensor should provide independent real-time flow measurements in the form of on-site analysis. One of the strengths of wearable sweat sensors is that they may provide non-invasive real-time continuous monitoring [2]. Moreover, measurements can be performed without the assistance of healthcare professionals. This must, therefore, also be expected for a wearable flow rate sensor. The gravimetric method would fail this requirement, because it requires handling of the sample and weighing before and after collection [36].

   Furthermore, the flow rate sensor should be able to work with low volumes, with channel diameters often in the order of tenths of micrometers. Additionally, the flow rate within the channel can be estimated to be around 0.7 μL/min, although the actual flow rate could be as low as 0.2 μL/min , and as high as 1.5 μL/min. This is based on an average sweat output of approximately 6.5 nL/min/gland between male and female subjects and the lower and upper bounds of sweat output after iontophoretic stimulation with pilocarpine [20]. For an indication, the volar underarm with a density of 104 active glands/cm^2 [15] and a collection area of 1 cm^2 was used in the calculations. In reality, the flow rate may be higher, which is typically the case for men and lower for women due to differences in mass-specific body surface area [20]. These extreme cases provide the upper and lower bounds. The design must take compatibility with both flow rates into account, where the lower bound poses the biggest challenge on the sensitivity of the sensor.

Our goal is to provide a flow rate sensor which can measure flows in the abovementioned ranges and which can be incorporated with electrochemical sensors. In that fashion, the measurement of composition and sweat rate can be related to one another. The electrochemical sensors will measure the composition of natural and/or artificial sweat constituents minimally 3 times in a day. A measurement typically lasts 30 seconds for voltammetry with a minimal resting period. The flow rate sensor should give results on the scale of minutes, yet be durable over the course of a day. Now that this timescale is known, it is also relevant to identify the measurement time for measuring significant changes in sweat rate in iontophoresis. The profile of iontophoresis is that of a peak followed by exponential decay. However, the flow rate profile is not extensively researched as the gravimetric method only gives an indication of the total volume over a selected time period. Comparing to an experimental patch which uses capacitance to measure sweat rate, a result every 2 minutes would be relevant to, at the least, reliably determine the average sweat rate, since sweat rate can change on the order minutes [53, 71].

2. **Facilitate sample renewal**
   With the premise of non-invasive real-time continuous monitoring, the device should be able to measure flow rate samples in succession too. This means that the flow rate sensor should be capable of sweat renewal for multiple measurements and analyses. According to the Macroduct manual, the minimal sweat volume for clinical validity for Cystic Fibrosis diagnosis is 15 μL within 30 minutes, or a sweat rate of 0.5 μL/min [72]. A device with a volume of 5 μL must be emptied 3 times or have a continuous method of expelling sweat over the course of 30 minutes. It is hence important that the sample can be renewed, when the device is completely full, especially in the case of higher sweat rates ($\geq$1 μL/min) or longer measurement times. For several analyses a day – for instance, one in the morning, afternoon and evening – the device should also facilitate measurements after periods when the device is not in use. This requirement is necessary as some flow rate measuring techniques can work independently but do not allow for replenishment of the sweat after one analysis. For instance, a channel in which a fluid front measurement is performed, should be reusable. when the volume capacity is reached, the channel can be drained by a manual pressure pump as adopted by Bariya *et al.* or an absorbent as adopted by Liu *et al.*

3. **Reliable in bedside monitoring environment**
   For daily bedside monitoring in a clinical setting, reliable measurements must be ensured. While the forces and movements on the device may be considerably less rigorous than in a sports setting, bedside monitoring already poses challenges in the design of a flow rate sensor. A common placement of a sweat sensor is the volar underarm [15]. The flow rate sensor should be resistant to motion or deformation of the underarm. A typical approach is to make the devices from a flexible substrate. Conversely, the fluid rate measurement may be altered by stretching, bending and twisting of the device. For this reason, a rigid compartment can be considered. Secondly, the device must provide consistent measurements irrespective of orientation, accounting for potential variations as the wearer stands, walks, sits or lies down. Furthermore, the impact of fluctuations in other variables such as temperature or humidity can be taken into account.

4. **Have an operation time within the window of iontophoretic stimulated sweat glands**

To promote more sweat flow, iontophoresis can be used to deliver a stimulant to the sweat glands. Subsequently, sweat secretion is boosted for a certain timespan. For pilocarpine, this activity may last for around 50 minutes [71, 20]. It is thus important to make sure that the device can operate within this window. In the future, the device operation may be expanded to daily monitoring with another iontophoretic agent such as carbachol, which has recently been shown to exhibit elevated sweat rate to over 24 hours [20]. During the scope of this project, however, pilocarpine iontophoresis will be taken as a point of departure for the development of a robust flow rate sensor. The stimulation through iontophoresis elevates the sweat rate, with sweat rates ranging from around 10 nL/min/gland for male patients to 3 nL/min/gland for female patients [20, 73]. It is essential that the device is operable in both scenarios, with the lower sweat rates posing a greater challenge due to the resulting filling times.

2.3 Criteria

With the definition of the requirements, the intended performance of the flow rate system has been established. However, several solutions can meet the requirements. The following step is thus to evaluate the potential solutions using a weighted criteria method. First, the selected criteria will be introduced and defined. Afterwards, the criteria will be ranked based on perceived importance for the end goal with a weighting score.

1. **Robustness**
   Robustness is described here as the ability to provide reliable measurements under various conditions. In the case of bedside monitoring, the wearer will occasionally walk, stand, sit, or lie down. Therefore, the susceptibility of the devices to different orientations, motion and environments must be assessed. This is particularly relevant for continuous sweat monitoring over the course of a day. With pilocarpine iontophoresis, the measurements will be performed within the hour, for which the conditions are relatively constant. Nevertheless, during the analysis the wearer may vary in resting position or accidentally exert a force on the device. A robust device will not be affected greatly by such disturbances and is therefore preferred, especially since the flow rates are little (μL/min).

2. **Durability**
   Durability is defined here as the ability to withstand regular use and to provide reliable measurements over an extended period of time without significant deterioration or failure. It is, therefore, different from the Robustness criterion. Robustness concerns reliability during analysis, and durability concerns the reliability of several analyses. This thus also depends on the structural integrity of the flow rate sensing system.

3. **Cost**
   In this criterion, the expenses for the development of the potential solution will be considered. If the device is intended for single analysis, or single days, this will be taken into account in estimating the costs of performing 3 analyses over the course of a week. The costs of the device must be attractive to use in the clinic as an alternative for blood analysis. Yet, in the development of a prototype, the costs will be significantly higher than a mass-produced end product. In addition, due to the non-invasive nature of sweat monitoring, it is nonetheless preferable over blood analysis.

4. **Feasibility**
   The feasibility of the device can be defined as the achievability of a given design within the timeframe of the project and at this particular stage of the concept development. Because not all details or obstacles are precisely known, it is necessary to estimate how feasible it is to develop a concept further to deliver the desired results.

5. **Sensitivity**
   The sensitivity is critical for the performance of the flow rate sensor. It is the aim to develop a flow rate sensor capable of measuring both flow rates of around 0.2 μL/min up to 1.5 μL/min after pilocarpine iontophoresis. The concept solutions are to be evaluated on their possible sensitivity. A high sensitivity is preferable for a future use where lower, natural flow rates might be examined.

6. **Comfort**
   Comfort for the wearer must also be ensured and taken into account when deciding on a concept solution. Whilst this is not critical for a short analysis, relevancy increases with increased time of wearing. Discomfort and other hazards can be considered, although non-invasive sweat monitoring has minimal risks of harm to the wearer. If the solution must be worn tightly on the skin, or if it is a hindrance due to e.g. large size, then that can be reflected in this criterion.

7. **Sustainability**
   The purpose of this criterion is to minimise the environmental impact and resource usage of the device. The development of a non-invasive sweat sensor is promising not only for sophisticated hospitals, but also for point-of-care applications. In both cases, it is important to consider the environmental impact of the chosen design. For instance, a reusable device or modular device generates less waste than a single-use solution. On the other hand, a recyclable single-use device may be preferred over a reusable device with higher ecotoxicity upon disposal.

8. **Novelty**
   This criterion weighs in the scientific value and innovation factor in the concept selection. The novelty of an approach can be of great scientific value, since it can promote new solutions and perspectives on the problem. Therefore, for research purposes it is more desirable to have a completely novel approach than to adapt an existing solution with less innovation. However, exploring an unknown solution also increases the risks of failure. Yet, if successful, it can give way to a whole new range of solutions by changing tack.

2.3.1 Criteria weighting

Since not all criteria have equal importance, a weighted criteria method is adopted. Each criterion is compared against the other to generate a ranking using a prioritisation matrix, seen in Table 2.1. For each instance where a criterion from the leftmost column of the table was considered to take priority over one from the top row, the cell was filled with a plus (+) sign and coloured green and the opposite cell with a minus sign (-) and red. Each + in a row is counted at this determines the weight seen in the rightmost column. The higher the weight, the more important the criterion. The prioritisation is briefly motivated in order to enhance transparency and reproducibility of the used method.

	Cost	Robustness	Durability	Feasibility	Sensitivity	Comfort	Sustainability	Novelty	**Weight**
Cost		-	-	-	-	+	-	-	1
Robustness	+		+	-	+	+	+	-	5
Durability	+	-		-	+	+	+	-	4
Feasibility	+	+	+		+	+	+	+	7
Sensitivity	+	-	-	-		+	+	-	3
Comfort	-	-	-	-	-		+	-	1
Sustainability	+	-	-	-	-	-		-	1
Novelty	+	+	+	-	+	+	+		6

Table 2.1: Prioritisation matrix for weighting criteria

Feasibility and novelty are respectively the most important criteria. The project should be achievable and innovative. Aside from that, robustness and durability are then prioritised. This means that they also trump sensitivity, provided that the requirements are met. This is due to the wearable application where robustness and durability are a larger issue to solve. Sensing performance is considered more important than cost, comfort and sustainability at this early stage in conceptualisation and prototyping. In addition, with blood analysis as reference, comfort and sustainability are already expected to be superior to blood analysis. The weights help us evaluate the concepts more thoroughly. The concepts will be introduced and scored in the next section.

Chapter 3

Concept selection

3.1 Concepts and criteria scoring

In this chapter, several concept solutions will be introduced and assessed on the aforementioned criteria. The concept with the best scoring will be further developed and tested. The author will judge a concept based on either one or several closely related techniques, or attempt to ascertain its performance based on the main working principle.

3.1.1 Capacitive moisture gradient with evaporation interface

The goal of this concept was to adopt the measurement of a humidity gradient in a moisture wicking medium through capacitive measurements, as seen in Figure 3.1. The use of an absorbent has shown good results in microfluidic designs, minimising dead volume and filling times [56, 37]. While the absorption takes place, it enables a capacitance measurement at several sites. Moreover, the absorbent medium, e.g. paper, which is also used in lateral flow assays [74], is partially exposed to air at the end of the channel. This creates an evaporation pressure, drawing fluid out of the channel. In doing so, a balance will be established based on the absorbent and evaporative pressures. The balance in moisture gradient can be coupled with the amount of sweat created within a time frame.

Figure 3.1: Concept containing two capacitors C_1 and C_2 that measure the moisture level in paper or another wicking medium, enclosed by the two capacitors. Flow is driven by evaporation.

The benefit in using multiple capacitors is that environmental variables can be eliminated through measuring the capacitance difference. The measurements are continuously performed and sample renewal is only needed after a new cycle. This could encompass replacing the patch or the paper, but fabrication would be simple. Whilst capacitance has been employed for sweat rate measurements [53], a set-up like this has not been attempted. Measuring the

flow rate through a wicking medium is also novel, its use often being limited as a 'passive' absorbent. Capacitive sensing has been used for estimating moisture contents in agriculture [75, 76], however. A downside of this concept is that the sweat contents will be chemically bound to the paper, changing its behaviour over the course of a measurement [74]. A changing saturation may also influence the flow, which is a problem identified by [54].

For our application, a great difficulty lies in the balance between absorption and evaporation. The absorption may change due to the salt deposition and moisture level, and the evaporation pressure depends on external factors, such as humidity and temperature. The performance of the absorbent must be evaluated in its double role as evaporator. If the absorbent wicks and dries rapidly, it may interfere with the measurements. If the absorbent is completely saturated, the measurement will also be compromised. This concept will therefore be difficult to realise, because it requires thorough optimisation.

3.1.2 Compartment filling

This concept is inspired by discrete droplet counting devices to measure sweat rate [54, 28, 62, 41]. In this design, a droplet forms gradually until it touches an absorbent ceiling, leading to complete absorption of the droplet. This event can be monitored by using electrodes to measure conductivity of a droplet. The amount of droplet counting events is logically coupled to the flow rate. However, it is not necessary that a droplet is formed. A compartment can also be filled and partially wicked [28, 41]. Yet, the variable moisture level of the wicking ceiling can cause irregular and inconsistent absorption events [54]. Over time, salt deposition occurs leading to sensor failure. To tackle this a bursting valve geometry can be adopted to periodically drain a reservoir, as illustrated in Figure 3.2, inspired by a Pythagorean siphon. Instead of letting the sweat evaporate at the outlet of the drain, it can be transported to a waste reservoir or wick where the evaporation takes place over a larger surface, similar to [41]. This is to improve the life span of the device.

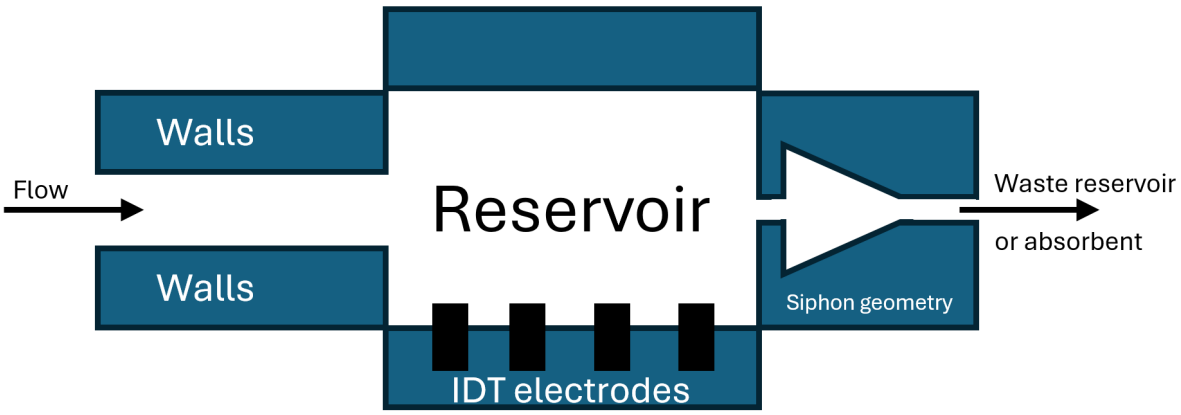

Figure 3.2: Compartment filling concept, where a reservoir is filled and monitored through IDT electrodes. Once it is full, it will passively empty through self-siphoning.

The benefit of this method is that it has already shown great potential in terms of durability [54]. It would, however, be interesting to also determine the sensitivity to motion of this method. Most wearables use flexible materials for user comfort, but deformation can cause irregular counting events. Using a rigid design could mitigate this issue. Additionally,

fabrication must consider geometry and surface properties, as they play a critical role. A microfluidic self-siphon also presents challenges. While a microfluidic swan beak has been used for pipetting cell cultures [77], scaling down for our application introduces significantly stronger surface effects, such as capillary action. These effects must be carefully considered to ensure efficient drainage [38].

3.1.3 Resonance weighing

The principle behind this concept is measuring mass, unlike the other concepts, which rely on analysing the electrical or electrochemical properties of the sweat sample. This concept adopts a resonator beneath the patch. As sweat fills the channel, more mass is added to the resonator, causing a shift in the resonance frequency. The flow rate can thus be determined by monitoring the amount of mass added to the resonance system over time. A benefit from utilising weight, is that it does not significantly depend on the chemical composition of the sweat, whilst providing a continuous means of measurement.

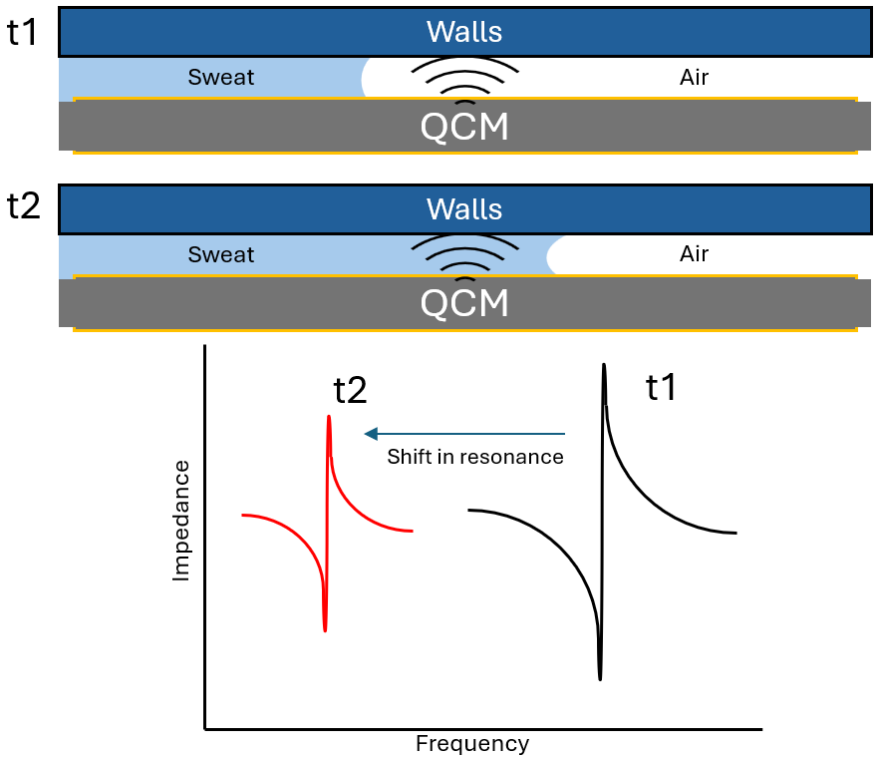

Figure 3.3: Illustration of a hypothetical resonance shift at different times t1 and t2 when using a QCM.

Resonators for mass weighing have been researched for Quartz Crystal Microbalances (QCMs) [78]. However, never have they been applied to measure microfluidic flow in a wearable setting. Additionally, the device could be developed to be modular, where the resonator module is incorporated in the read-out circuitry for other sensors. The device will be operable as long as the channels have not fully been filled. If the channels are full, the sweat can be atomised at the outlet. The benefit of atomisation is that this disperses little

sweat droplets, as opposed to evaporation of water, which leaves a salt deposition at the site of evaporation [54]. For creating the atomisation, a different resonator could be used based on the design of a piezo ink-jet printer head to help empty the channel [79]. Theoretically, one could even attempt to regulate the frequency of the piezo according to the perceived flow rate from the resonance microbalance [80]. Nevertheless, the concept mainly concerns the primary development of the resonance weighing principle, as seen in Figure 3.3.

One issue to be anticipated is that the vibrations interfere with voltammetric measurements, as these analyses are sensitive to convection [81, 82]. However, the device could be appointed a measurement frequency which alternates with the voltammetric measurements, as these operate on the order of a minute. Another hazard is cavitation from the vibrations, as air bubbles can occlude the channel. This problem could be solved by staying below the atomisation and cavitation threshold for water. This technique may be prone to external loading of the device, such as clothing on top of the sensor. Aside from this, it is interesting to examine the performance of such a resonance balance for evaluating microfluidic flow rates on the order of microlitre per minute.

3.1.4 Result of scoring

After evaluation of the criteria for each of the concepts, they have been scored to the best of our current understanding, which is shown in Appendix A.1. It followed that resonance weighing was pursued further, scoring 104 points as seen in Table 3.1. This measurement principle for flow rate has not been researched. The other techniques have been explored more exhaustively, although plenty of innovation and optimisation lie ahead of these principles. Compartment filling techniques are the most recent advancement in the field of wearable flow rate sensors, where capacitive and impedimetric measurements are already more common. Recently, Liu *et al* combined the two, creating an adaptively resettable interdigitated electrode flow rate sensor. Exploring this concept further could give rise to a new way of tackling flow rate measurements in wearables. The critical eye may notice that calorimetric methods were not considered in this assessment. This is a shortcoming because it is also considered a promising technique for sweat rate sensing, as already mentioned in section 1.2.3.

Scoring	Weight	**Capacitive Moisture Gradient**		**Compartment Filling**		**Resonance Weighing**	
Feasibility	7	2	14	3	21	4	28
Novelty	6	4	24	3	18	5	30
Robustness	5	3	15	3	15	3	15
Durability	4	2	8	5	20	4	16
Sensitivity	3	2	6	3	9	3	9
Comfort	1	3	3	3	3	3	3
Cost	1	3	3	3	3	3	3
Sustainability	1	2	2	5	5	5	5
Total score			**75**		**94**		**109**

Table 3.1: Results from concept scoring

3.1.5 Concept development

In this project, we will continue with the best, most innovative solution from the ranking: the exploration and feasibility study of a novel, ultrasonic flow rate sensing modality for microfluidic wearable sweat sensors.

The aim is to create a microfluidic structure around an existing piezoelectric element. This will facilitate ultrasonic measurements. Along the way, we must also explore the interaction between sweat and the sensor to develop a better understanding. This will be done by diving into the relevant theory in the next section and performing experiments in the subsequent section. Finally, a prototype will be presented demonstrating the feasibility of this method.

Chapter 4

Theoretical Framework

4.1 Introduction

The theoretical framework around microfluidics and piezoelectric sensors are discussed in this chapter. This helps to understand the governing laws of our concept solution and adopt them in our future design. Microfluidic channels will be used to transport sweat. It is important to cover microfluidics, because it describes the interaction of the sweat at the microscale. Piezoelectricity is the driving phenomenon behind the novel flow rate sensor. It must be understood how a piezoelectric sensor can interact with sweat and the microfluidic structure. Several types of piezoelectric sensors will also be discussed.

4.2 Microfluidics

In Chapter 1.2.2, recent developments were discussed in microfluidic sweat patches. At the base of these developments lies the field of microfluidics. Fundamental context is provided in this section.

4.2.1 Transport in a microfluidic channel

Microfluidics entails the transport phenomena and fluid-based devices at microscopic length scales [48]. These microfluidic devices consist of microchannels, -pumps and -valves [83]. In sweat sensing, they are beneficial for controlling sample volume and renewal, minimising leakage, contamination and evaporation [2]. Capillary forces are especially important for promoting sweat flow along microfluidic channels.

The surface tension, contact angle and wettability define fundamental fluid-solid interface behaviour. Surface tension can be seen as a cohesive force, where the molecules in the fluid are attracted towards the bulk of the fluid through van der Waals forces. The molecules on the boundary of a droplet, or at any liquid-gas interface, will not experience this attraction from gas. The unit is N/m [48, 84]. The contact angle defines the interaction of a droplet with a material. This shows the affinity of the liquid with the solid. If the contact angle is smaller than 90°, the liquid wets the surface and is said to be hydrophilic. A contact angle greater than 90° is non-wetting and said to be hydrophobic.

Because of surface tension, a pressure difference exists between the interior and exterior

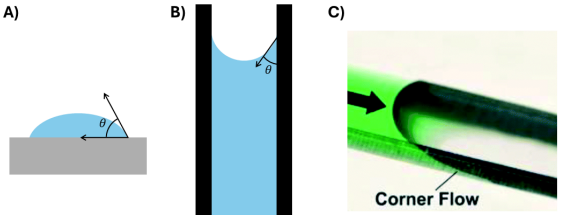

Figure 4.1: Schematic representations of microfluidic wetting phenomena and the contact angle θ. A) Contact angle of a droplet, B) contact angle of fluid in a channel, and C) Corner flow arising from two wettable surfaces intersecting. Image C is reprinted from [38].

of the fluid, see Figure 4.1. This is described in the Young-Laplace equation [85]

$$\Delta P = \gamma \left(\frac{1}{R_1} + \frac{1}{R_2} \right) \tag{4.1}$$

where ΔP denotes the Laplace pressure, γ the surface tension, R_1 and R_2 denote the radii of curvature of the interface surface [48]. In the case of a droplet on a solid, a balance exists between the cohesive forces of the bulk fluid and the affinity of the droplet with the solid's surface. This case can be expanded to a capillary channel. This capillary effect is dictated by the surface tension of the liquid and the geometry and surface chemistry of the channel [38]. Because of affinity to the sidewalls, This delivers a different profile, seen in Figure 4.1, where the fluid crescents inwards for a hydrophilic surface. In the 3D case, where two wettable walls intersect, corner flow, or edge-wetting, can occur [38].

The capillary effect is essential for driving passive filling in microfluidic sweat patches and delivering sweat to the sensing area in the shortest amount of time. Unaccompanied by auxiliary equipment, the sweat gland is the sole active driving force behind sweat flow. The filling is promoted by the negative pressure from the capillary action of the microchannels. For a rectangular microchannel, the Young-Laplace equation relates the contact angle, microchannel size and capillary pressure by the following expression: [38]

$$P = -\gamma \left(\frac{\cos\theta_t + \cos\theta_b}{h} + \frac{\cos\theta_l + \cos\theta_r}{w} \right) \tag{4.2}$$

where P is the Laplace or capillary pressure, γ the surface tension of the liquid in the channel, h and w are respectively the channel height and the width, and θ_t, θ_b, θ_l and θ_r are the top, bottom, left and right contact angles of the liquid with the channel walls. As the channel size decreases, the capillary pressure increases.

4.2.2 Promoting and directing flow in a channel

Microfluidic filling systems are called capillary pumps. The interaction where a liquid wets a surface can be exploited by using several strategies. For instance, one can employ various types of structures within a channel to enhance capillary filling, as seen in Figure 1.6 and discussed in Chapter 1.2.2. These structures maximise the contact area with the fluid, thus enhancing capillary capabilities [61], such as 'posts' as incorporated by Fu *et al.*[42] or an arboreal structure, incorporated by Niu *et al* [50]. Surface effects also play a significant role, which is why hydrophilic coatings, treatments or materials are often used to enhance capillary effects [38].

Laplace pressure can also be used to direct flow in a microfluidic structure. The fluid flows towards the lowest pressure. By an abrupt change in the channel, flow can be halted. One example of this is a capillary bursting valve. In an arrow-like fashion seen in Figure 1.6Aii, the walls make a sudden angle to dissuade wetting of the surface. This forms a meniscus and increases the Laplace pressure. The critical pressure at which the bursting valve conduces flow, can be expressed in a rectangular channel as

$$P_{burst} = -2\gamma \left(\frac{cos\theta_I}{w} + \frac{cos\theta_\alpha}{h} \right) \tag{4.3}$$

where γ is the liquid's surface tension, θ the contact angle in the vent channel, α the diverging angle of the stop valve, and w and h the width and height of the diverging section, respectively [41]. These valves are adopted to chronologically fill reservoirs [86] or to create air vents with minimal chances of leakage [41].

4.3 Piezoelectric sensors

Ultrasonic, piezoelectric sensors and transducers are used for many applications. They can be used for ultrasonic cleaning, sound, impact loading, distance, flow and microgravimetric measurements [78, 87]. It is this final application, we explore to measure channel filling and flow rate. First, we must get acquainted with the piezoelectric effect and understand the resonance behaviour of such a sensor. Specifically, the quartz crystal microbalance will be discussed, before existing relations for mass and fluid loading are elaborated upon, followed by other types of sensors.

4.3.1 The piezoelectric effect

When two quartz crystals are rubbed together, this creates a luminescent effect [88]. Quartz is a naturally occurring piezoelectric material and because of its asymmetric crystal structure, it can generate electrical charges under strain [89]. At rest, the net charge is neutral. When a force is exerted however, its internal structure is deformed, causing a potential difference. This transforms energy from the mechanical to the electrical domain. This is called the direct piezoelectric effect, as visible in Figure 4.2. The reverse piezoelectric effect occurs when a strain is induced as a result of an electric field. The reverse piezoelectric effect can be employed for precise actuation, also in the form of oscillations in the case of microgravimetric sensing.

4.3.2 Resonance behaviour

The interesting case with piezoelectricity, is that it not only intertwines physical properties with an electrical response, but it can also settle a clear analogy between physical and electric parameters [78]. This is illustrated by the following equations

$$V = \frac{\eta l}{A_s e^2} i_p + \frac{\rho_s l^2}{2A_s e^2} \frac{di_p}{dt} + \frac{cl}{Ase^2} \int i_p \, dt \tag{4.4}$$

where V stands for voltage, l the length or thickness of the piezo element and e the piezoelectric stress constant. The physical parameters are viscosity η, surface mass density ρ_s electrode surface A_S, the elastic constant c. i_p denotes the current induced by the piezoelectric effect.

For an RLC-circuit, the voltage measured over a series circuit can be expressed as

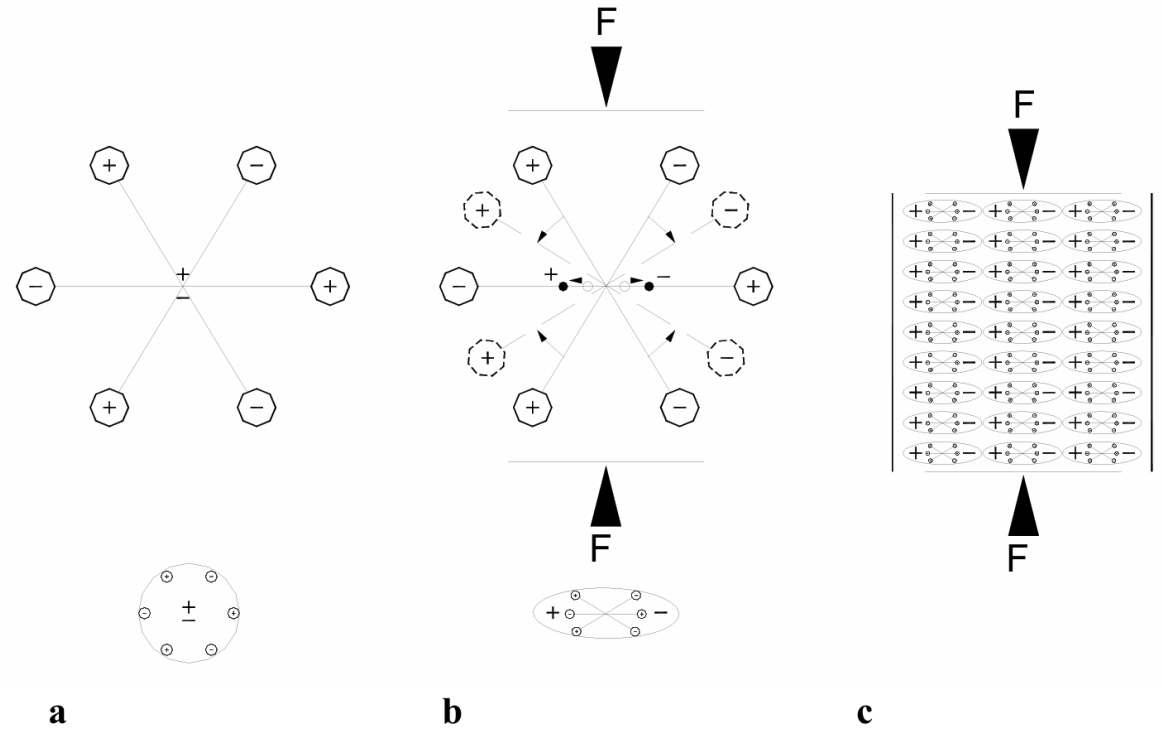

Figure 4.2: Schematic explanation of the piezoelectric effect: a) shows the neutral, resting molecule; b) the molecule subjected to a compressive force, creating a dipole, and c) the effect on the macroscale. Reproduced from [78].

$$V = R_m i_p + L_m \frac{di_p}{dt} + \frac{1}{C_m} \int i_p \, dt \tag{4.5}$$

where R_m, L_m and C_m are the resistance, inductance and capacitance that, respectively, form this circuit. If this electrical model is combined with a parallel capacitor C_0, it represents the real electrical impedance of the piezo near the resonance frequency. This model, also named the Butterworth Van-Dyke (BVD) model, is depicted in Figure 4.3.

According to this model, two types of resonances will be present. The first consists of a series resonance (f_s) in the so-called motional branch of the BVD model. Here, the resonance is dictated by the RLC circuit, modelling the piezoelectric crystal and it constitutes the minimum impedance. The second is the parallel resonance, which is also related to the parallel capacitor C_0. This constitutes the maximum impedance, because the current circulates between the branches [90].

In Figure 4.4, the different operating regions are demonstrated. Below the series resonance and above the parallel resonance, the capacitive branch is dominant. In between, the motional branch behaves inductively. This leads to a significant phase transition [91].

4.3.3 The quartz crystal microbalance

Quartz crystal has been used as a microbalance for its good sensitivity to mass loading. The electric parameters can be excellently linked to physical properties, which is convenient for a

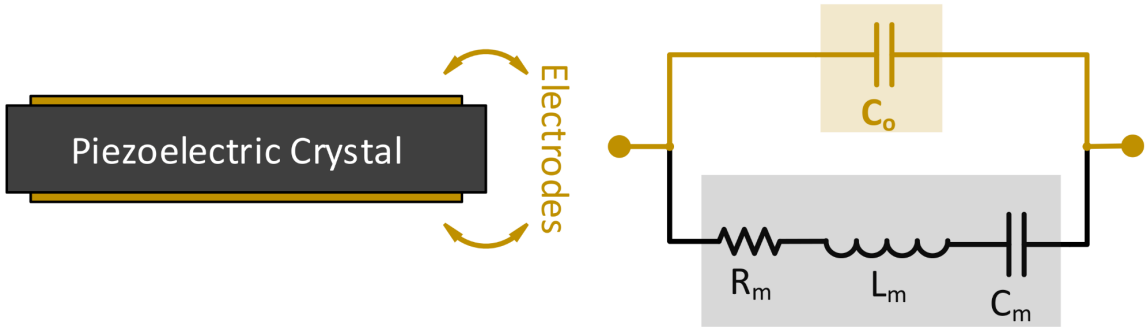

Figure 4.3: Illustration of the BVD-model with branches linked to the elements of the piezoelectric component. Reproduced from [91].

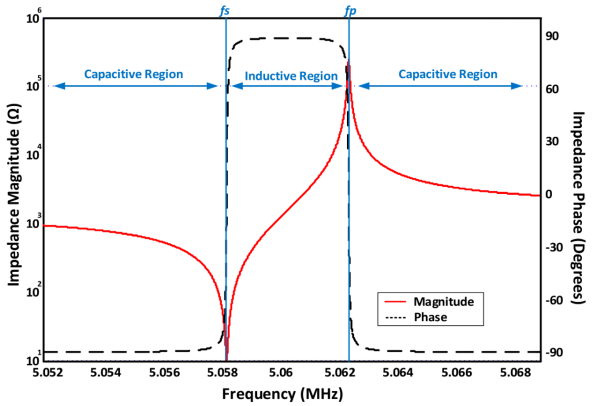

Figure 4.4: Typical frequency response for a quartz resonator. Reproduced from [91].

microbalance. As a surface mass is added, the resonant frequency decreases. Different cuts exists for quartz. These cuts determine the vibration mode of the quartz. An AT cut quartz crystal vibrates in shear mode and is most typically used for quartz crystal microbalances (QCM) [78]. The resonance frequency of the quartz is linked to its thickness. With increasing density and thickness of the film however, the microbalance enters the non-gravimetric regime, where the sensor also responds to the (visco)elastic properties of the load [78].

Sauerbrey equation

For small phase shifts, which occur in a thin film of rigid material, a uniformly distributed mass at the surface of the sensor generates a shift in the resonant frequency with the Sauerbrey equation [92]

$$\Delta f_s = -\frac{2f_0^2 \Delta m}{A\sqrt{\rho_q c_q}} \tag{4.6}$$

where f_s is the resonance shift, f_0 the unloaded frequency, m the mass, A the active surface area and ρ_q and c_q the density and elastic constant of the quartz, respectively. In this way, the frequency shift can be pertained to mass [92, 78].

Kanazawa-Gordon equation

For the same AT cut quartz, it is possible to recover the liquid density and viscosity of a Newtonian fluid. A shear wave has an extremely small penetration depth, so the liquid film can be considered semi-infinite. Under this assumption, the Kanazawa-Gordon equation can be retrieved [93]

$$\Delta f_s = -f_0^{3/2} \sqrt{\frac{\rho_l \eta_l}{\pi \rho_q c_q}} \tag{4.7}$$

where ρ_l and c_l denote the liquid density and viscosity, respectively. Both Equation 4.6 and 4.7 are instrumental in QCM applications, where for instance an absorbed mass in a (bio)chemical sensor or liquid density/viscosity is targeted [78, 94].

Other acoustic wave devices

Acoustic-sensors can be categorised as either a bulk acoustic wave (BAW) sensor or a surface acoustic wave (SAW) sensor. A BAW device measures through the bulk of the liquid, while a SAW device only measures on the surface. While the QCM is considered a BAW device, many BAW devices are not used for liquid measurements due to the limited propagation of waves in the liquid medium [78].

SAW devices offer good potential for in-liquid measurements. Surface transverse wave sensors can interact with a liquid medium, though mainly applied to chemically-modified surfaces measuring mass for in-liquid application [78]. Flexural plate wave sensors are most suitable to the measurement of fluid properties, but they consist of a diaphragm with a thickness smaller than the wavelength and are thus rather fragile [78]. Apart from quartz, a piezoceramic may also be used for mass measurements. It offers less performance. Especially for mass sensing in liquid media, the resonance peaks may not be extracted [95]. Interestingly, a SAW device was developed for measuring flow rate in a 6 x 5 x 2 mm channel. As heated water flows through the device, the flow of water disperses heat, thereby increasing the frequency of the device [96]. This is a calorimetric method of measuring flow rate, however, where it uses the frequency response to heat to indirectly measure flow, instead of the flow itself.

Piezoelectric benders

Amongst acoustic wave devices are piezoelectric benders, which are a specialized type of piezoelectric unimorph. A unimorph actuator consists of a single layer of piezoelectric material sandwiched between two thin electrode layers and bonded to an elastic substrate [97]. This configuration is known for its high displacement-to-voltage ratio [98]. As the name suggests, benders achieve displacement through the bending of a membrane induced by the piezoelectric layer's out-of-plane vibrations, as shown in Figure 4.5 [97].

The bending mechanism occurs because the piezoelectric element, bonded to a passive material, is constrained at the interface, allowing expansion on one side while the other remains fixed. This differential strain causes compression on one side and expansion on the other, resulting in bending. For further insights into the interaction between the piezoelectric and passive layers, refer to [98, 99, 100].

In our application, it is interesting to investigate the response of piezoelectric unimorphs, and particularly benders to mass and fluid loading. Microcantilever benders are commonly employed in mass detection [102, 98] and have also been explored for energy harvesting [103,

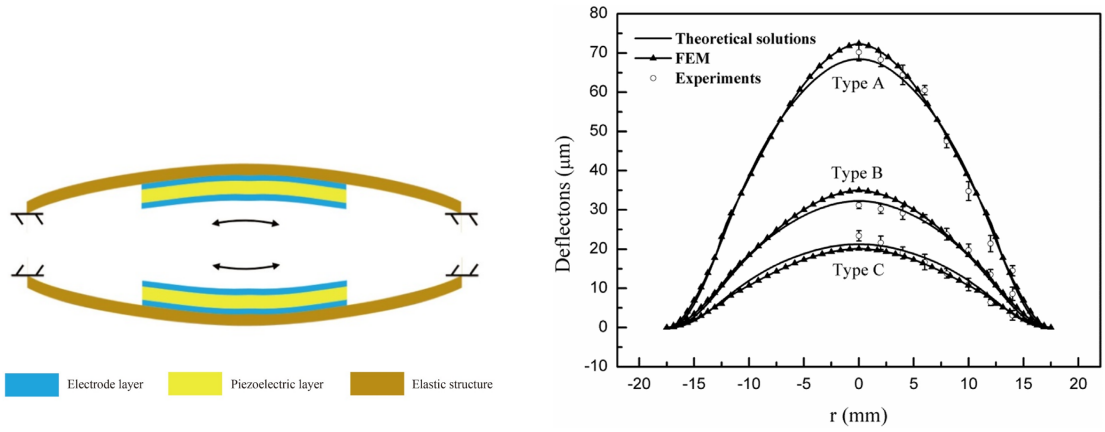

(a) (b)

Figure 4.5: (a) Schematic view of bending motion from a unimorph bender from [97]. (b) Displacement of the bender along its radius from [101].

104, 105]. When a point mass is placed at the cantilever tip, the natural frequency of the bender shifts according to:

$$\omega_0 \sim \sqrt{\frac{k_{eff}}{m_{eff}}} \tag{4.8}$$

where ω_0 is the natural frequency, k_{eff} the effective stiffness and m_{eff} the effective mass. For a cantilever bender, the stiffness depends on the width and length of the beam [98, 102]. The mass effect varies with its position along the bender [98]. This position dependence also applies to circular diaphragm benders, where flexure is greatest at the center, as depicted in Figure 4.5. A mass attached to the bender typically lowers the resonance frequency, a strategy used in both energy harvesting [106] and actuation applications [101].

The resonance frequency of circular benders is influenced by the thickness and stiffness of the passive layer, damping, and mass loading. Without mass, the resonance frequency increases with passive layer thickness; however, with added mass, this increase occurs at a reduced rate for the thicker layers [101]. Li *et al.* demonstrated this using a mass spring model to predict changes in resonance frequency for piezoelectric cantilevers attached to elastic bases, showing strong agreement with experimental data [105].

In piezoelectric diaphragms, where the passive layer does not fully cover the piezoelectric element, both bending and thickness modes can occur. For liquid sensing, the bending mode is preferred due to reduced damping [107].

At the micro-scale, piezoelectric micromachined ultrasound transducers (PMUTs) represent a class of benders with applications in medical ultrasound imaging, energy harvesting, and fluid sensing [108]. Fluid density can be estimated by a shift in resonance frequency [109]. The flow rate can also be estimated [110]. At a flow rate of 50 μL/hr a single PMUT cell was covered, exhibiting a shift, detected by a Laser Doppler Vibrometer. The flow rate could be determined by observing the start and end times of the resonant shift [105].

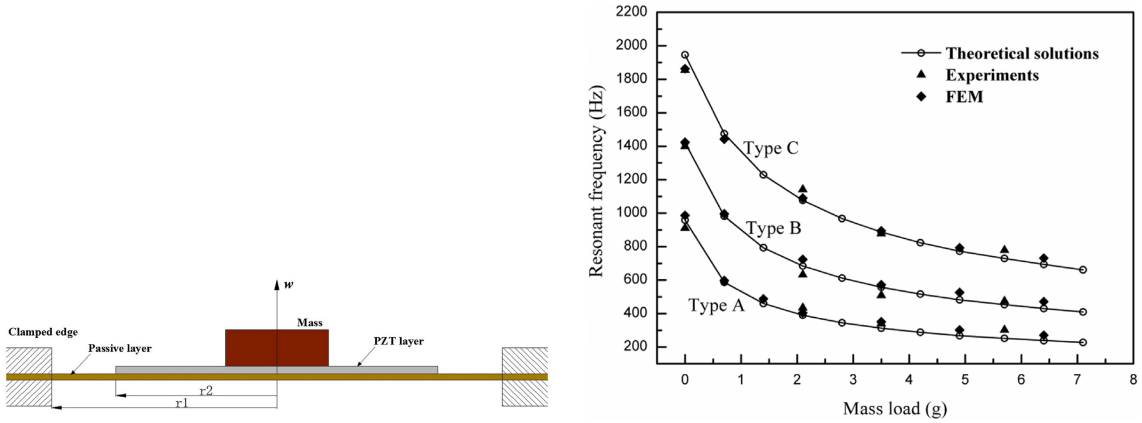

(a) (b)

Figure 4.6: (a) Schematic view of unimorph bender with a mass load from [101]. (b) Resonance shift due to mass loading for three types of benders from [101]. Type A has a thickness of 0.24 mm, Type B 0.36 mm and Type C 0.5 mm

Our case

For piezoelectric acoustic devices, liquid coverage or mass is rarely the target of the analysis. All the while, both quartz and bender resonators seem capable of doing so, but they have only be researched for full liquid coverage. In our case, the challenge will reside in that the sensor will never full be covered in liquid, it is position dependent, and will respond differently according to layers deposited on top. The overall shift in resonance frequency will be assumed to be a combined effect of mass, temperature and viscosity [91], summarised as:

$$\Delta f \approx \Delta f_M + \Delta f_T + \Delta f_L \tag{4.9}$$

where added mass may have the highest contribution [110, 102]. The improved understanding of microfluidics and piezoelectric resonance pave the way for the experimental development of our prototype sweat rate sensor.

Chapter 5

Experimental embodiment

This section will cover the different experimental facets of the thesis, alongside the development of the design. As described, the design of a microfluidic resonant flow rate sensor is embodied by obtaining a piezoelectric sensor and a microfluidic structure. The goal is to achieve a wearable flow rate test to assess the feasibility of resonance weighing in the field of sweat sensing. First, the fabrication of the microfluidic structure will be tackled. Then, the sensor selection and exploration will be discussed. Once the working principle is affirmed, the testing conditions can increase in complexity. The interaction of the microfluidic structure with the sensor is mapped as well. The design is later expanded by iterating the sensing reservoir geometry and introducing a resettability option to meet the requirements. In addition, a sweat collector is design to solidify the new measurement modality by performing a wearable test.

5.1 3D printing

3D printing creates a low-cost, simple and versatile way to prototype microfluidic structures [111, 112]. It will be frequently used in the experimental process to further iterate, test and gain insights. In the resonance concept, the flow rate sensor does not only consists of the piezoelectric transducer. Rather, it comprises of the whole complex of the transducer, combined with 3D printed microfluidics and thus must not be overlooked. Additionally, 3D printing was used to complete the design by printing the wearable collector. Printing channels with 3 degrees of freedom in the design was greatly beneficial, as will be evident later. Although a filament 3D printer for microfluidic application is technically possible, the performance of a stereolithography (SLA hereafter) 3D printer for microfluidics is considered superior, as can be seen in Figure 5.1 [111]. The resolution of optimised printers can go as low as 27 μm [112] and the porosity is less than with FDM techniques [111]. It operates by hardening a photo-sensitive resin in a layered fashion. The layers are hardened by an LCD screen selectively lighting up.

Workflow

After designing a microfluidic structure, it is supported, sliced and checked for errors in a free slicing software (Chitubox). The 3D printer in house was an Anycubic Photon Mono 1 (Anycubic) with an XY resolution of 0.051 mm and a Z resolution of 0.01 mm. The layer

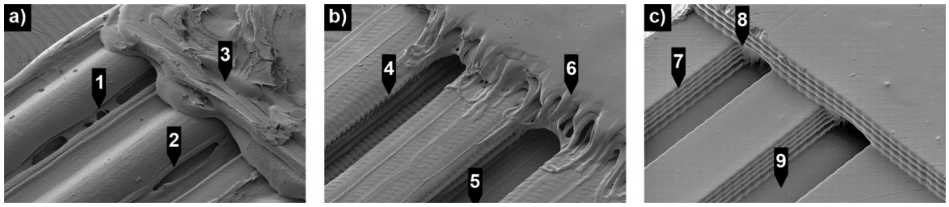

Figure 5.1: Comparison of 3D printing techniques for a microfluidic channel (300 um). a) Filament printed channels, b) fuse-jet printed channels and c) SLA printed channels. The numbers indicate printing errors

height is 0.051 mm, exposure time 0.5 s, and lifting speed 4 mm/s. The print is set at an angle to create the smoothest surface according to the arctan rule (angle of orientation = arctan(layer height/pixel width). If an arbitrary angle is chosen, the surface will be jagged, because the pixels or voxels do not fit perfectly in the orientation, as illustrated in Figure 5.2. Light but plenty of supports are used to assure the print is successful. Anycubic Clear photoresin (Anycubic) is used throughout most of the research and development. It was readily available and transparent which facilitates visual inspection during measurements. Moreover, the contact angle is estimated to be around 72°, visible in Appendix Figure B1, which is, for example more hydrophilic than typically used PDMS (106° without modification [113]).

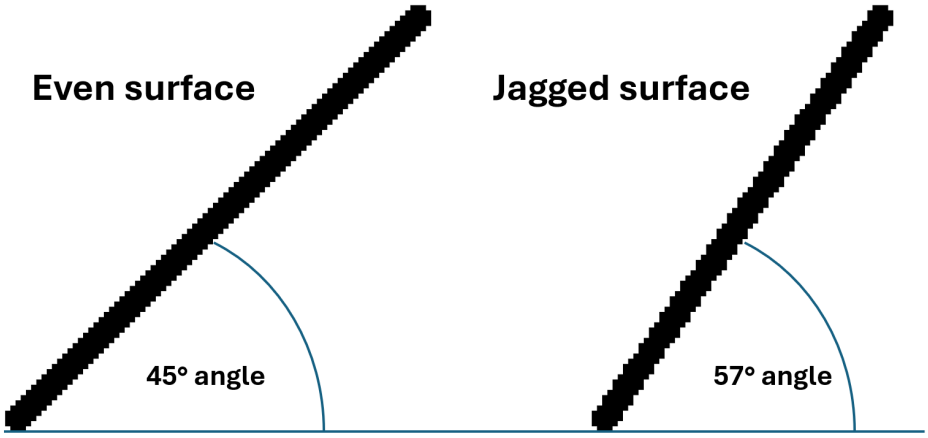

Figure 5.2: Illustration of the arctan rule for printing smooth flat surfaces

After printing, the supports are removed before the curing step, as seen in Figure 5.3. The prints were washed and stirred in isopropanol (IPA) multiple times. Hereafter, the prints are cured in the Wash-and-Cure (Anycubic) for 12 min, where the prints are flipped halfway through. They are then cleaned with IPA once again to ensure no resin remained uncured. Gloves and a filter mask are worn during the whole process. The printer was situated in a metal cabinet, containing a bathroom ventilator to output fumes outside a window. The space was properly ventilated as well. The waste products are properly disposed of and any area that might have been in contact with resin is cleaned with IPA. The physical printing set-up is found in Appendix Figure B3.

Figure 5.3: A) Build plate with finished prints and B) Prints under UV curing after support removal.

5.2 Sensor selection and characterisation

The first step to evaluate the new measuring modality is to select a piezoelectric sensor. The cost of a quartz crystal is high (≥100 EUR), thus cheaper, piezoceramic options are investigated, costing as low as 6 EUR a piece [114]. Although they do not match the quartz crystal in mass sensing performance, it might still serve as a microbalance. To accelerate the process, commercial sensors were acquired instead of creating the piezo-electric from scratch.

The following aspects are taken into consideration: size, resonance frequency, contact, application and costs. The sensor should be compact to fit in a wearable device. In addition, the resonance frequency is varied to investigate whether a certain bandwidth accommodates liquid sensing more than others. The type of contact is also important, because it must be approximately flat to create a microfluidic chamber for small volumes. This is also intertwined with the application of the sensor. Most sensors are applied to gas sensors, or time-of-flight sensing. Some of these sensors have a roster or a grid covering the piezoelectric element and cannot be used. The costs also influenced the sensor selection.

From the search, three sensors are further explored. The first sensor is an ultrasonic transceiver (CUSA-TR65-065-2200-TH68, Same Sky) with a resonance frequency of 40 kHz. The dimensions are Ø14 x 9 mm. The piezoelectric element is covered by an aluminium cap, resembling a unimorph bender, see Appendix Figure B4. Unlike a quartz crystal, which has different types of cuts, the vibration mode can be approximated as longitudinal, with a directivity of around 60 degrees for around X-axis and 120 degrees for the Y-axis. It is intended for distances between 0.4 and 6.5 meters. As a transceiver, it can both act as a transmitter and receiver, and this type of sensor is likely used in the automotive industry as a parking sensor for instance.

The second sensor operates at 120 kHz (ND18X2N6, KEMET). The dimensions are Ø18 x 2 mm. This piezoelectric can be used for ultrasonic cleaning, levitation, and as flow and level meter amongst others. The sensor is relatively large in diameter, but smaller in height

than the CUSA sensor. This disc geometry is better for wearable applications.

The third sensor is an ultrasonic bender (UB161M7, PUI Audio), which resonates at 1.7 MHz. It is designed for high voltage circuits, meant for ultrasonic cleaning or atomisation. Ultrasonic benders have a higher displacement, by adhering a neutral material to the piezoelectric material. Since this bender could act as an atomiser, it could provide a means of expelling fluid. The dimensions of Ø16 x 1.23 mm are also attractive for integration into a wearable device.

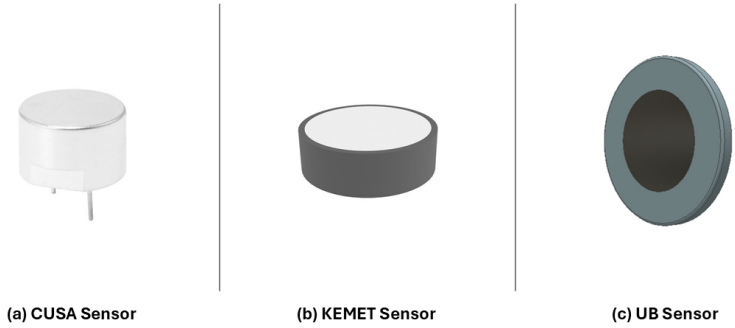

Figure 5.4: The three different sensors

The sensors are evaluated using an oscilloscope (DSO3152A, Agilent) and a function generator (33220A, Agilent), with the latter providing a 10V amplitude sine wave to drive the piezo element. Two readout circuits were tested. The first monitors current changes using a 510Ω resistor in series with the sensor, measuring the voltage drop caused by deformation-induced currents. The second uses a high-resistance (100 kΩ) series resistor to measure the voltage directly across the sensor, limiting current to isolate voltage changes.

The resonance frequency is identified by manually adjusting the sine wave frequency and observing the peak-to-peak voltage ($V_{\text{P-P}}$) on the oscilloscope. If the signal is weak, noisy, or unclear, the readout method is switched between current and voltage measurement. Once the resonance frequency is located, a droplet is applied to the sensor's center, testing its fluid sensitivity by observing any resulting frequency shift.

Figure 5.6 displays the results of the droplet test for each of the sensors. The KEMET sensor under air and fluid loading maintains its original resonance frequency around 120 kHz. The UB sensor responds to fluid loading, but not in a stable fashion. The signal is irreproducibly distorted or damped for the same volumes without a significant frequency shift. The droplet was also visibly vibrating. Both the KEMET and the CUSA sensor show clear resonances. The UB sensor was also tested in current measuring mode, where it only displayed a rather distinct resonance at 1.9 MHz. Opposite the other sensors, the CUSA sensor, with a resonance around 41 kHz, shows an evident shift under fluid loading, plotted in Figure 5.9. The signal is also free of distortion. For this reason, the CUSA sensor was selected for further development.

The droplet test in Figure 5.9 explores volume quantification by pipetting droplets onto

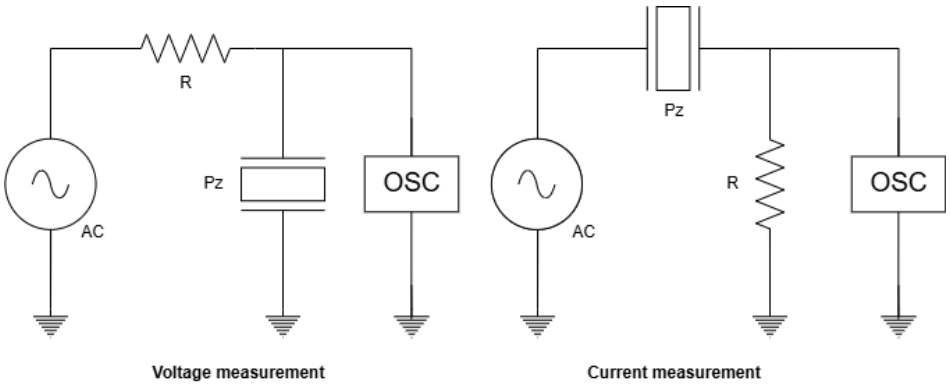

Figure 5.5: The set-ups used for sensor characterisation using an oscilloscope and waveform generator. AC is the waveform generator, R the resistor, Pz the piezoelectric element and OSC the oscilloscope.

the sensor's surface and measuring the resulting frequency shift. The shifts show good proportionality to droplet volumes, with slight distortion near 37 kHz. The resonance frequency is taken at the maximum voltage, and the resonance frequency is plotted against mass in Figure 5.8 and fitted to a mass-spring resonance ($R^2 = 0.98$), according to

$$f_r = \frac{1}{2\pi}\sqrt{\frac{k_{eff}}{m_{eff} + \Delta m}} \tag{5.1}$$

where f_r is the resonance frequency, k_{eff} the effective stiffness, m_{eff} the effective mass without fluid loading, Δm the (virtual) added mass of the fluid. It is assumed that inertial forces dominate over elastic forces. The effective stiffness was estimated at 12 N/m and mass at 179 mg.

The next step is to examine the position dependence of the sensor. At close-distance measurements, or direct contact, this is especially important. The maximum intensity is expected at the centre of the sensor with a decrease laterally, because the nature of an ultrasonic bender [115], see Figure 4.5. 4 distances were taken for assessment, namely r=[0, 2.5, 4, 6] mm. In Figure 5.8, it can be seen that the sensor measures well within a 2.5 mm radius. Outside, the error is too large to provide a reliable measurement.

5.2.1 Integration of microfluidic structure

For wearable microfluidic sweat sensing, the sweat must be collected and transported to the sensor in a channel. Thus far, no material in between the sensor and the fluid is used, because the case had been deconstructed into fundamental testing conditions: can we measure and quantify fluid on a bare sensor? Now, these conditions are expanded to measuring fluid in a 3D printed microfluidic channel.

A closed microfluidic channel does not provide direct contact with the sensor. An open channel allows for better contact, but requires an intermediate material to prevent leakage. A bi-adhesive tape was thus used (3M 1522). The tape is hydrophobic (contact angle = 106°, Appendix Figure B2). The amount of tape layers was varied during droplet tests, as plotted in Figure 5.9. With each added layer and without added mass, the resonance decreases linearly.

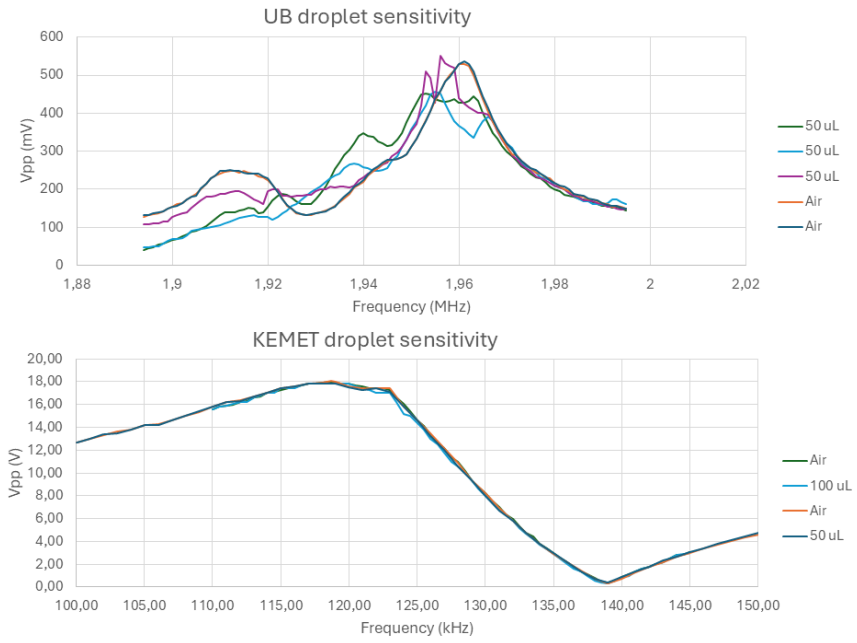

Figure 5.6: Results of the droplet tests for the UB and KEMET sensor.

The tape is treated as an extension of the passive layer when fitted. The fitted stiffness lowers with each layer, which is expected from springs in series [116]. The different slopes, especially when comparing layers with no layers, may arise from the way added mass translates the curve according to Equation 5.1. This is not evident for the passive layers in Figure 4.6b, because here stiffness effect may be greater than the mass effect.

Initially, the effects of a constant solid mass loading are thought to be little compared to fluid loading up to 20 μL, as visible in Figure 5.10, because the tape exhibits a shift of around 1 kHz from the sensor and print, although dampening is significant. Interestingly, the shift is significantly larger than for the droplet tests without a print. In addition, 3D-printed cylindrical weights were tested on the sensor with and without the adhesive tape (Appendix Figure B6). With direct contact, the resonance increases in a linear fashion (below 1 kHz). The effective weight of the masses is difficult to ascertain due to the non uniform displacement profile. It may be that the weights only increase the stiffness of the membrane. For the same mass test, but now with the mass on the tape, the following results are found: for the smallest weight the shift was negative and high, the second was close to the original resonance and the third and fourth weights did not express resonance. A dynamic system with a coupled mass resonator model with damping may explain these results. These effects will be further expanded upon in Appendix C.3.

The sensitivity orientation of the sensor's surface also had to be taken into account, because the sensor showed asymmetric directivity in x and y direction [114]. This dependence upon close contact was uncovered by placing strips of tape in the x, y and xy direction, for which the results are found in Table B1. The biggest difference was found between the x and y direction. This may cause an error of 1 kHz in the absolute resonance values, if not considered. For subsequent testing, the orientation was kept constant.

After the sensor characterisation, the sensor is finally tested with a static filling condition.

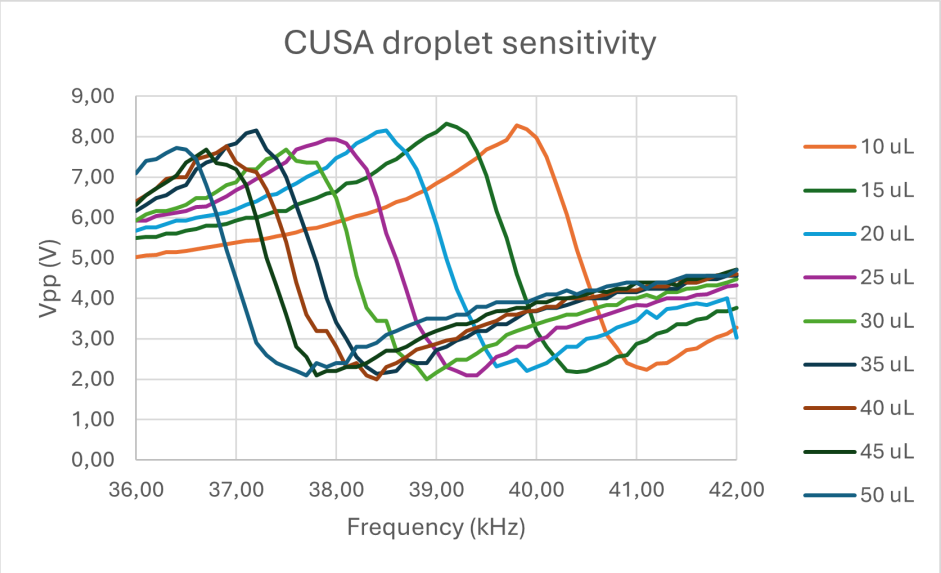

Figure 5.7: Raw data of droplet testing of the CUSA sensor.

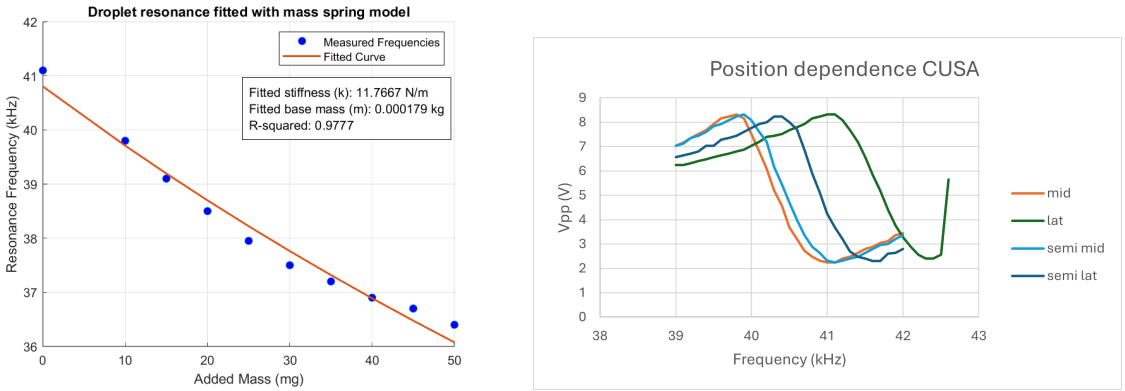

(a) (b)

Figure 5.8: (a) droplet testing results fitted to a mass spring system and (b) position dependence of the sensor. The droplet calibration was performed with and without bi-adhesive. The tape measurements were discontinued due to an unstable signal at higher volumes due to atomisation. The position dependence was tested for $r = [0, 2.5, 4, 6]$ mm.

A volume of 10 and 20 μL was injected in an SLA printed reservoir (2.4 mm radius), containing two holes (r=1 mm). The reservoir was the size of the approximate 'sweet spot' of the sensor established earlier. The plot in Figure 5.10 shows good results, as the resonance peaks are clearly discernible.

5.3 Design iterations: sensing area

The sensor has demonstrated the ability to measure droplets of varying sizes and distinguish between different volumes, marking progress towards a wearable sweat sensor. The focus

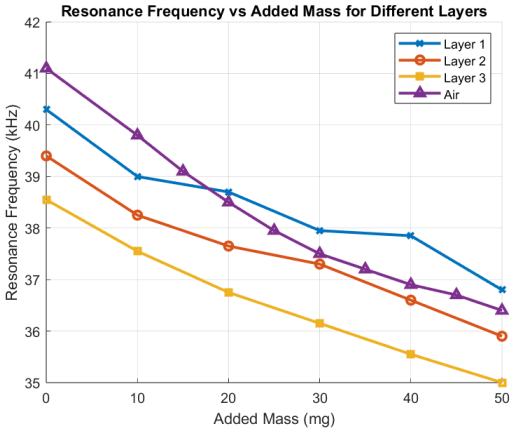

Figure 5.9: Droplet sensitivity with varying amount of tape on the sensor.

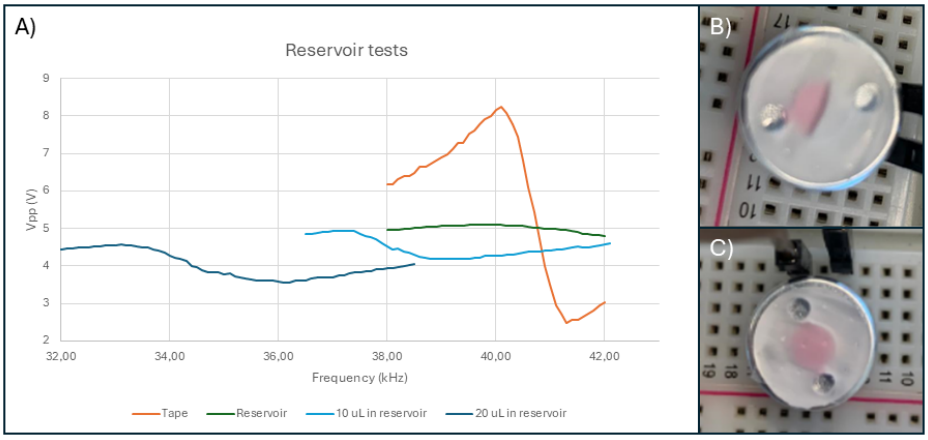

Figure 5.10: A) Static filling of a reservoir with water. B) 10 μL in the reservoir. C) 20 μL in the reservoir.

now shifts to designing an optimal microfluidic structure to meet the requirements. This section outlines the measurement protocol using an updated setup, which will help evaluate the microfluidic geometry, scale, and sensor contact most suitable for resettable sweat rate measurements.

Basis design

The basis device geometry consists of a thick membrane (2 mm or 1 mm) and contains 1 mm or 0.5 mm rectangular channels and a sensing area. An adhesive strip is placed between the print and the piezoelectric sensor. The side columns allow for fixation on the sensor. A Luer slip connection was modelled to make the flow rate sensor prototype compatible with a syringe. At the outlet, a cavity was made to hold a wick for absorbing the fluid. The design is depicted in Figure 5.11.

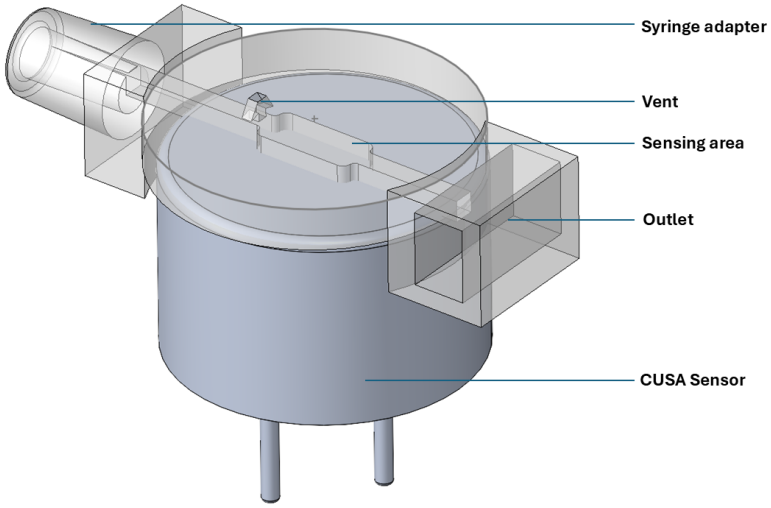

Figure 5.11: Basis membrane design of sensor.

5.3.1 Measurement protocol

A syringe pump (KD Scientific) is used for enabling measurements with set flow rates. Coloured demi-water (Brilliant Black dye) is used to visualise the flow within the channels. Before each measurement, the bi-adhesive is added to the sensor. The print is pressed on top. Initially, the print and tape were removed after the measurements. However, at a later stage it seemed less variable to reuse the print and tape, because different tape sizes could cause variation. The channels were emptied with a wick, followed by blowing the channels clean with 2 bar air pressure. A vacuum pump was used as a final measure to ensure no fluid remains in the channel. The set-up can be seen in Figure 5.12.

A syringe pump (KD Scientific) is used to enable measurements at controlled flow rates. Colored demi-water (Brilliant Black dye) visualise flow within the channels. Before each measurement, bi-adhesive tape is applied to the sensor, and the microfluidic print is pressed on top. Initially, the tape and print were removed after measurements, but reusing them was deemed superior, because it reduces inconsistencies. Channels are emptied using a wick, followed by cleaning with 2 bar air pressure. A vacuum pump ensures no residual fluid remained. The experimental setup is shown in Figure 5.12.

An impedance analyser (E4990A, Keysight) was used to swiftly analyse the resonance frequency. It plots the impedance against a range of frequencies in a 1V frequency sweep. The output is demonstrated in Figure 5.13. The resonance can be tracked by using built-in markers for peak detection. The impedance analyser is not typically used for continuous measurements. The output can be saved manually, but this does not provide good temporal resolution. In order to solve this, external communication is set up with Keysight Connection expert. In Excel Visual Basic for Applications, the values of two markers are continuously saved. This data is further analysed in Matlab (Mathworks).

Evaluating the sensor response

From the characteristics of the impedance graph, the most reliable way to measure the frequency shift is found. The series and parallel resonance are considered, as well as the peak

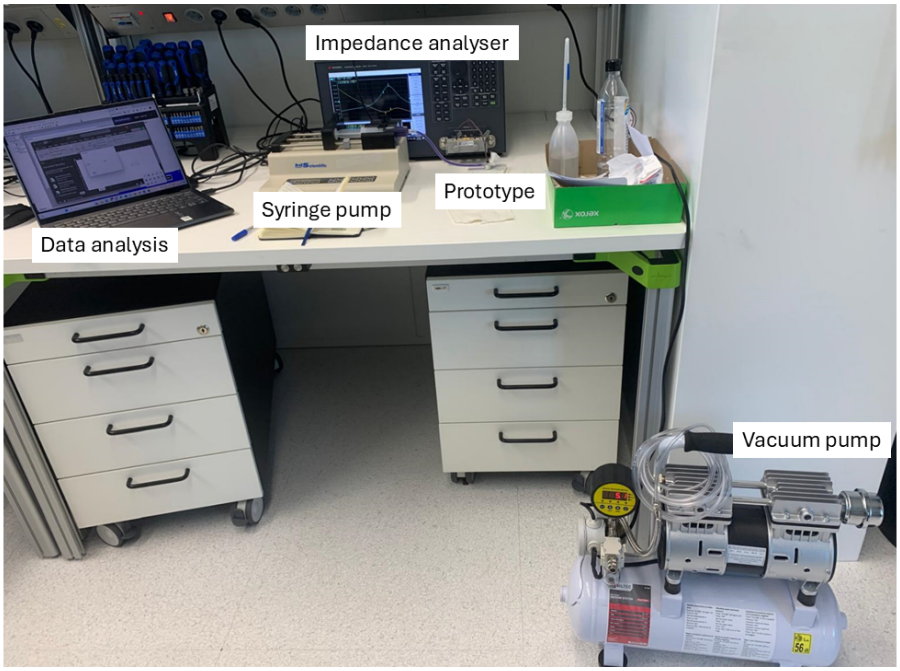

Figure 5.12: Experimental set-up, air pump not in picture.

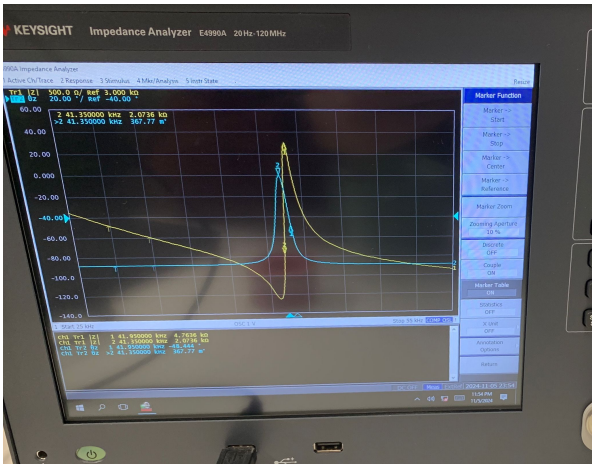

Figure 5.13: Impedance analyser with the markers set on the parallel resonance and the phase peak.

phase in between and the impedance magnitude. The peak phase was the most consistent, followed by the parallel resonance, which is why these were tracked. An example output of the data analysis algorithm is provided in Figure 5.14. For clarity in the next figures, only the phase is depicted by default. If relevant, other traces are plotted.

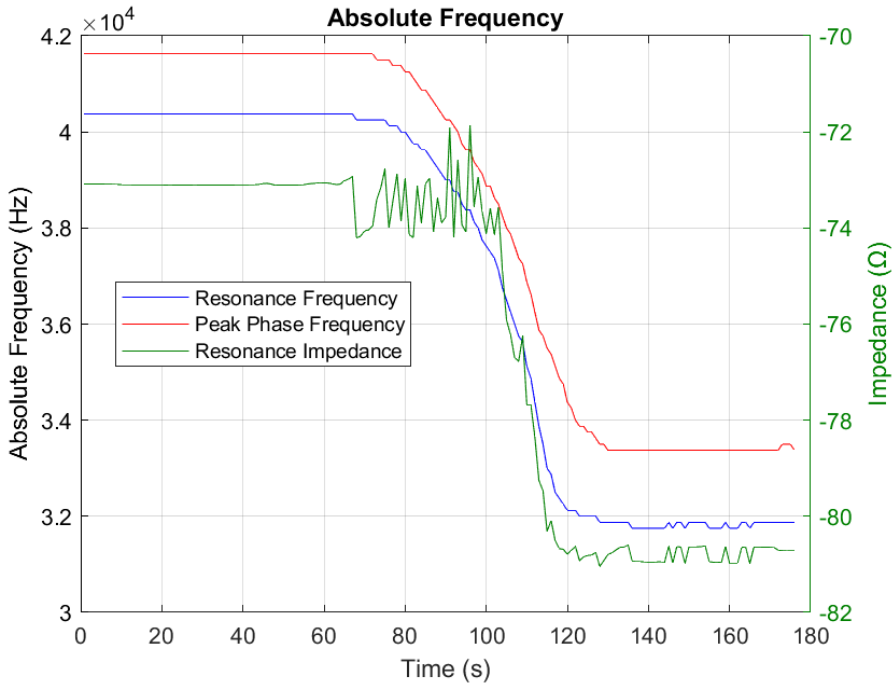

Figure 5.14: Example output of filling cycle of the flow rate sensor. Here, the series resonance is tracked instead of the parallel resonance.

5.3.2 Optimisation methods

Geometry

Now that the sensor behaviour is better understood, it is time to find the best shape for measuring flow. To this end, four geometries were tested: a linear channel, an arced channel, a circular reservoir and a rectangular reservoir, as described in Table 5.1 and depicted in Figure 5.15. The trade-off in these concepts lies the amount of volume that is measured in one filling cycle and in the coverage of the sensor. A large sensing area can be more sensitive to motion, because the fluid is less confined. On the other hand, it also conveys more information on sweat rate because of a longer measurement time.

Size

The size of the channels determines the amount of fluid on the sensing area. It also governs the filling time of the device. For this reason, the device should be as small as possible to limit the delay between the start of sweating and the passage of sweat over the sensing area. Two rectangular channels sizes were investigated for the proof-of-principle design: 1 mm and 0.5 mm channels. This was done for the linear channel and circular reservoir design.

Contact Area

The contact area between the printed membrane and the piezo surface can affect sensor performance. Excessive dampening can hinder peak detection, so maximising sensor response is crucial for analysis. Two types of contacts were evaluated: a solid disc design and a

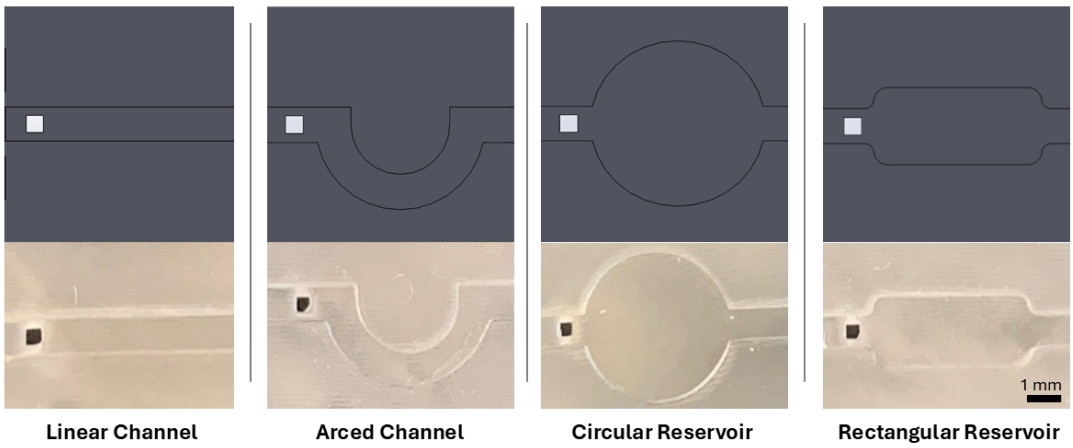

Figure 5.15: Tested geometries.

Table 5.1: Summary of Channel and Reservoir Designs

Design	Description
Linear channel	A straight channel over the sensor, simplest geometry. Does not account for non-uniform sensor response, potentially reducing measurement precision. Small total shift expected due to low volume.
Arced channel	Arc-shaped channel with constant radius to address position dependence. Suitable for measuring outside the sensor's sweet spot. Works best with smaller channels and has a small volume.
Circular reservoir	Covers the sweet spot of the sensor completely, maximizing response. Volume of approximately 18 μL, but larger size may increase susceptibility to motion effects.
Rectangular reservoir	Widened channel at the sweet spot, with a volume of about 11 μL. Close contact with walls helps restore fluid front for refilling.

channel wall design. The solid disc design covers the whole adhesive on the sensor and acts as a membrane (Figure5.16). Only the outline of the channel contacts the sensor in the second design. It is expected that this minimal contact results in the least interference from the channel structure.

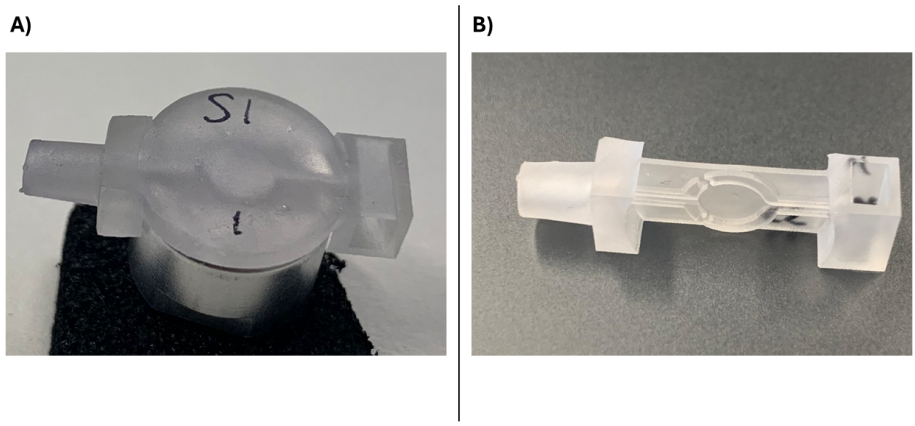

Figure 5.16: A) Solid reservoir design, where only the sensing area and channels are not in contact with the tape. The rectangular darkening is the tape. B) The contour reservoir design where only the extruded channel walls contact the tape. This version also contained air vents on the sides.

5.3.3 Optimisation results

What is the best geometry?

Each channel geometry was tested in duplo at a flow rate of 20 μL/min. In Figure 5.17, the geometry results are plotted. From the plots, it seems that starting frequency drops significantly for the channel designs. The shift is also marginal compared to the reservoir designs. The difference between the channels and the reservoirs is of a surprising magnitude. Channels designs have a starting frequency of $\pm$34 kHz and shift on the order of $\pm$0.1 kHz. Reservoir designs both have a starting frequency of $\pm$43 kHz and a shift on the order of $\pm$7 kHz, despite the different reservoir volumes. It may be that the reservoir designs facilitate bending more, creating a region where the bender can resonate more freely, loosely clamping at the sides of the reservoir, decoupling the print. The channel designs cover these regions, as benders can showcase complex coupling of modes and geometry-dependent effects [101, 105, 117]

The rectangular reservoir provides a higher shift relative to its volume that the circular reservoir, although the reproducibility of the shift was occasionaly impaired by leakage. Apart from this, discrete steps in the measurement stand out. This is especially evident because of the smaller plotting scale in the left graph in Figure 5.17. This is an artefact from the analyser settings, as the peak detection for the frequency using trackers has a lower sampling time than the magnitude. Due to the larger shifts, this artefact interferes less with the measurement for the reservoir geometries. These facilitate a characteristic sigmoid shape, which might also be present in the channel designs, were it not for the sampling issue. Nevertheless, to validate the working principle, the reservoir approach was deemed superior, because of the larger shifts. In addition, the longer filling times are also considered an advantage of a bigger reservoir. One thing to consider in the reservoir designs is the movement of fluid as an effect of orientation differences. This affects the circular reservoir the most, although full reservoir

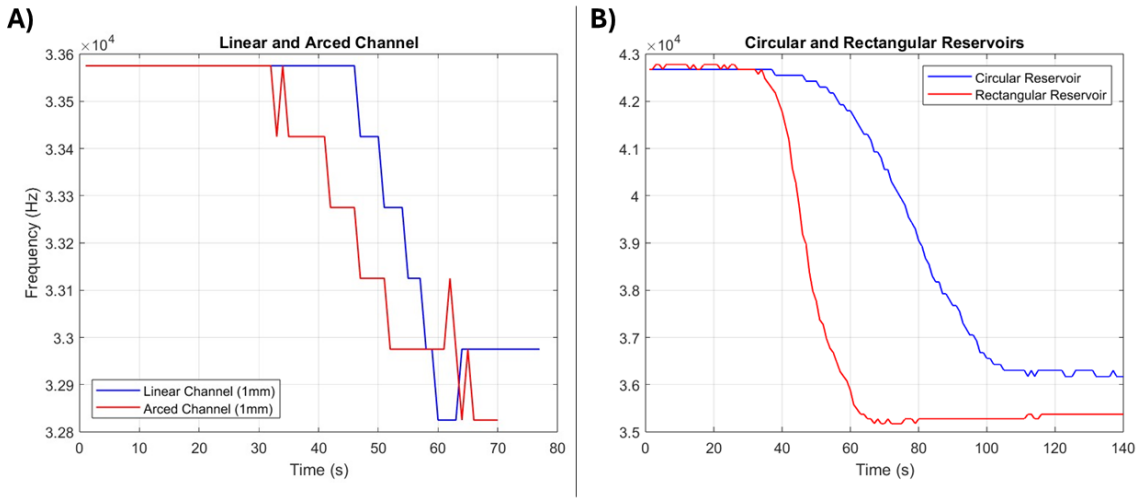

Figure 5.17: A) Results of varying channel geometry and B) reservoir geometry.

filling is achieved before proceeding into the channel, visible in Appendix Figure C1.

What is the best scale?

The effects of scale has been investigated for all channel types, but only the reservoir designs were considered in Figure 5.18. The rest of the results can be found in Appendix Figure C4. For the reservoir design, only the height of the reservoir was varied. The circular reservoir had an issue at 0.5 mm, caused by the occurrence of another phase peak at a lower frequency with a higher magnitude. The tracker follows the highest peak. As water fill the channel, the damping increases by viscous effects. The peaks merge and during this process the tracker suddenly switches to the other peak. Moreover, the presence of two phase peaks prior to fluid loading is different from the 1 mm channel and is likely cause by the different thicknesses of the membrane. The 0.5 mm channel size was 1 mm thick and dampens less than the 2 mm thick membrane for the 1 mm channel. For the 2 mm thick membrane the peaks can be merged through damping or the mass is decoupled (Appendix C.3 for dynamical model).

The shift, once the peak is merged, seems similar to the 1 mm height reservoir. This is an indication that the sensor might not selectively measure mass, but that it also sensitive to the degree of surface coverage. The rectangular reservoir shows a lesser shift for the smaller scale. For the proof-of-concept, a reservoir with channels of 1 mm are opted for to provide the most stable results.

What is the best type of contact?

In Figure 5.18, the sensor response under flow is depicted using a circular reservoir geometry. Surprisingly, the contour design starts at 34 kHz with a 0.2 kHz shift, despite weighing less and having less contact than the solid design, which starts at 42 kHz with an 8 kHz shift.

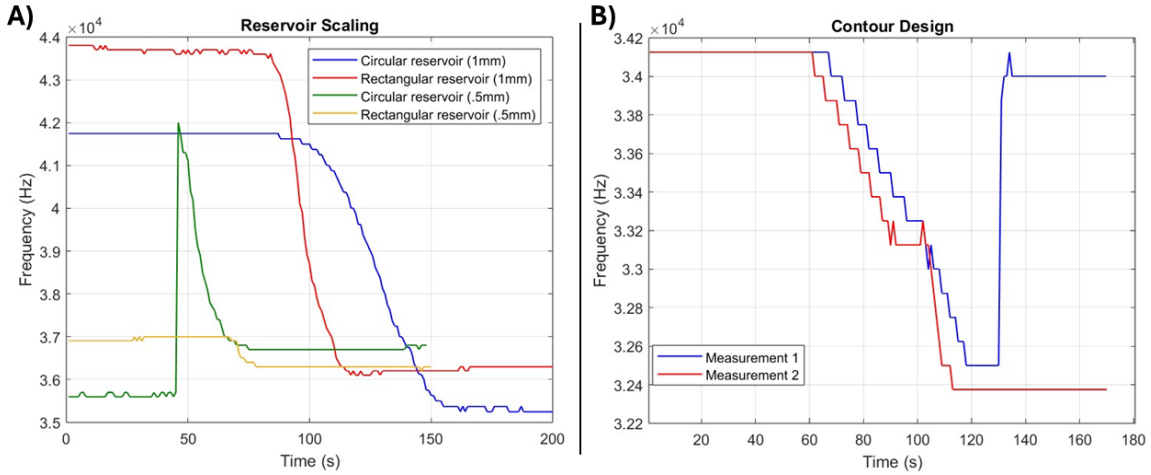

Figure 5.18: A) Results of varying scale. B) Results of varying the type of contact with the sensor.

Similar to the channel size, the thinner material reduces damping, which may explain this initial frequency being lower as two peaks are distinguishable. This trend was assessed in Appendix C.3.

Further testing continued with the solid design, 1 mm channels, and a reservoir, because they were easier to analyse and provided the highest shifts. No preference has been established between circular and rectangular reservoirs thus far, but this will be addressed in the next section on channel resettability.

5.3.4 Channel Resettability: Wick concept

For wicking, various methods were considered, including an atomisation and inkjet-inspired approach. However, these are found to be ineffective at voltages up to 10V, and higher voltages are unsuitable for wearables due to safety concerns. Instead, a wick was incorporated into the design for simplicity, inspired by Liu *et al.* [41].

A wick, placed at the end of the channel, absorbs fluid once reached and resets with the next contact. Unlike Liu's design, which emptied arbitrary channel segments, our focus was on wicking the reservoir specifically. An air vent near the reservoir's upstream end ensures effective fluid separation by balancing air pressure. Without the vent, wicking fails.

Figure 5.19 shows wick performance and highlights the principle. A wick chamber at the channel outlet facilitates fluid removal. While the circular reservoir is often emptied for one cycle, achieving multiple cycles remains challenging, as discussed below.

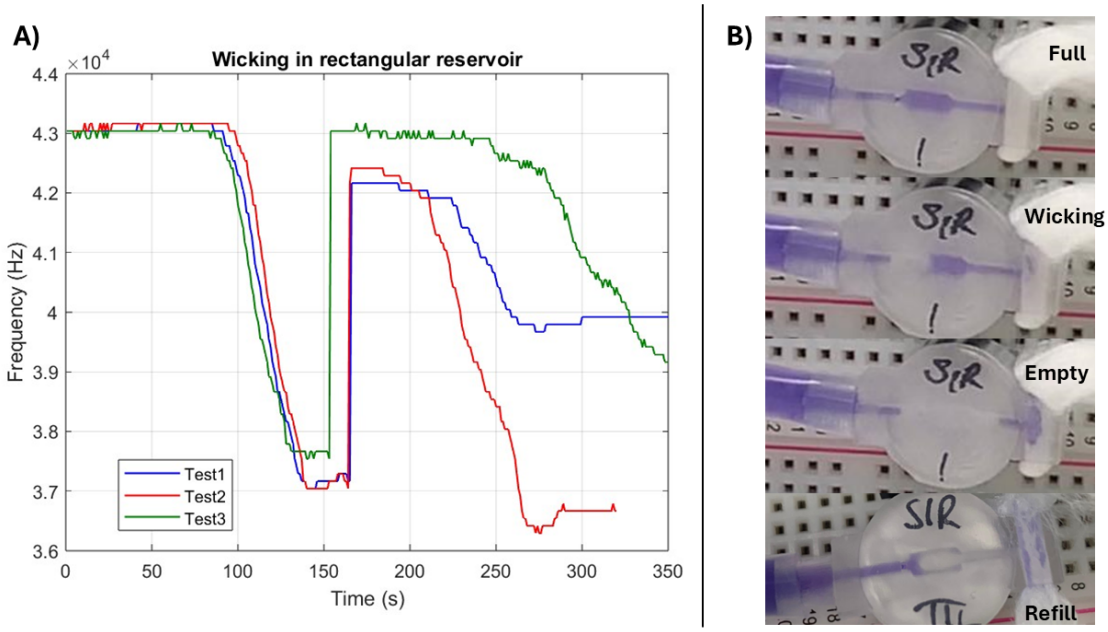

Figure 5.19: Wicking behaviour of the sensor. A) Two filling cycles as seen in the data and show bad reproducibility of the trend of the first filling. B) The first three images show a wicking event, the fourth (from another measurement) shows the restoration of the fluid front, eventually refilling the reservoir completely.

Wicking Challenges

After the frequent initial wicking event, it was rare to obtain a second wicking event. Three modes of failure hindering this are: 1) vent leakage, 2) continuous sideflow and 3) issues at the outlet.

1. **Vent leakage**
   Initially, the vent was designed as a simple (rectangular) opening in the design, tested in 300 and 500 μm size. The latter was preferred 500 μm vents, showing less printing defects.

   However, leakage occurred through the square vents. In order to prevent this, capillary bursting valves are implemented as stop valves. The geometry of the valve is depicted in Figure 5.20, containing a 118° angle. This limits vent leakage by increasing the Young Laplace pressure from -89 kPa to 199 kPa.

2. **Continuous sideflow**
   Continuous wicking after an initial wicking event prevents the reservoir from filling, as seen in Figure 5.21. The bi-adhesive tape is hydrophobic (contact angle = 106°). This directs flow laterally over the printed walls. In corners, the contact angle is larger, making it more attractive for fluid to reside there. After wicking, the sweat residue at the sidewalls prevent a fluid front to be restored, leaving a gap in the centre of the reservoir. The same issue was brought up by Bariya *et al.* [52].

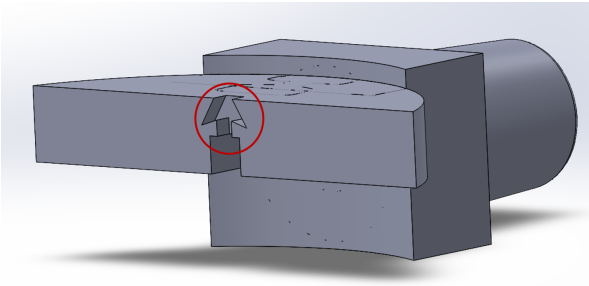

Figure 5.20: Placement of a capillary bursting valve upstream the reservoir to prevent leakage throught the air vent.

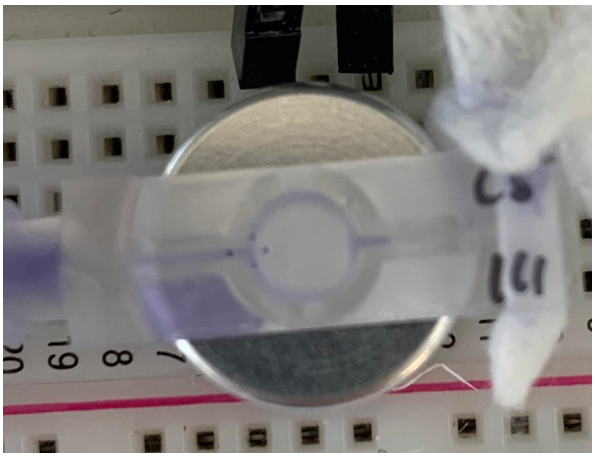

Figure 5.21: The sideflow 'steady state' after a wicking event for the circular reservoir for a contour contact area print. Additionally, there is leakage at the inlet.

To improve wicking, the sidewall can be made hydrophobic, because this reduces the discrepancy in wettability of the two channel interfaces. Vaseline is smeared on the sidewalls of the circular design to assess the feasibility of this. This facilitated multiple wicking events.
Vaseline is not an ideal choice, however, because it retains fluid by its irregular deposition at the sidewalls. In addition, the crude deposition also changes the geometry of the reservoir. Therefore, it is not quite clear whether hydrophilicity or geometry change was crucial. The rectangular reservoir design addressed these issues by slightly widening the channel, allowing sideflows to converge and restore the fluid front (Figure 5.19B). See Figure 5.19B for the restoration of the fluid front. For this reason, the rectangular reservoir design was chosen for the wearable prototype.
However, because the fluid front is restored under the sideflow, the results are not very reproducible, as is evident in Figure 5.19A. The filling rate slow, as the fluid is still being absorbed. A different adhesive or modification could improve reproducibility. Interdigitated 'teeth' are tested, for instance, for promoting serpentine refilling. While this is observed for primary filling, it actually prevents a second filling event. The teeth do not contact the adhesive to not interfere with the signal. Yet, the resonance frequency and shift magnitude are considerably lower and smaller compared to the blank rectangular reservoir, visible in Appendix Figure C8, similar to previous tests. Because

of a different structure, it may be that the stiffness is altered, influencing the dynamic response of the system. Another option for promotoing flow can be to create grooves at the top of the reservoir for directional capillary flow [38].

3. **Outlet issues**
   In the first iteration of wicking, resetting often failed due to insufficient volume removal. This issue occurs when only a small segment of the distal channel is emptied, primarily at lower flow rates (3, 6, 9 μL/min). Air entering through the outlet, often due to uneven or insufficient contact with the wick, is the main cause.

   While the initial wicking event is usually successful, subsequent attempts rarely succeed because the wick becomes saturated and cannot compete with the flow rates. A saturated wick increases fluid resistance, leading to vent leakage. After mitigating sideflow issues through the rectangular geometry, impaired wicking remains the primary failure mode, requiring further investigation.

5.3.5 Multiflow measurements and reproducibility

From the two reservoir designs, the rectangular reservoir performed better when wicking was considered. Therefore, further testing proceeded with this reservoir. This started with creating a dataset of different flow rates. The measurements were performed in triplo with flow rates 3, 6, 9, 12, 15 and 18 μL/min. The results can be found in Figure 5.22. Already, the different flow rates can be intuitively discerned, but some variance was observed in the slope and final frequency, with lower flow rates yielding lower final frequencies. Reproducibility testing revealed robustness under different orientations, but day-to-day variations in frequency shift magnitudes, with differences of up to 1 kHz, visible in Appendix Figure C2 and C3, respectively. The dataset depicted in Figure 5.22 forms the basis for the flow rate characterisation detailed in Chapter 6.

5.3.6 Discussion

In this section, a design was developed for measuring flow by using a low-cost piezoelectric element. This constituted of sensor selection and characterisation, designing and 3D printing of microchannels, and creating a set-up for capturing the sensor response to fluid loading. A quartz crystal microbalance is the golden standard, but piezoceramic sensors can also show promising results.

Three sensors were tested on fluid loading, which should be expanded in the future. Yet, one of the three showcased strong results. The CUSA sensor was responsive to fluid loading, even through multiple layers of a bi-adhesive tape. The interaction could be modelled as a mass spring system. The sensitivity of the sensor was considered uniform at the centre region of the sensor (r=2.5 mm). To confine and direct fluid over the sensor, rapid prototyping was done via SLA printing. A syringe pump was used to investigate different geometries, scale and surface contacts. A higher frequency shift was exhibited for fluids contained in a printed structure. Furthermore, an attempt was made to make the device self-resettable. The rectangular reservoir showed the best potential for (repetitively) measuring sweat and was measured over a broader range of flow rates.

A dynamic system's approach was taken to interpret the results. However, a detailed analytical description or simulation should be investigated for a bender under partial fluid loading in a channel to provide more insights.

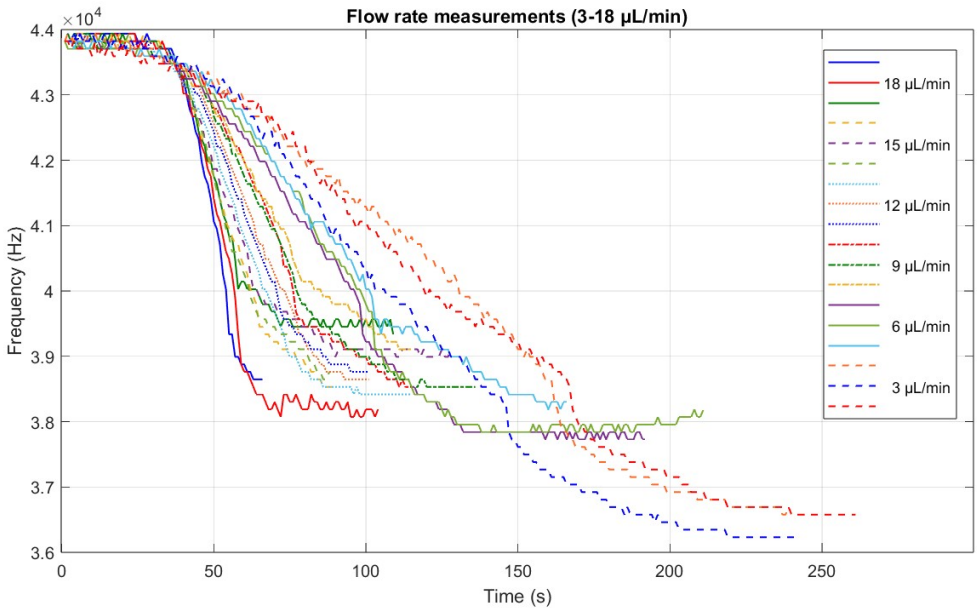

Figure 5.22: In triplo flow rate measurements with the rectangular reservoir from 3-18 μL/min. The data is normalised towards the average starting frequency for clarity.

During the experiments, it was found that trapped air between the print and bi-adhesive tape could act as a crevice for fluid to leak into. This can introduce an error in the measurements. It can occur at the corner of the print and the sensor. Most of the trapped air can be removed by pressing the print firmly. Initially, the prints were used once, flushed with water and then left to dry, alternating different prints. At a later stage, the print was reused. Leakage might also be prevented and results improved with another seal or material. For prolonged measurements, heating was noticed of the syringe pump, which should be prevented.

Our bi-adhesive was originally intended for hair pieces, like toupées and wigs. However, we did not look into other adhesives. The same goes for the microfluidic substrate. It is recommended to investigate other materials, like PET, PDMS or other resins. Increasing the hydrophilicity of the adhesive may already improve the consistency of the refilling behaviour. The surfaces of these materials can also be tailored to improve wettability. Only a Vaseline barrier was tested to try and dissuade sideflow. Yet, a hydrophilic center will improve consistency of the refills more. Hydrophilicity is better for reproducibility in general. In primary filling, the sweat still has to overcome the hydrodynamic resistance in the dry channel. This resistance will be lower for a hydrophilic channel. This would also lessen the discrepancy between dry and wet channel filling.

The data acquisition can also be improved. The built-in peak detection is convenient, because it directly extracts the peak data. However, this lacks sampling speed and precision. It is better to extract all the data from the frequency sweep instead of just the peak values. A separate peak detection algorithm can then provide better defined shift curves, especially when the shift is small. Moreover, fitting the Butterworth-von-Dyke model can also improve the accuracy of the resonance peak detection.

5.4 Wearable development: collection area

Now we are capable of obtaining a good measurement signal, we can proceed to develop a means to transport sweat from the sweat glands to the sensing area. The first part of the sweat journey has already been taken care of. Sweat is transported to the skin's surface after being produced, so it is our goal to collect this within the shortest possible time. This can be achieved by minimising the amount of dead volume in the design, whilst covering the largest amount of sweat glands. The sweat glands are stimulated through pilocarpine iontophoresis.

Sweat collection systems have already been well developed [2, 37]. Most consist of a microfluidic structure expressing higher hydrophilicity. Moreover, some are aided by a hydrophilic filler or a steep surface tension gradient. Our substrate is not optimised for sweat collection due to the low hydrophilicity of the resin. The capillary effect was little, although present from visual inspection (Appendix Figure D2). The collection area developed here serves as a means to facilitate the on-body assessment of the new sensing modality.

In addition, the collector was specifically made for our male test subject and our iontophoresis system, developed by T. Bakker in 2019 [118]. The electrodes in this set-up are compatible with circular Pilogel disks, but the current Pilogel Disks (ELITechGroup) are elliptical. This limits the active area considerably in size, because the disk must be halved in order to fit. The active area was around 3 cm^2, which corresponds to 104 sweat glands[15]. Given that the iontophoretic output upon pilocarpine is expected to be 10 nL/min on average for men [20], flow rates of around 3 μL/min are expected. Iontophoresis was performed according to the protocol found in Appendix D.3.

5.4.1 Basis design

The membrane design was adapted for a wearable configuration by creating a collector with a 1 cm radius and 2 mm height. The 2 mm height accommodates potential skin curvature, while the sensing structure sits atop the collector to minimize space. A small gap was maintained between the membrane and the collector (Figure 5.23). A 0.5 mm-wide collection channel at the edge of the collector prevents long filling times, transitioning to 1 mm width after the sensing area to test wicking. The membrane radius remains 7.25 mm, consistent with prior designs.

A T-junction design was proposed for compatibility with both the syringe pump and skin application. The T-junction uses a capillary stop valves to promote unidirectional flow toward the sensing area (Figure 5.24). However, this design failed due to bursting at the T-junction when Laplace pressure in the channel exceeded that of the stop valve. Despite rounding the edges to reduce Laplace pressures, the issue persisted. Early channel widening to 1 mm could alleviate the problem, but the hybrid concept was abandoned to focus on the sweat collector.

The basic collector design, 2 mm high, ensured sweat glands remained unblocked. However, at the average male iontophoretic sweat rate, filling would take three hours—far exceeding the one-hour stimulation duration. To reduce filling times, four funnel-based collector concepts were developed, with a sloped design directing sweat toward the inlet (Figure 5.25). The base design and two variations are depicted in Figure 5.26. The fourth variation builds on the funnel design.

1. **The funnel**: At the base, de design consists of a funnel towards the collection channel. The maximum depth at that point is 0.75 mm. It is expected that a part of the

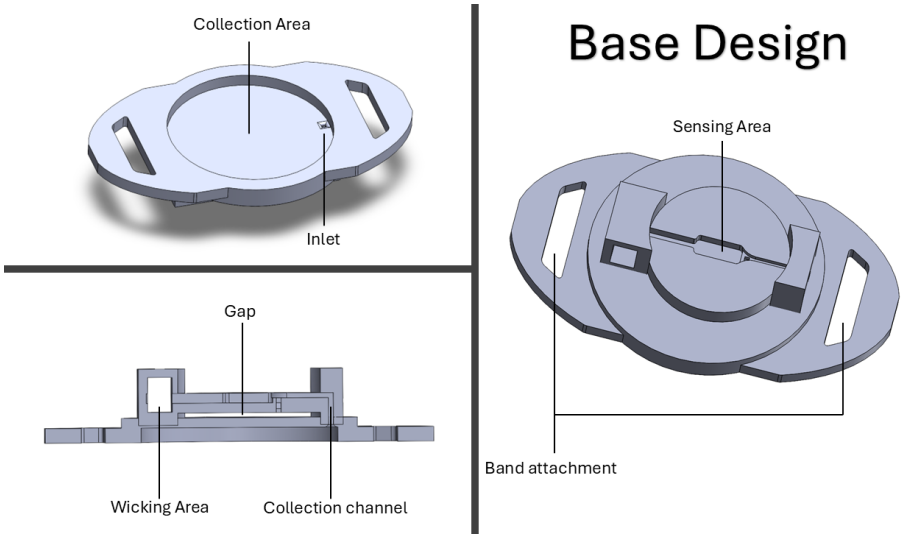

Figure 5.23: Schematic drawing of the wearable base design. A gap between the collector and membrane is maintained to reduce damping.

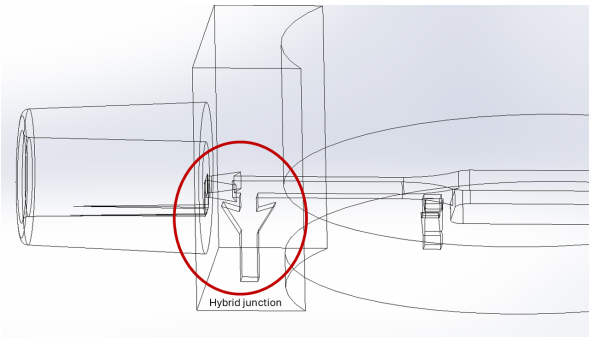

Figure 5.24: Hybrid junction design for compatibility with a syringe pump and on-body sweat measurement.

sweat glands can be occluded, because of the shallow depth. The collection channel is positioned near the edge, which also prevents blockage of the inlet.

2. **Lines**: This design has structural lines to prevent the skin to deform and occlude sweat glands. In addition, the corners of the lines can act as a guide. This promotes corner flow, though this effect is not significant for contact angles above 30° [38].

3. **Hexagons**: A hexagon infill is used to reduce the volume of the collector and can act as a capillary guide [38]. In addition, the hexagons can provide structural support.

4. **Porous medium**: By placing a porous medium in the funneled collector, the filling time can be reduced. The Cutisoft woven compress was used as a hydrophilic porous medium.

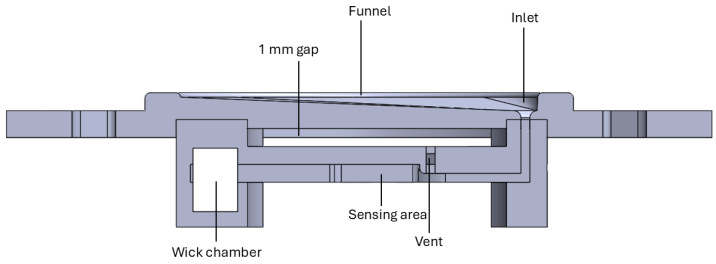

Figure 5.25: Cross-section of funnel design, illustrating the slanted profile towards the inlet.

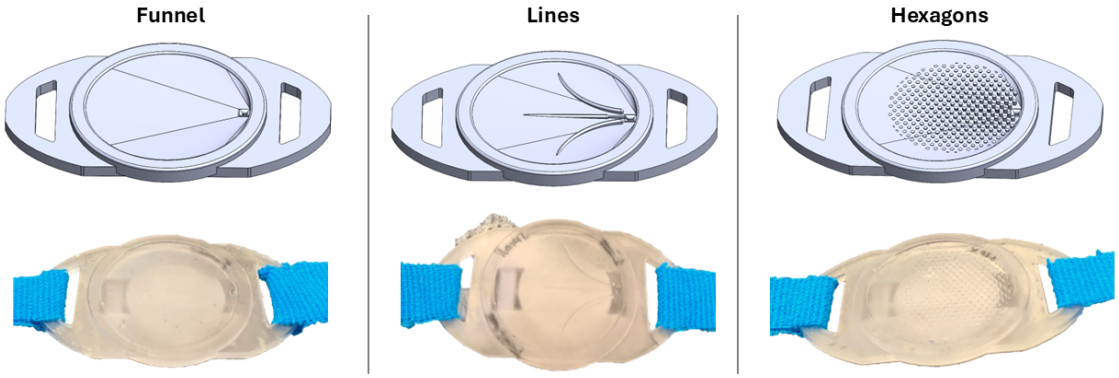

Figure 5.26: The digital drawing and SLA printed collectors

Design	Time (min:sec)
Lines	5:40
Funnel	6:20
Hexagons	11
Porous Medium	22:30

Table 5.2: Filling times for the different collection concepts.

5.4.2 Results

The quickest filling time was achieved by the lines concept, closely followed by the simple funnel design. The gain from using structural lines is marginal. The funnel occludes more

sweat glands than the lines design, but there is also less volume to fill. The lines design limits skin deformation, preventing the blockage of sweat pores, but also increases the volume of the device. The hexagon design took twice as long as the lines design to fill, likely due to direct skin contact covering sweat glands. The porous medium performed the worst, requiring the compress to fully saturate before filling could begin. This design was four times slower than the lines concept. The results are summarised in Table 5.2. In the current designs, determining the number of blocked sweat pores remains challenging. This is problematic, because the sweat rate per gland should be retrievable from the flow rate. Additional variables influencing the filling rates include the time of day hydration levels, prior physical activity, and attachment tightness of the collector. These factors were controlled by measuring subjects around noon, ensuring hydration, and avoiding intensive activity. We assumed that the sweat rate from the left and right under arm is similar. However, literature suggests they are slightly asymmetrical [23].

The goal of this section was to create a practical sweat collector to transport sweat to the ultrasonic sensor. All collector designs achieved sweat filling. The funnel and lines designs demonstrated filling times well within the iontophoretic window, making them suitable for wearable flow rate testing. The lines design was selected for its faster filling and better reproducibility under varying attachment forces, as its structure limits skin deformation. Physics simulations and further measurements are recommended to refine these designs.

Chapter 6

Characterisation and analysis algorithm

6.1 Development of characterisation and flow rate estimation algorithm

From Figure 5.22, it is possible to already distinguish higher- and lower-order flow rates based on slope and measurement time. It shows potential for using a piezoelectric transducer for microfluidic flow rate measurements. But, to further substantiate this, the visual distinction must be quantified to accurately determine the sweat rate. It raises two questions. First, how do we recognise the start of a measurement? Different flow rates will create different times when the reservoir start filling, so it must be identified when the sensor starts being responsive to the fluid. Second, how do we quantify the filling once we start the measurement? This section introduces two algorithms to address these questions. The first characterises the frequency shift in relation to sweat volume within the reservoir. The second estimates the flow rate based on the measurement data.

6.1.1 Characterisation algorithm

To identify the start of filling for characterisation, three methods can be employed. The first is manual inspection, which involves visually identifying the points where the frequency shift begins and ends. Although this approach is straightforward, it is time-consuming and inefficient. Another method is threshold-based windowing, where a threshold frequency is used to automatically isolate the data. This technique is more effective in the volume domain, as the curves align more consistently in Figure 6.1. However, finding the optimal threshold requires trial and error and may result in inconsistent cutoffs in the time domain. A third approach involves using characteristic parameters of the curve to determine the start of filling. This method is both precise and efficient, making it a preferred choice. This will be further elaborated upon in this section.

Recognising filling

The filling curve mostly resembles a sigmoid, containing two bending points and an inflection point in between. By finding the bending points of the curve, the part corresponding to

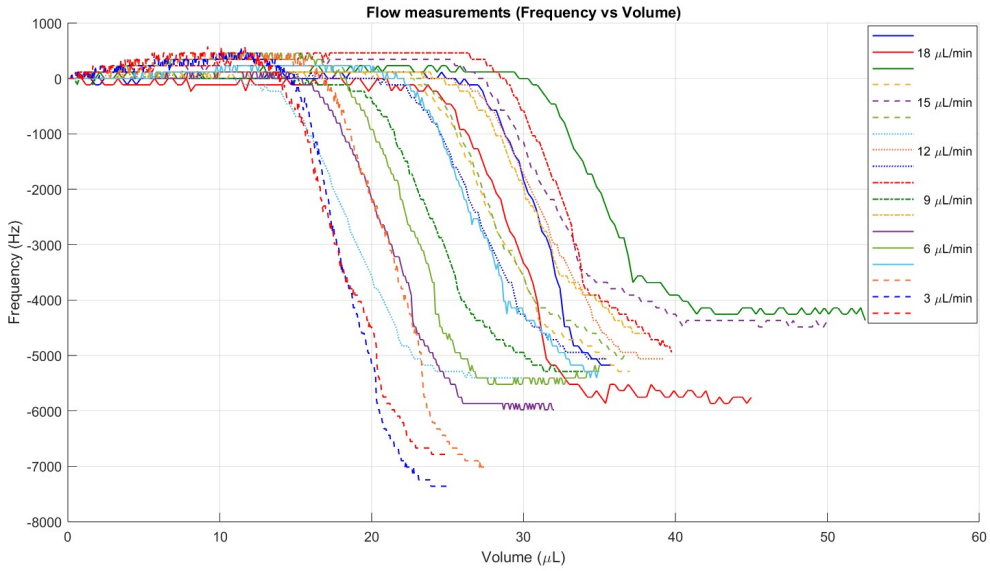

Figure 6.1: Frequency vs volume plot of in triplo flow rate measurements with the rectangular reservoir from 3-18 μL/min. The volume is determined by multiplying the measurement time with the known flow rate. The data is normalised towards the average starting frequency for clarity.

sensor response can be isolated. The bending points are best accessed through the second order derivatives where they constitute either a positive or negative peak. The bending points are found automatically by an algorithm. It first smooths the curve using locally estimated scatterplot smoothing, of which the effects are plotted in Appendix Figure D3. Then, the first and second derivatives are taken to find both the inflection point and the bending points.

One challenge in obtaining experimental data is that differentiation amplifies noise, making the information difficult to interpret. To address this, a second smoothing step is applied before calculating the second derivative. Figure 6.2 shows an example of the algorithm's output. Although the first bending point is identified with high accuracy, the inflection point and second bending point are less precise. Ideally, in a perfect sigmoid curve, the bending points would be symmetrically positioned. However, in practice, the second bending point is often located closer to the inflection point. This discrepancy likely originates from experimental variation at the curve's end rather than algorithm misclassification.

The algorithm determines the first bending point by searching near the inflection point. The second bending point is located within the range defined by the first bending point and the inflection point, ensuring that it remains within a single filling cycle. Although this method has some inaccuracies, it effectively defines boundary values for characterisation, as will be demonstrated in the following section.

Quantifying filling

At first glance, it seems attractive to relate the complete shape of the curve to the flow rate. However, in practise, the measurements will not exhibit a perfect sigmoid curve all the way through. Rather, the flow rate will vary during the measurements and the algorithm should

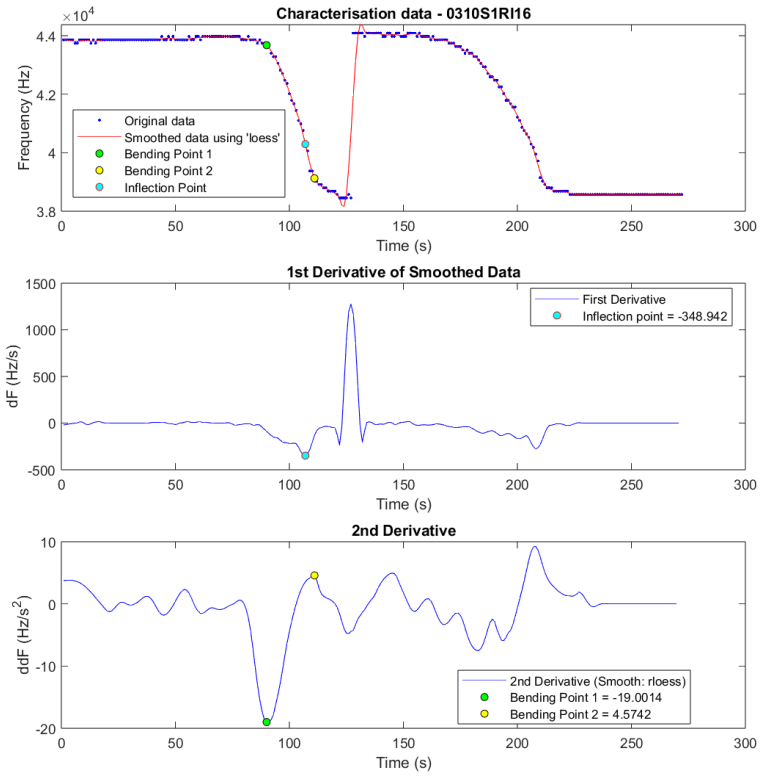

Figure 6.2: Example output of the bending point algorithm.

take this into account. In other words, the characterisation method should be independent of the set flow rates. Variations in sweat rate can then be monitored as the reservoir fills, and not only once it is full. This can be achieved by relating the frequency shift over the amount of volume in the reservoir, retrieving the volume by multiplying the flow rate with time. In Figure 6.1, a relatively constant slope can be observed for each of the measurements. By determining a slope, linearity is assumed, and this is also a prerequisite if the goal is to perform a real-time measurement. To retrieve our target constant, the slope F/V, three methods were assessed: a manual sigmoid fit, a manual linear fit, and an automatic method using the characteristic points in the curve.

Both the sigmoid and linear fit required manual input in order to optimise the fit. The linear fit is straightforward, outputting the constant F/V directly. With the average F/V of the dataset, the flow rates are recalculated. In doing so, the estimated values can be compared with the set values of the syringe pump, as can be seen in Figure 6.3. The root mean squared error (RMSE) is used as an error metric, because it is in the same units as the measurement. The data shows the error caused solely by averaging, because the window is kept exactly the same for the data. For the sigmoid fit, visible in Appendix Figure D4, the logistic sigmoid equation was used: a/(1+exp(-b*(x-c))). a determines the starting asymptote, b determines the steepness and c the position of the midpoint. To find the slope at the inflection points, the parameters are multiplied and divised by 4: ab/4. The sigmoid fit showcases the largest

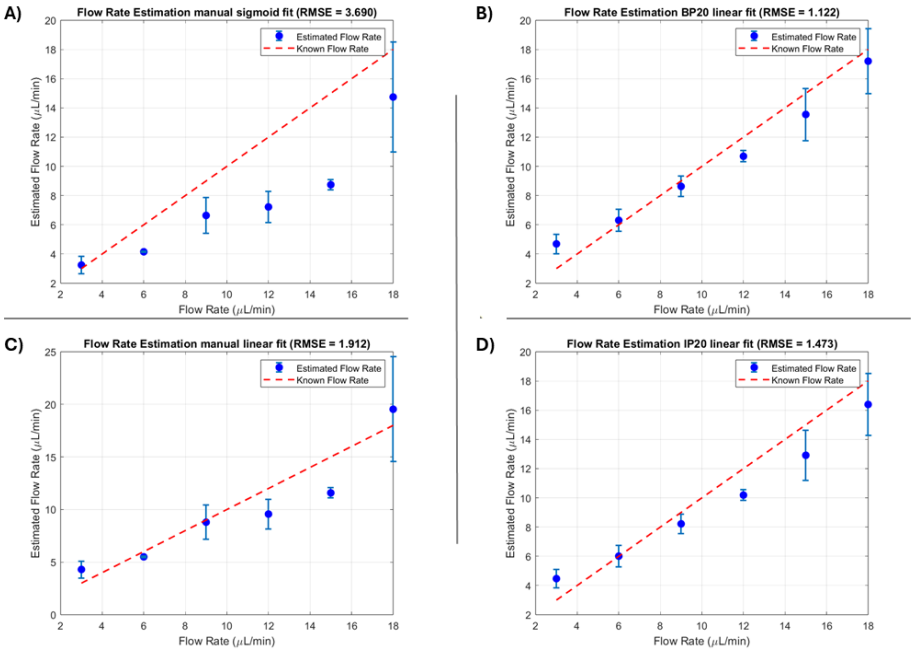

Figure 6.3: Assessment of the flow rate characterisation approaches based on A) a sigmoid fit, B) a linear fit and an automatic linear fitting method with 0.2 rloess smoothing based on C) bending point to bending point windowing and D) bending point to inflection point windowing.

error, as can be seen in Figure 6.3.

The final method was based on the bending point algorithm. Two variants were tested by taking either the difference or performing a linear fit between the first bending point and either the inflection point (BPIP-approach) or the second bending point (BPBP-approach). The linear fit BPIP-approach is more precise, as the linearity is better approximated with smaller ranges. The second approach takes into account a wider range of data. This is a less specific region of the curve, but may create a F/V constant which is applicable over a wider range. Other results can be found in Appendix Figure reffig:overfitting.

Evaluation

Based on the results in Figure 6.3, it is evident that the automatic approach is the best method based on this dataset. Generally, the lower flow rates are overestimated in each case and higher variance occurs at the higher flow rates. It was expected that the absolute frequency shift would be constant irrespective of flow rate, as discussed earlier.

Yet, a higher frequency shift originates from lower flow rates specifically. At higher flow rates, a greater variance exists, which could be attributed to higher pressures in the system. The pressures could cause leakage at the interface between the microfluidic structure and the adhesive. Nevertheless, the variance is also a product of the characterisation method used. The sigmoid fit has the smallest variance, but underestimates the flow rate, because it is based on the steepest point of the curve.

The linear and bending point characterisation represent the slope over a wider region.

However, there is also greater variance in this region. On one hand, this is due to experimental factors, such as the degree of adhesion or variable behaviour of the wick. On the other hand, the manual and automatic windowing cannot ensure that the curve is windowed at exactly the same point in the curve. However, through an algorithm, it is less prone to human bias.

Still, the way of evaluation of the algorithm is prone to overfitting with the different degrees of smoothing and reference points used. A shortcoming is that the errors in averaging are essentially evaluated using the same window and not the consistency of the automatic windowing. Although it provides some insight in the performance, a better method is to validate it on a new dataset. We proceeded with a F/V constant of -614.26 Hz/μL from the BPBP-approach with 20% smoothing (BP20) to incorporate in a flow rate estimation algorithm to assess the feasibility of the flow rate sensor.

6.1.2 Flow rate estimation algorithm

Recognising filling real-time

The above algorithm serves as both a means of quantifying filling and a method for characterizing the sensor. With the constraints of a real-time measurement, a flow rate estimation algorithm was developed. Real-time filling recognition cannot rely on bending points and should not rely on manual inspection. A threshold frequency approach is also problematic because the starting resonance frequency varies between measurements. To address this, relative negative frequency shift thresholding —sufficiently large to distinguish from noise— is used to identify the start of filling. Similarly, the end of filling is detected using a relative positive threshold. A small degree of smoothing is used to compensate for the sampling issue of the analyser.

While this method is compatible with real-time measurements, it is less consistent and more sensitive to noise than the bending point algorithm. Finetuning is sporadically required to account for early perturbations in the data, which are also unavoidable in wearable applications. One potential improvement is to tailor the threshold to specific flow rates, as noise sensitivity depends on the chosen threshold. This adjustment can also consider factors like the type of sweat induction or expected sweat rates (e.g., based on gender), allowing for narrower flow rate ranges.

Absolute thresholding was not developed but remains a viable option. To reduce noise interference, a condition could be added requiring a series of consecutive points below the threshold to confirm filling recognition. Further development in these areas is necessary to enhance reliability in wearable applications.

Measurement interval for averaging

After finding the starting time, a measurement interval is used to average over the real-time data. The interval was set to 60 seconds, because typically, sweat changes occur on the order of minutes, as discussed earlier. If this interval was not attainable, the length of the window is taken as interval. In Figure 6.4, some exemplary results are illustrated using the result from the BP20-approach. Contrary to the expectations from Figure 6.3, the lower flow rates are actually quite accurately determined in two cases, while the accuracy drops-off towards higher flow rates. This effect is caused by the relative scale of the interval against the measurement time, as seen in Figure 6.5. If the interval is significantly smaller than the measurement time, more interval segments are taken within the approximate linear region of the measurement.

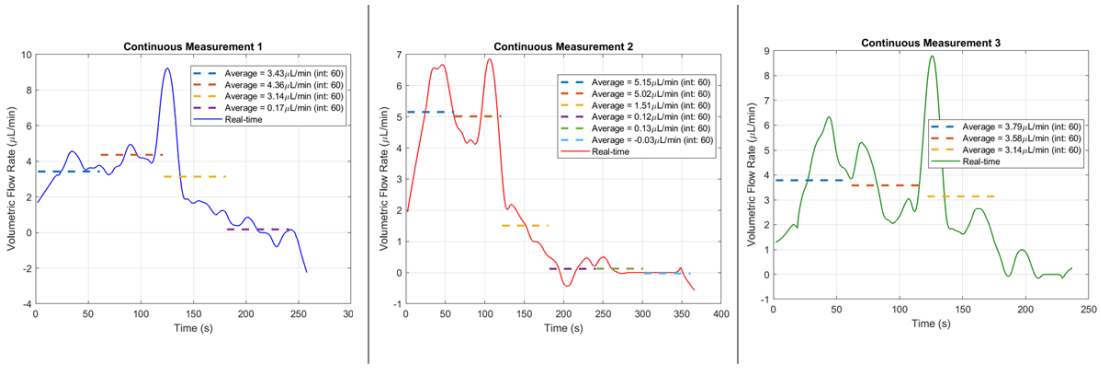

Figure 6.4: Flow rate estimation for 3 μL/min.

For a relatively large interval, even constituting the complete length of the window, the region become less linear. This leads to an underestimation of the flow rate. With smaller measurement ranges the interval can be optimised to suit all data. Nonetheless, the results at the lower flow rates are promising. In general, the measurements of 3 and 6 μL/min show good results, with two out of three measurements generating an accurate estimation of the flow rate. At the mid flow rates, from 9-12 μL/min, the flow rates are less accurate due to the interval to length of measurement ratio. If this is changed, the accuracy can be improved. The same holds for the higher flow rates, although more variation in estimated flow rates can be expected based on the variance in the data and increased curve from the sigmoid shape. The results for the whole data set can be found in Appendix Figure D6 and D7.

Discussion

A flow rate estimation algorithm was developed in this section, using an algorithm which takes the constraints of real-time measurements into account. It is advisable to characterise the device response for each configuration with a new print and tape. It is the latter that may cause unpredictable effects, because they are manually cut. Moreover, it is recommended that more independent measurements are performed for introducing statistical analyses to confidently fit data and exclude outliers. This will further improve the scientific rigour and further establish the method. Additionally, the interval effect is expected to remain a limitation of this technique. However, the effects can be mitigated by developing a smart algorithm to adjust the interval according to the curve.

The sigmoid curve profile could also be compensated for in the future. One can finetune the geometry for instance. Naturally, the sigmoid shape is also the reason why the slope at the inflection point was unsuccessful, as the slope is the highest at the inflection point, leading to an underestimation of the flow rate anywhere else. However, for the flow rates around and below 3 μL/min, the sigmoid fit might be a feasible method. Here, the degree of inflection is small for the lower flow rates. This means that the slope at the inflection point has greater resemblance to the surrounding region of the curve.

Most importantly, it must be mentioned that the flow rate estimation algorithm was tested on the same dataset as the characterisation algorithm. The issue in doing so, is that the found constant from the characterisation holds semblance to the data for which the flow rate is now

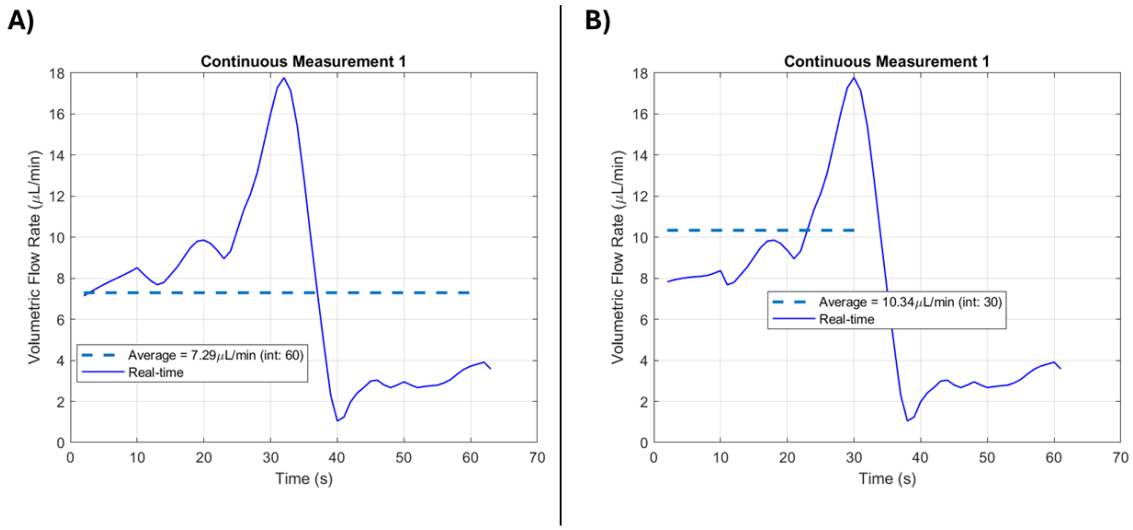

Figure 6.5: Flow rate estimation for 9 μL/min at different intervals (60 and 30).

estimated. This is a shortcoming, but insights are still provided, because of the contrasting windowing approaches of the two methods.

Chapter 7

Wearable Testing of Prototype

7.1 Wearable Testing

This section constitutes the final experimental result of the prototype in this thesis. It takes shape as an on-body test of ultrasonic piezoelectric sensor for flow rate measurements. This paragraph will begin with an elaboration on the set-up and protocol used. This is followed by insights from preliminary testing, which was done in parallel to the testing of the sweat collectors. With these insights, new problems that arose were tackled. Finally, a true sweat measurement is presented, which can be considered the final milestone in this project.

7.1.1 Methods

For these measurements, the same iontophoresis protocol is applied, which can be found in Appendix D.3. After iontophoresis, a small amount of dye is placed on the stimulated skin region. The piezoelectric sensor is covered by the bi-adhesive and firmly pressed to the 3D-printed collector. The collector is attached to the volar part of the underarm with sports tape. The impedance measurement is started once filling takes place. The measurement is stopped when either a steady state is reached in sensor response (after filling), or when filling is unlikely to happen. Because real sweat is tested, measures are taken to ensure safety. The sensor is electrically insulated from the subject and galvanic isolation is achieved by the placement of transformer (1:1) between the impedance analyser and the sensor.

After the measurement, the frequency curve is analyzed and converted to flow rate using an algorithm described in the next chapter. The estimated flow rate can be compared to the flow rate is validated with either the gravimetric or colorimetric method.

Gravimetric testing is done by measuring the weight of the flow rate sensor prototype, before and after the measurement. The difference between the weights will constitute the mass of sweat that was produced during the time of testing. For the colorimetric method, the volume of the sweat in the microfluidic structure must be known. If the time of entry to and exit of the microfluidic structure are known, the average sweat rate can also be determined.

7.1.2 Final iterations

During testing of the sweat collectors, sweat failed to reach the outlet due to leakage occurring at the corner where the wick was wedged between the sensor and the print, as shown in Figure 7.1. Once the sweat contacted the bi-adhesive tape, it spread across the sensor, impairing

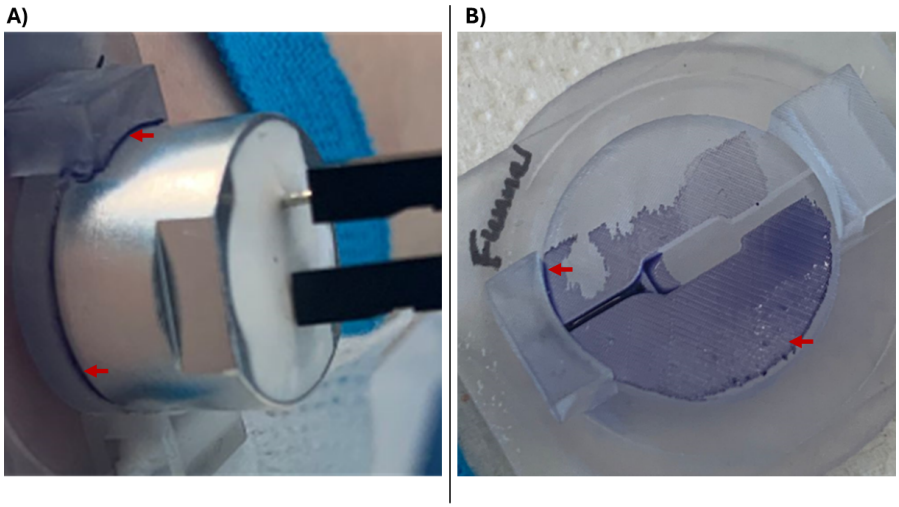

Figure 7.1: Leakage issues with sweat depicted with red arrows. A) Leakage visible during a measurement. B) Inspecting filling and leakage after the measurement. Note that upon removal, sweat disperses into the adhesive due to underpressure.

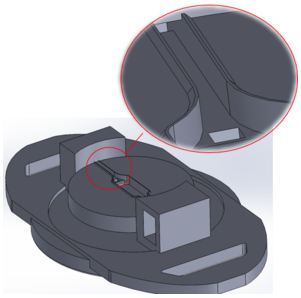

Figure 7.2: Extruded channel contours of 0.1 mm height to prevent leakage.

proper visualization of the channels. After testing, the sensors were removed for inspection, revealing through ink deposition that sweat only filled about a quarter of the sensing area.

The leakage can be caused by the loose connection of the sensor with the adhesive. Through motion, the sensor cannot be as firmly attached as in the static tests. Another contributing factor could be the size of the membrane. Initially increased from 7 mm to 7.25 mm to better match the sensor, the larger radius may have been too wide for effective containment of sweat. Additionally, the design contains a transition from the 0.5x0.5 mm channel to the reservoir, which is 2.2x1mm. This change in geometry might be too sudden, increasing the Laplace pressure and redirecting sweat into the crevice rather than along the intended path.

The prototype is redesigned to better contain the sweat in the channels. This is firstly done by decreasing the radius from 7.25 mm to 7.15 mm. Small extruded walls (0.1 mm height) were added to the channel contours, as illustrated in Figure 7.2, to guide the sweat flow more effectively. Lastly, allowing the adhesive tape to sit longer before testing improved the bond and reduced the likelihood of leakage. These adjustments aim to ensure sweat is better retained in the channels and can reach the outlet during testing.

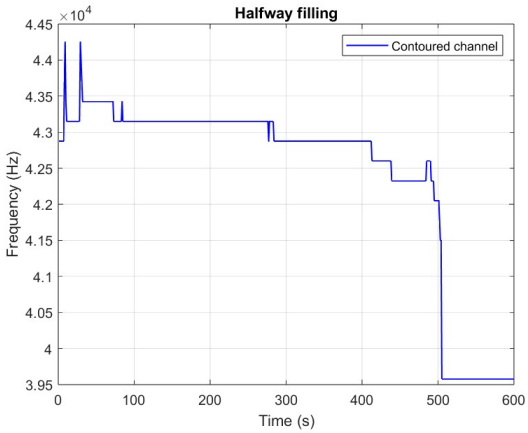

Figure 7.3: Sensor output for halfway filling of the sensing area.

7.1.3 Results

First, the design is tested where only the radius was changed. This results in leakage as can be seen by the stains in Figure 7.4. Again, sweat does not reach the end of the channel. The design with extruded channel walls showed better results. A small shift is observed, when inspecting the data in Figure 7.3, and upon visual inspection of the dried channel in Figure 7.4, it seems the reservoir was halfway filled. However, this is still not the desired result.

Now, the tape is attached to the sensor and print to be set over night. Both the designs are tested in order to pinpoint which adaptation is critical. The results are depicted in Figure 7.5. The design without extruded contours achieves reseroir filling, but no wicking due to leakage in the final part of the channel, as can be seen in Figure 7.4. The extruded contour design did provide a clean measurement, and is depicted in Figure 7.2. The channel filling reached the wick and was partially absorbed. The characteristic sigmoid shape is still represented, although the flow rate is not expected to remain constant. Rather, it decays over time. Due to motion, prevalent at the end of measurement to inspect potential leakage, the signal is distorted. The main cause was twisting of the underarms deforming the skin. This altered the volume of the collection well and advanced or retracted volume in the channels.

Using the flow rate estimation algorithm, the frequency shift is translated to volume for both measurements in Figure 7.6 by a constant F/V=-614.26 Hz/μL. The retrieved volumes are close to the actual reservoir volume of 11 μL. Over the full interval, the flow rate of the first and second measurement using the ultrasonic sensor was found to be 1.38 μL/min and 1.56 μL/min respectively. Figure 7.6 shows the real-time data and the average over the full data.

Gravimetric measurement succeeded only for the second test due to experimental error, yielding a flow rate of 0.98 μL/min. A colorimetric flow rate estimation was also performed, which aligns more closely with the ultrasonic measurements as it spans a similar timescale. With a total microfluidic volume of 17.3 μL and known membrane entry/exit times, flow rates were estimated at 1.31 μL/min and 1.22 μL/min for the two tests.

If the averaging interval is changed to 60 seconds, as if the sensor would provide a read-out every minute, it would output the results in Figure 7.7. The trend of the sweat rate is then roughly in accordance with the expected decay of sweat rate after pilocarpine iontophoresis. However, there is quite some fluctuations in the data, leading to negative flow rate measure-

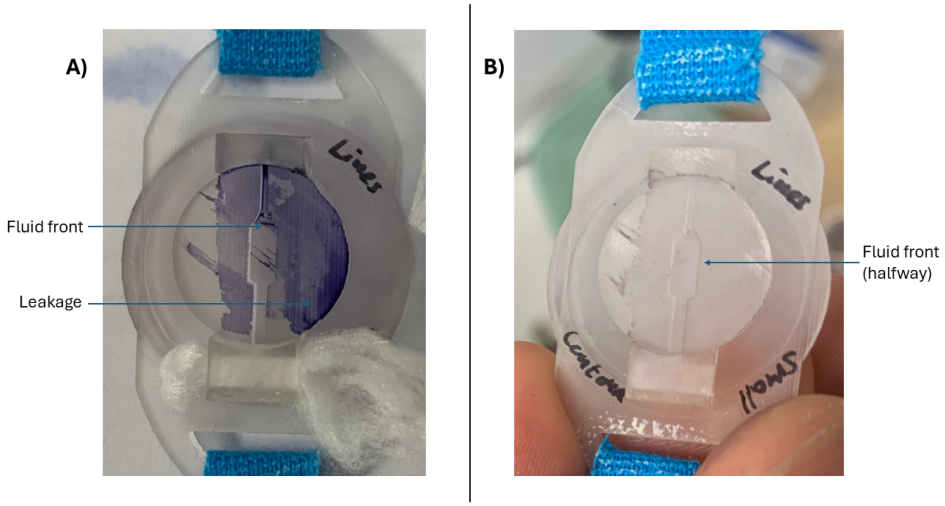

Figure 7.4: Estimation of channel filling degree through colourant stains after adhesive removal. A) The reservoir was not reached for the flat channel due to leakage. B) This image shows the dried dye front in the reservoir for the extruded wall contours.

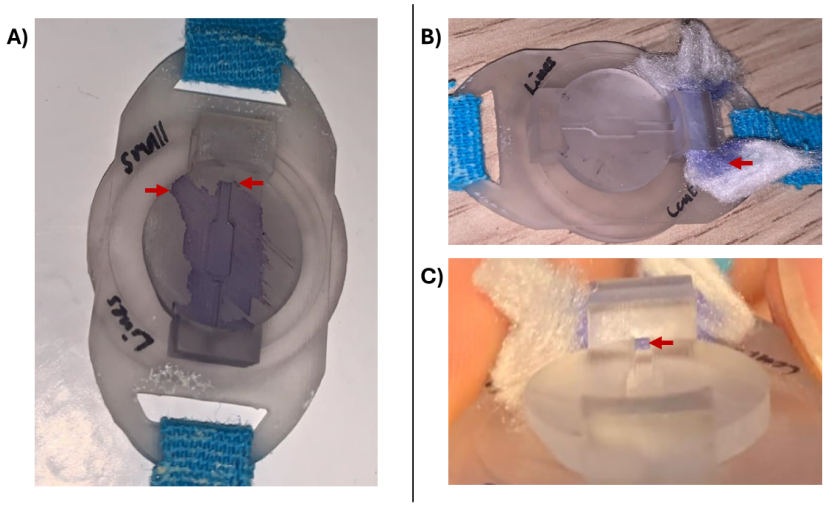

Figure 7.5: Sensor stains after complete filling of the reservoir after the adhesive was set overnight. A) Red arrows denote the sweat in the flat channel design nearly reaching the end of the channel with leakage. B) Extruded contours design where the wick is stained with sweat. The channel contents are fully wicked. C) Confirmation of sweat reaching the end of the channel blue stains at the outlet.

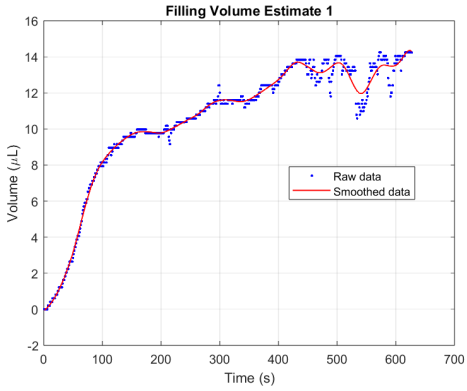

(a) Volume estimation for measurement 1 (flat channel)

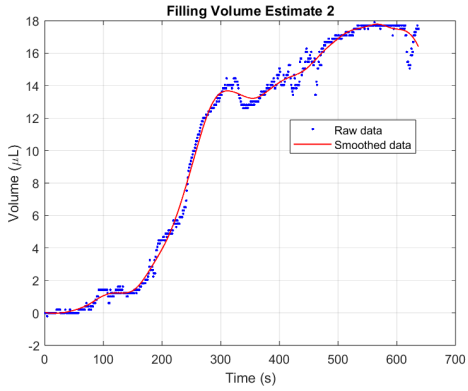

(b) Volume estimation for measurement 2 (walled channel)

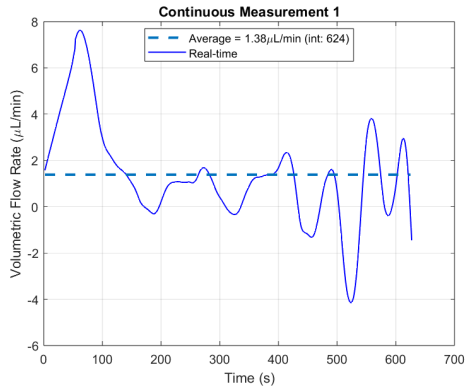

(c) Flow rate estimation for measurement 1 (flat channel)

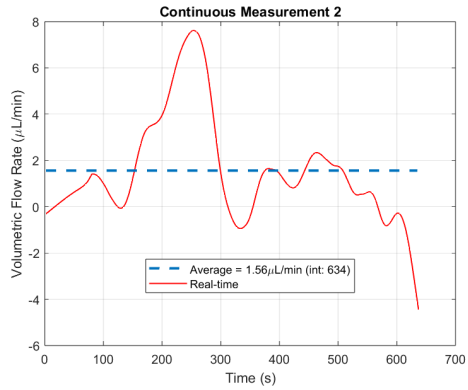

(d) Flow rate estimation for measurement 2 (walled channel)

Figure 7.6: Wearable sweat test results. Subfigures show (a) and (b) volume estimation for flat and walled channels, and (c) and (d) flow rate estimation for measurements 1 and 2.

ments. It may be that this is a motion artefact, or the result of noise. Unfortunately, this could not be further investigated at this time.

7.1.4 Discussion

The results show that the right order of the flow rate is achieved. It shows a decaying trend as is expected from pilocarpine iontophoresis [71]. Starting at a flow rate of around 4-5 μL/min and then quickly reducing to below 1 μL/min. While this is promising, the presence of a negative flow rate shows that there is still undesired behaviour. This can be physical due to motion of the subject. As the underarm is twisted, pressures are generated because the rigid collector does not deform, while the skin does. A flexible collector would be able to deform with the skin and perhaps reduce this effect.

An important note is that the gravimetric method and the ultrasonic sensing method are not performed over the same period. The latter measured during 10 minutes, while the gravimetric measurement were performed with around 40 minutes in between. In addition,

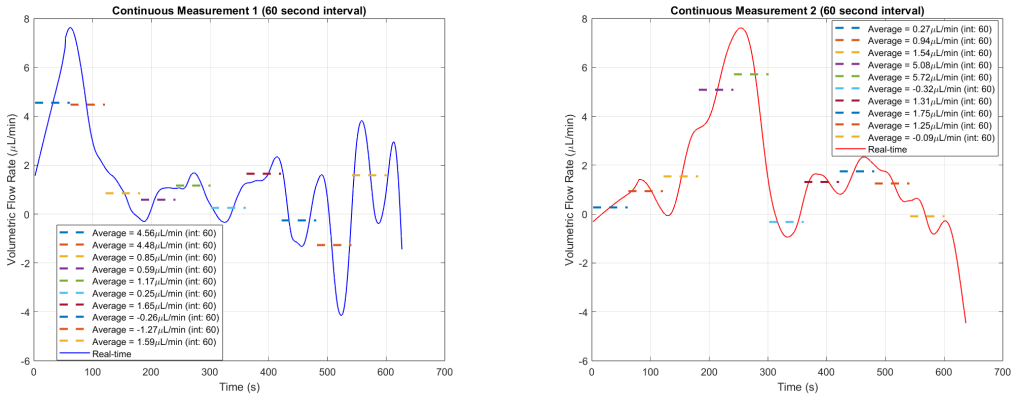

(a) Flow rate estimation every 60 seconds for measurement 1

(b) Flow rate estimation every 60 seconds for measurement 2

Figure 7.7: Treating the data like a real-time measurement.

sweat could evaporate at the end of the channel. Due to evaporation, it is most likely that the flow rate is underestimated.

The colorimetric method was more reliable. The measurements were started when the transport channel was filled and ended when the wick was reached or nearly reached. The colorimetric method shows near accordance with the found values from the prototype. The found flow rates are below the flow rate ranges on which the estimation algorithm was based (3-18 μL). In principle, however, the estimation showed approximate flow-independency by normalising to volume instead of flow rate, as visible in Figure 6.1. Nevertheless, a broader characterisation range covering these flow rates would be more comprehensive. Furthermore, the wicking concept did not empty the channel in this test, when the data is examined. Yet, the collection channel seemed to be wicked dry after the measurement, see Figure 7.4. A positive remark is that the stop valve in the air vent never leaked in wearable testing. This is promising for further optimising the wicking behaviour.

Using the our new flow rate sensing modality and prototype, including a collector, we managed to achieve a flow rate that is close to the flow rate using a colorimetric method. However, this was based on only 2 tests, not holding statistical significance. Accuracy is expected to improve with more measurement and a comprehensive validation of the characterisation algorithm. Additionally, true real-time measurements at 1 min. intervals are still variable and not validated.

Chapter 8

Conclusion

This thesis explores the development of a novel platform for reliable sweat rate measurements, which are essential for enhancing the potential of sweat analysis. Accurate sweat rate measurement allows for compensation of sweat rate effects on the sweat matrix and has significant clinical relevance. The initial sections cover the physiology of sweat to highlight the importance of sweat rate, followed by a review of existing wearable flow rate sensing methods.

The focus of this research was on designing a microfluidic flow rate sensor accompanied by a sweat collector. Three concepts were evaluated based on requirements and criteria such as real-time measurement capability, reliability in clinical settings, and performance under artificial sweat stimulation. A resonance-based weighting concept showed the most promise and was further developed.

A prototype was constructed using a piezoelectric sensor, a 3D-printed microfluidic structure and double-sided adhesive. Various sensors were tested beforehand. The most effective sensor underwent further characterisation. Modifications to the 3D-printed structure optimised the shape and size of the sensing area to enhance sensor performance. As a reservoir at the centre of the piezoelectric sensor fills, a frequency shift of several kHz is observed. This behaviour was linearly related to the flow rate after characterisation with a syringe pump, averaging over a set interval. A wick was added at the end of the microfluidic structure to facilitate sample renewal. By the addition of a vent upstream, the complete reservoir could be drained. Leakage was prevented by using a stop valve. The system was completed by designing a sweat collector to accommodate on-body sweat rate measurements.

To validate the system, on-body sweat rate measurements were conducted using pilocarpine iontophoresis. The data was analysed and compared with the actual flow rate, for which an established reference method was used. The sensor retrieved flow rates of 1.38 and 1.56 μL/min. This was in good agreement with the reference method: 1.31 and 1.22 μL/min, respectively.

In conclusion, this thesis contributes to the growing field of wearable sensing technologies by introducing a novel piezoelectric-based flow rate sensor for sweat analysis, demonstrating its feasibility and potential for further development in future applications.

Chapter 9

Future Outlook

9.1 Further development

The next steps in the development of this prototype is to improve the characterisation by increasing the testing volume. Statistical analysis will provide a better indication of performance than in duplo tests and reduce chances of overfitting. Moreover, the sensitivity to motion, pressure loading and temperature must be investigated. Many piezoelectric materials are also pyroelectric, meaning that they can produce an electric field due to temperature changes [89]. It was not investigated how temperature differences and fluctuations influence the magnitude of the resonance shift in this particular sensor. The linear characterisation method and its flow rate sensing performance are a step in the right direction. Exploring geometric compensations for the sigmoid curve could provide further optimisation. For the prototype, it is also suggested to investigate more hydrophilic options for the adhesive to improve reusability. The next steps in the development of this sensing modality is to investigate other resonators as well.

Admittedly, because our study focused on the feasibility, most of the tests served a goal of reaching a wearable measurement. The tests were therefore not comprehensively performed and many of the tests could be expanded upon. The characterisation was performed on one dataset, and the wearable test was not performed with the same device on the same day. Therefore, a critical note may be placed at the measured flow rates.

AT cut quartz, for instance, can still provide accurate measurement under temperature changes (10-50 C°) [91] and is the golden standard for microgravimetric measurements [95]. SAW devices can also be considered [78]. Fundamentally, we could not attribute the shift to only mass or only viscosity effects. Channel height was critical in maximising the frequency shift, but also the geometry was decisive. Different contact areas created an approximately equal shift for geometries in the plane with the surface of the sensor. However, when the membrane thickness of the print is varied, this can be detrimental to the shift.

Rather than measuring thin-film masses, our technique focuses on analysing the gradual replacement of air with sweat. Future research should involve a detailed examination of the resonator-fluid interaction, which can be investigated using physics simulation software or advanced analysis [101, 119, 103]. This approach allows for a deeper understanding of the piezoelectric response to microfluidically contained sweat.

Aside from this, a wearable circuit should be development to drive the resonator and perform impedimetric measurements to detect the frequency shifts real-time. However, a

wireless read-out is also achievable as the ultrasonic waves propagate through air. This saves space and would be a unique feature of this measuring modality.

9.1.1 Resonance weighing as a flow rate sensing modality

Magnetoelastic resonance

With this piezoelectric concept, we have introduced a novel flow rate sensing modality in the field of sweat sensing. This does not confine itself to the piezoelectric effect. Using magnetoelastic resonance can be very promising as well. It relies on the magnetostrictive material properties of the sensor and not on the magnetic polarisation and is sensitive to mass loading and fluid drag forces [120, 121, 122]. Using magnetoelastic resonance allows for remote driving and read-out of the device [123], rendering it a passive wearable for flow rate sensing.

Magnetoelastic resonance has been investigated for flow rate sensing based on a suspended sensor [122, 121]. The investigation of a magnetoelastic flow rate sensor at the microfluidic scale is a highly encouraged next step in the development of wearable ultrasonic sweat rate sensing.

9.2 Other applications

Developments made for one application can often be expanded to other industries. This is especially evident for our application of a parking sensor, intended for high voltages and distance measurements between 0.4 and 6.5 meters [114], which now appears to measure flows on the order of μL/min. While we are limited to the filling of a flow front, our flow rate sensor can be used as a low-cost POC microbalance or to non-invasively assess filling of a microfluidic compartment in general. Notably, the sensor does not make direct contact with the fluid in this method. Upon further optimisation, it may also be used to assess physical properties of small liquids. This can be applied for quality control in the biochemical, food or environmental industry.

Appendix A

Concept scoring

A.1 Concept Scoring

A.1.1 Capacitive moisture gradient with evaporation interface

Feasibility
While manufacturing is not a great obstacle, it will be hard to consolidate the calibration for flow rate in this concept. This is expected to be an issue because of the unknown effects of the paper medium over time due to possible chemical alterations and moisture level. To sort out these issues would require more time-intensive optimisation, which is why the feasibility is scored lower.
Score: 2

Novelty
The use of a capacitor and multiple capacitors is not novel in a sweat monitoring context. However, they have exclusively been used to measure the fluid coverage of a channel [53, 61]. Using the degree of capacitance coupled to moisture level of an absorbent medium can be found in an agricultural context [75, 76]. Moreover, evaporation is widely used as a means of driving flow in and out of the channel. In this concept, evaporation is a key process.
Score: 4

Robustness
It is known that both evaporation and capacitance measurements are temperature dependent [17, 60, 124]. Sensitivity to motion should also be tested thoroughly, especially with a flexible substrate, which can be made from PET layers. A rigid solution is then required, limiting comfort and also having implications for the ease of manufacturing. In addition, with measuring moisture level and gradient the capacitance is not qualitatively assessed and therefore error due to motion or temperature will be more problematic. For this reason, robustness is not reassured. For bedside monitoring, it could be at an acceptable degree.
Score: 3

Durability
The durability of this design is debatable due to the interactions with paper and the fact that paper microfluidics is typically disposable [125]. In typical designs, without paper, the channel can be emptied or flushed which limits the contamination of a previous sample. A

drawback from paper is that this cannot be easily done. An option could be to replace the absorbent medium, similar to a reusable lateral flow assay. At the microfluidic scale, this could be a demanding task. Thus, either the paper can remain sufficiently stable over the course of a day or the device has to disposed after a cycle. For this reason, this concept scores low on durability.
Score: 2

Sensitivity
In previous publications, a linear relation was measured with good results [76]. For sweat, it is difficult to ascertain the effect of salt deposition. It is likely that no high sensitivity is achieved over time due to the aforementioned obstacles.
Score: 2

Comfort
Due to the possibility of a rigid patch, it is not scored highly. There is no notable inconvenience aside from this.
Score: 3

Cost
Costs can be quite low, due to relatively simple fabrication. On the other hand, a higher amount of patches is required due to the disposable trait.
Score: 3

Sustainability
It scores low due to the high chance of a single-use application.
Score: 2

A.1.2 Compartment filling

Feasibility
Compartment filling methods with promising results have been described in literature, indicating that this working principle is feasible to measure flow rate [28]. However, the proposed solution is expected to have a more complex structure to achieve drainage. A microfluidic self-siphon is thus more difficult to manufacture than a layered structure with an absorbent layer. The principle is more feasible, conversely, as it does not include multiple phenomena. The device will operate on a microscale and the governing principles must also be carefully researched in order to find an adequate, functional solution. This makes the design more feasible than concept 1, but not to a great extent, as it can be too time-intensive within the limited timespan.
Score: 3

Novelty
Compartment filling methods have been used as a sweat rate sensor, as an adaptation to the droplet counting. However, thus far absorbent media have had a significant role as a driving force to clear the compartment. A drawback of this method is that the absorbent can display different moisture levels. To solve this, another clearing method, novel to sweat sensors, can

be investigated. The microfluidic self siphon is usually applied to centrifugal set-ups [77]. Recent adaptation use capillary forces and gravity to siphon biological samples. Applying this technique would be relatively novel in the compartment filling niche, but wicking has been done previously [41].
Score: 3

Robustness
Robustness is an interesting point for debate. These techniques rely heavy on a particular distance between the fluid and the absorbent. Although the Bond number can be designed to be high, which means gravity has an insignificant impact on the adhesion [48]. Deformation of the flexible substrate or the fluid can influence the measurements too. A rigid substrate would therefore be advantageous, coming at the expense of comfort.
Score: 3

Durability
Discrete droplet counting techniques have shown excellent durability, with a documented lifespan of 200 hours in a tabletop setting with continuous use [54]. It would be the aim to reach a similar or longer life time, as the limiting factor was the absorbent medium in those tests. This concept can potentially be reused for multiple measurement cycles.
Score: 5

Sensitivity
For this working principle, the amount of signal is dependent on the flow rate. A low flow rate of 0.5 $\mu L/\text{min}$ for instance can have around 10 minutes between the signal spikes [28], although this is greatly dependent on the design choices. A balance must be found in facilitating the lower and upper bounds of naturally occurring sweat rates.
Score: 3

Comfort
Due to the possibility of a rigid patch, it is not scored highly. There is no notable inconvenience aside from this.
Score: 3

Cost
It is expected that the costs will be higher as the fabrication might be more complex and intensive, but the reusability and long life span would lower the amount of units required.
Score: 3

Sustainability
This concept scores high because of the long lifespan.
Score: 5

A.1.3 Resonance weighing

Feasibility
This concept is easy to implement and test over the course of a master's thesis. It contains a

single phenomenon which allows for a precise characterisation of the interactions taking place, which can be tackled via a theoretical and empirical route. Moreover, this approach is quite novel and thus chances of success are uncertain. For this reason, it is a compelling concept to explore.
Score: 4

Novelty
As alluded to above, a resonance based microfluidic sweat rate sensor has not been explored before and is thus an innovative concept solution. QCMs are used for biological samples, air humidity sensors and seldom to this end [78, 126].
Score 5

Robustness
QCMs best approximate the goal of this concept and are extremely sensitive. It is important extract the rate of frequency change resultant from the gradual filling of the channel. All the while, there are additional effects from the substrate and skin which also affect the resonator. One can imagine that fabric covering the resonator could also influence the measurement, so good isolation is needed.
Score: 3

Durability
The benefit of weighing a mass difference is that it is not dependent on the sweat composition, nor the residual mass in the channel. This would render the method suitable for several measurement iterations, although assessment is necessary.
Score: 4

Sensitivity
A high sensitivity is likely to be achieved with a quartz resonator. Another piezo-material will likely be used due to lower costs. The sensitivity remains to be determined. The channels are estimated to contain around 15 mg of sweat. At a low flow rate of 0.2 μL for the theoretical channel also used in the requirements section, the device would have to measure 0.4 mg every 2 minutes. QCMs can measure significantly lower masses, down to nanogram differences, but in a tabletop setting [126].
Score: 3

Comfort
The material choice can both be flexible and rigid. In any case, the piezo will remain rigid and can be part of the PCB infrastructure, aiming to minimise user discomfort. The ultrasound will be above hearing level (20 kHz), the ultrasound vibrations will not be audible and are non-invasive. Heating effects should be considered for prolonged use.
Score: 3

Cost
While quartz is expensive, the use of other piezo-materials are considerably cheaper with low cost fabrication. Moreover, the design can be made reusable to spare resources and expenses.
Score: 3

Sustainability
This concept scores high on sustainability, as it can likely be used over multiple measurement cycles.
Score: 5

Appendix B

Preliminary testing

B.1 Contact Angles

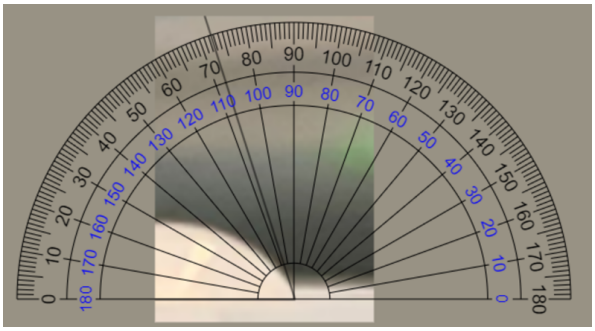

Figure B1: Contact angle of Anycubic Clear Resin.

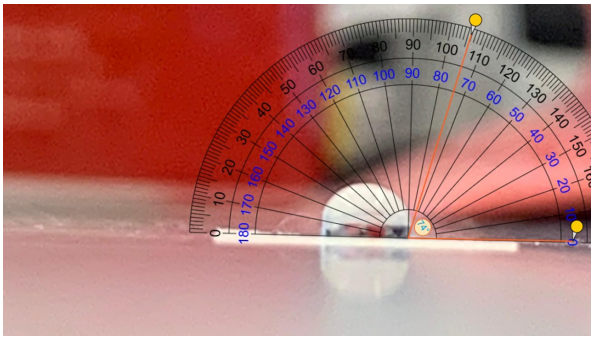

Figure B2: Contact angle bi-adhesive tape.

B.2 Printing set-up

Figure B3: The home printing set-up.

B.3 CUSA sensor

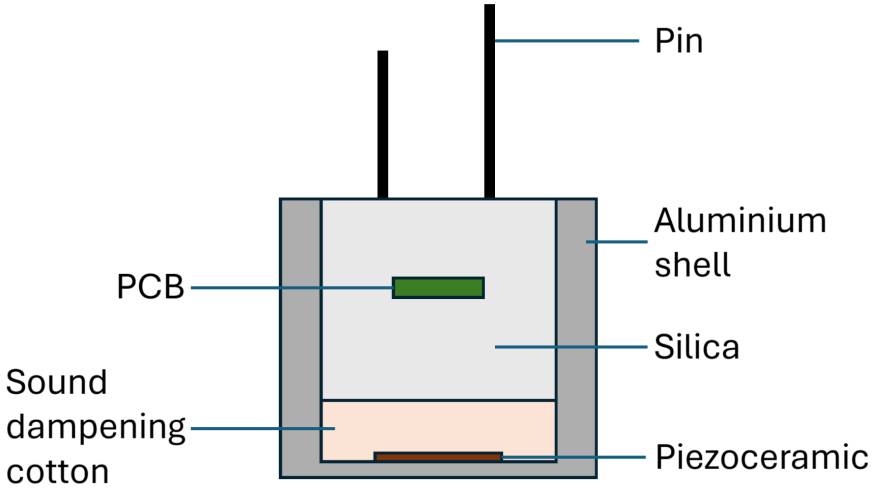

Figure B4: Schematic view of sensor anatomy.

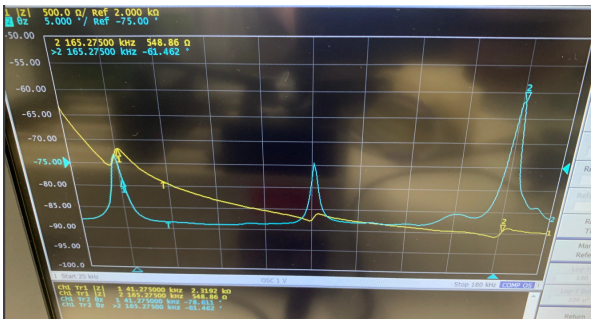

Figure B5: Sensor resonance at around 40 kHz with overtones at around 80 and 160 kHz.

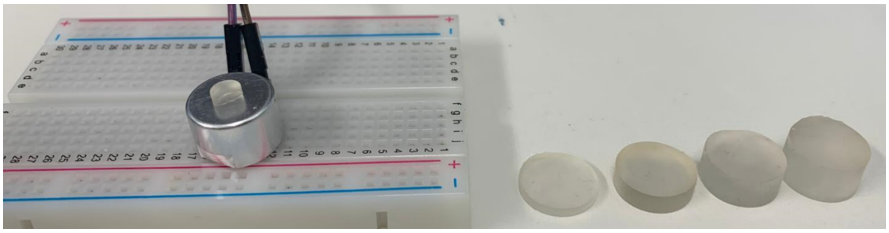

Figure B6: Cylindrical prints used for mass testing, more info in Table B1.

	Mass (mg)	**Fres (kHz)**	**Fres$_{tape(xy)}$ (kHz)**
Bare	0	41.27	-
Disk1 (1mm)	376.67	41.45	34.45
Disk2 (2mm)	784.14	41.625	39.175
Disk3 (4mm)	1115.75	41.625	-
Disk4 (8mm)	1491.82	41.8	-
Tiny Mass	36.86	41.45	39.7
Tape (x)	18	-	40.95
Tape (xy)	18	-	41.225
Tape (y)	18	-	41.5

Table B1: Mass and frequency data with and without tape. Orientation of the sensor was also tested with tape. The x-axis is in line with the pins.

Appendix C

Testing with microfluidic substrates

C.1 Orientation dependency filling

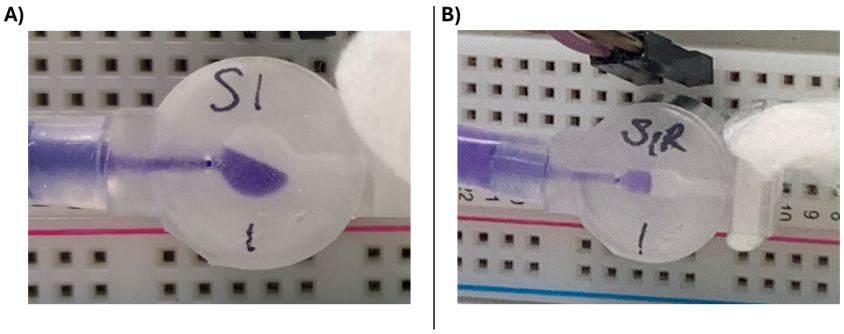

Figure C1: Illustration of filling process for the circular and rectangular reservoir, tilted sideways.

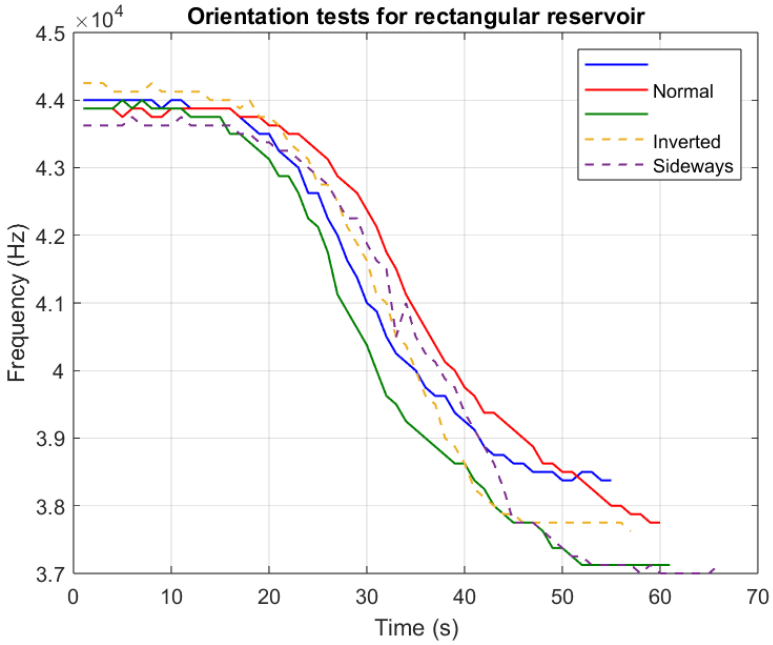

Figure C2: Shift curves in a normal, inverted and sideways position performed at 18 μL/min injection rate.

C.2 Day-to-day variation

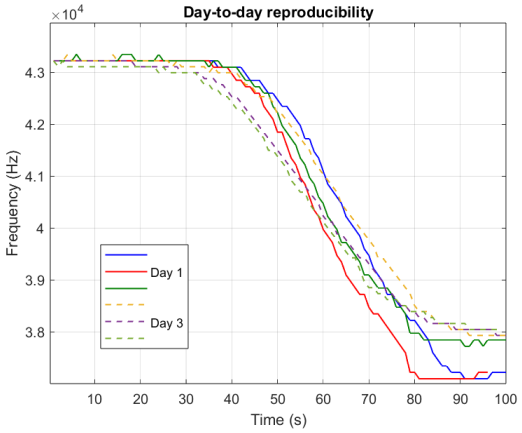

Figure C3: Difference in measurements on different days. A slight difference can be observed.

C.3 Scale test results

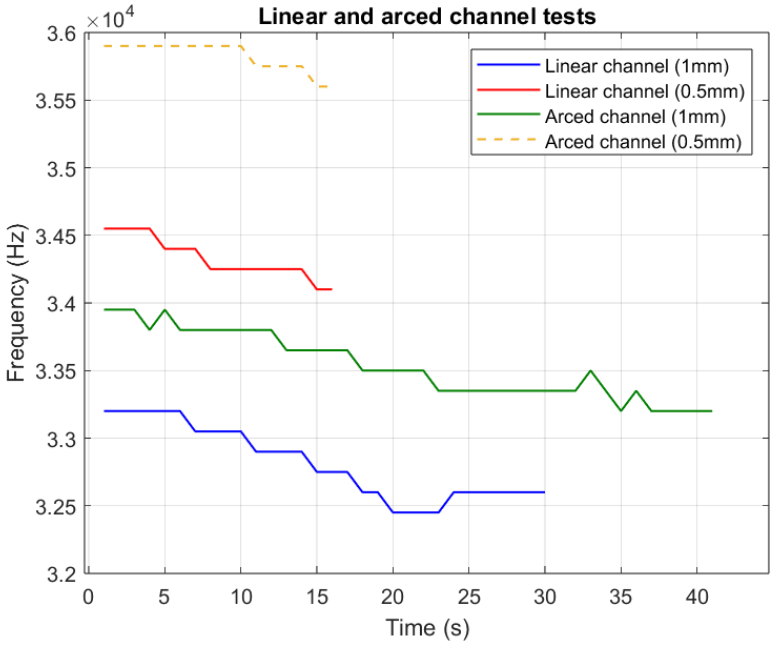

Figure C4: Linear and arced channels of different sizes. Despite a visible shift, the data was not usable for further development.

C.4 Qualitative dynamic system model

A dynamic system was designed to qualitatively assess the influence of a changing stiffness, mass and damping coefficient for a model consisting of 4 masses connected with springs, seen in Figure C5. This was done to simulate the resonance and antiresonance peaks in the data, while the behaviour does not completely match. It therefore serves as an illustration of the phase influence of mass, stiffness and damping.

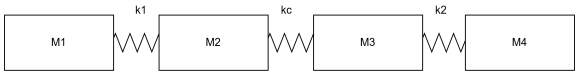

Figure C5: The adopted model consisting of 4 masses, the force is exerted on the first mass. kc is the coupling stiffness.

Two effects were considered that could explain the phase behaviour. Often, the impedance damped to such a degree, that the phase behaviour provided the clearest signal. For a thinner print, multiple peaks could be discerned. For a thicker print, only one peak was found with a range of 30-45 kHz.

One explanation can be the coupling and decoupling of mass subsystems M1-M2 and M3-M4. With a high stiffness, aka a thicker print, mass coupling occurs and energy transfer takes place, potentially merging the phase peaks. If we assume that the second subsystem contains the print in M3, we have two cases. A light mass reduces the inertia, hypothetically increasing the system's resonance. However, it also improves the coupling, bringing the resonant peaks closer together. For a heavier mass, decoupling increases, leading to the phase peaks being

further apart, leading to one clear peak in our measurement range.

With increasing thickness, damping also plays a larger role. This was also evident from the merging of the peaks when water covers the sensor area, because water increases damping. Increasing thickness also leads to higher damping and this is also a likely explanation for the sensor's behaviour.

Added complexity lies in the non-uniform stiffness of the sensor due to bending. A simulation or analytical solution would provide further insights more specific to this case. This was not researched further due to time limitations.

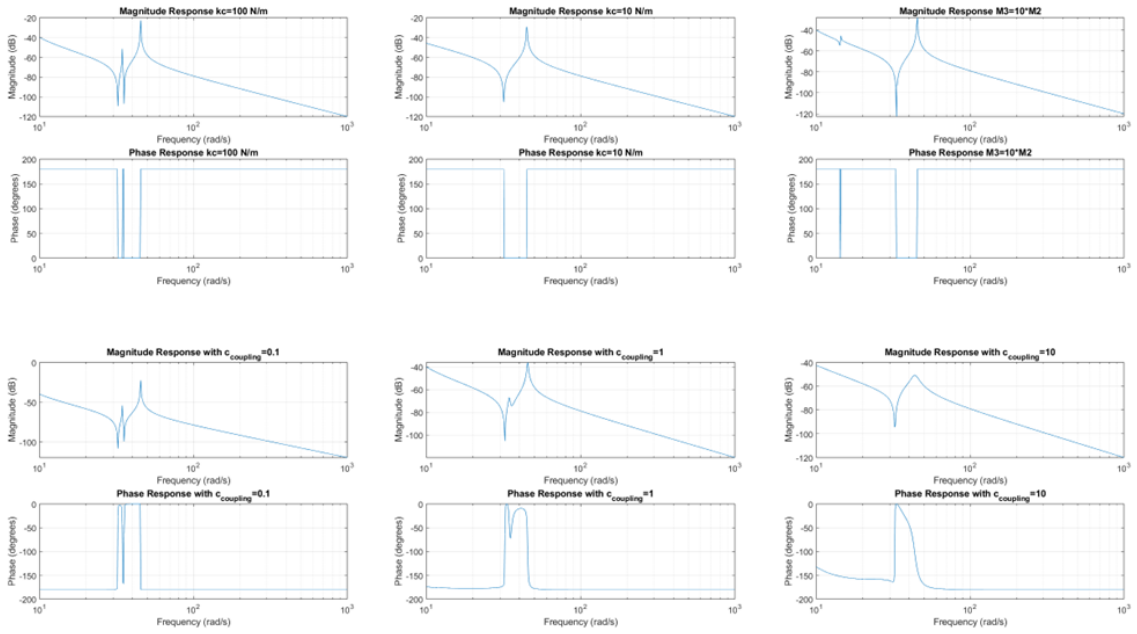

Figure C6: Investigation of influence of parameters. The above left graph was the standard model with M1=1, M2=1, M3=1 and M4=10 kg. k1,k2=1000 N/m, k3=100 N/m.

C.5 Teeth design experiment

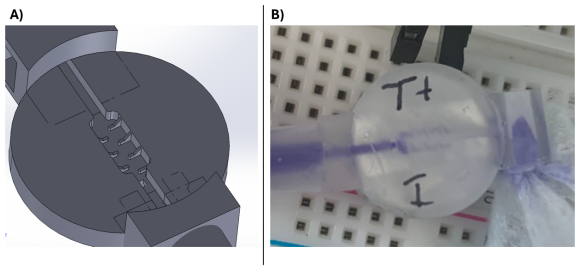

Figure C7: A) Large teeth design. B) Failed refilling steady state.

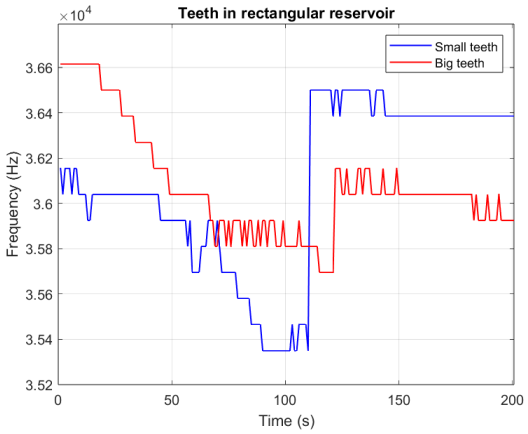

Figure C8: Shift data from the teeth designs to attempt to prevent sideflow for improving wicking performance. However, the shift is not similar to the expected shift from the rectangular reservoir.

Appendix D

Towards a wearable sensor

D.1 Raw data

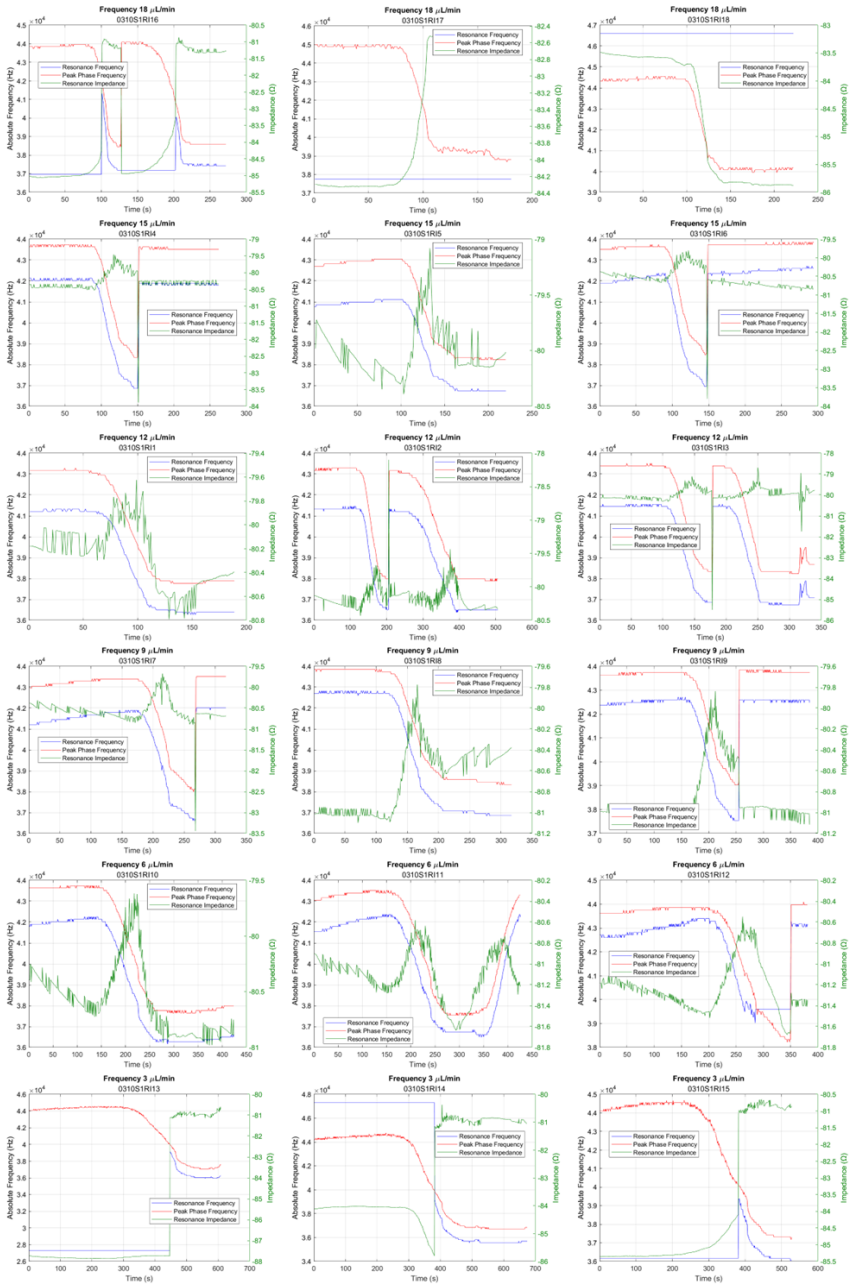

Figure D1: Raw data of rectangular reservoir measurements ranging from 3 to 18 μL/min measured in triplo.

D.2 Capillary effect in resin

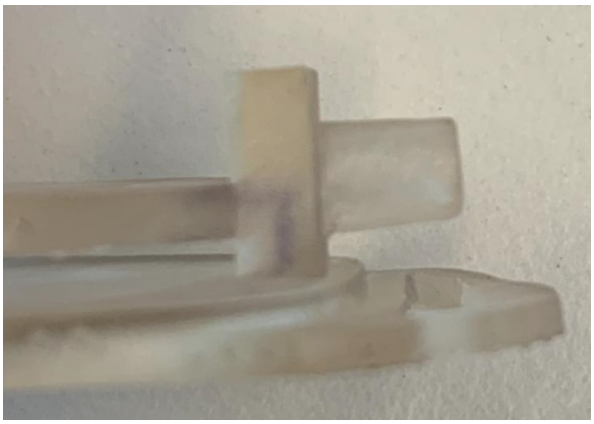

Figure D2: Capillary effect after laying the collector on a coloured water droplet.

D.3 Iontophoresis protocol

This protocol serves as an ancillary for testing of sweat sensing prototypes. On one hand, this protocol provides insight into the practicalities of the built iontophoresis set-up, developed by Thomas Bakker. On the other hand, the produced sweat can be stored for later use, if needed. The experiment consists of two phases: the sweat induction and sweat collection.

Sweat induction
For the sweat induction, the following supplies are needed:

1. Iontophoresis setup (cables, electrodes, power source)
2. Pilogel discs
3. Water (Demi-water)
4. Alcohol
5. Cotton balls or gauze pads
6. Adhesives

First, ensure to be properly hydrated. To prepare for sweat induction, the electrodes can be cleaned if deemed necessary. The skin should be cleaned with alcohol and dried subsequently. The placement of the red electrode is the most important, as this is the electrode from which the pilocarpine will migrate into the skin. First, the pilogel disc must be loaded in the electrode. To mitigate the risks of burns, also wet the area of skin where the electrode will be placed with a drop of water. Then, place and fix the loaded electrode on the wrinkleless, hairless and muscular part of the volar forearm and without directly palpable tendons or bone. Make sure good contact with the skin and disc is ensured. The same procedure should be performed for the black electrode. This can be placed at around 10 cm distance. The iontophoresis set-up can be set to 1 mA for 5 minutes. Afterwards, the electrodes and gels can be removed and the skin cleaned with alcohol and dried with the pads. The pilocarpine boosts sweat production for around an hour, with its peak activity at around 20 minutes after stimulation.

Sweat collection
For the sweat collection, the following additional supplies are needed:

1. Microbalance
2. Parafilm (optional)

After sweat induction, an absorbent patch can be applied to the stimulated region of the forearm or a wearable prototype. The patch consists of an absorbent material (gauze pads/cotton ball) of known weight (measured in advance) covered with Parafilm and attached with an adhesive. The patch/prototype can remain in place over the course of an hour, but can be replaced, if necessary, to prevent saturation of the absorbent. After the collection, the absorbent patch or prototype is weighed again. The measurements from weighing the patches can be utilised to estimate the sweat output upon pilocarpine iontophoresis. As no analysis of sweat composition is intended, normal water can be used instead of deionised

water. Moreover, the absorbent is weighed before extraction, and thus it is not critical to extract the full contents of the absorbent patch.

D.4 Smoothing

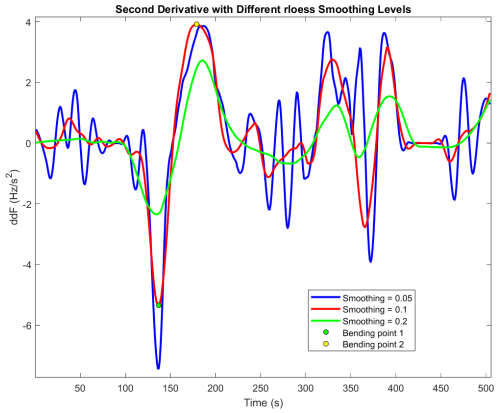

Figure D3: Showcase of smoothing effects on the 2nd derivative of the characterisation algorithm. Bending points are added for clarity.

D.5 Sigmoid fit

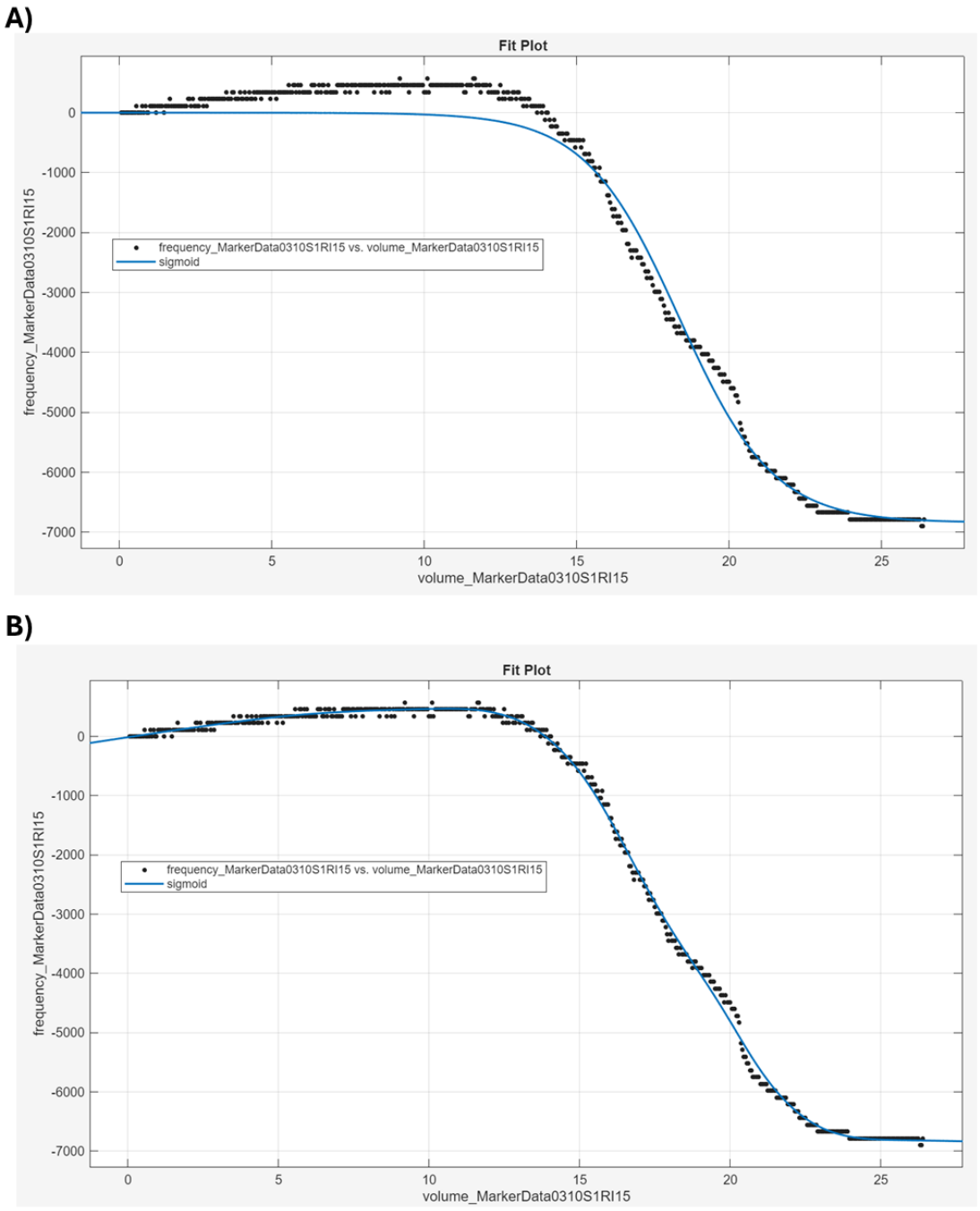

Figure D4: A) Sigmoid fit without manual windowing. B) Sigmoid fit with manual windowing.

D.6 Flow rate assessment

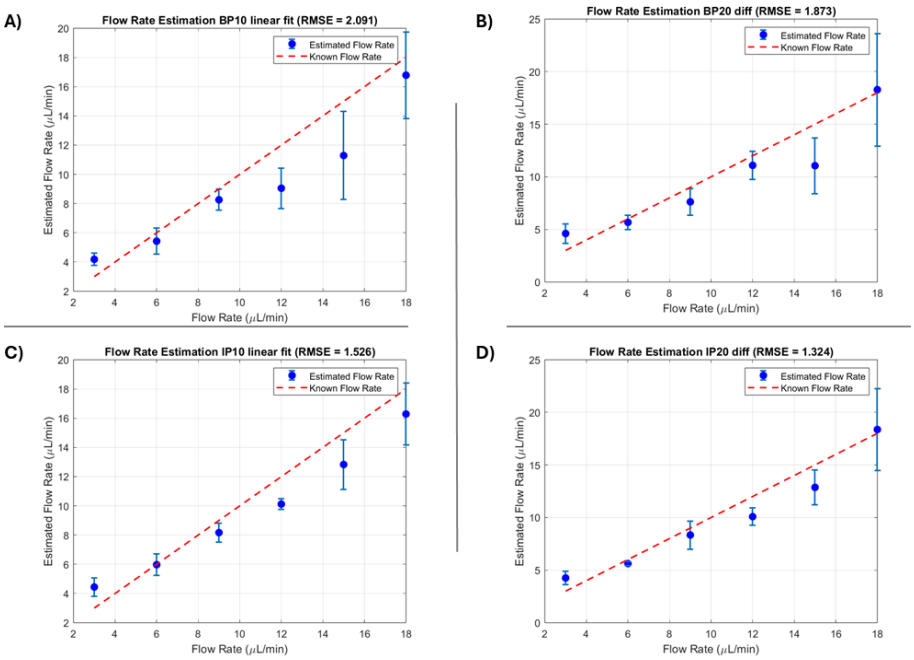

Figure D5: Assessment of the flow rate characterisation approaches. A) flow rate estimation for a linear fit with 0.1 rloess smoothing between two bending points, B) estimation for a difference between two bending points with 0.2 smoothing. C) estimation for a linear fit with 0.1 rloess smoothing between the first bending point and the inflection point, D) estimation for a difference between the first bending point and the inflection point with 0.2 smoothing.

D.7 Flow rate estimates on existing data

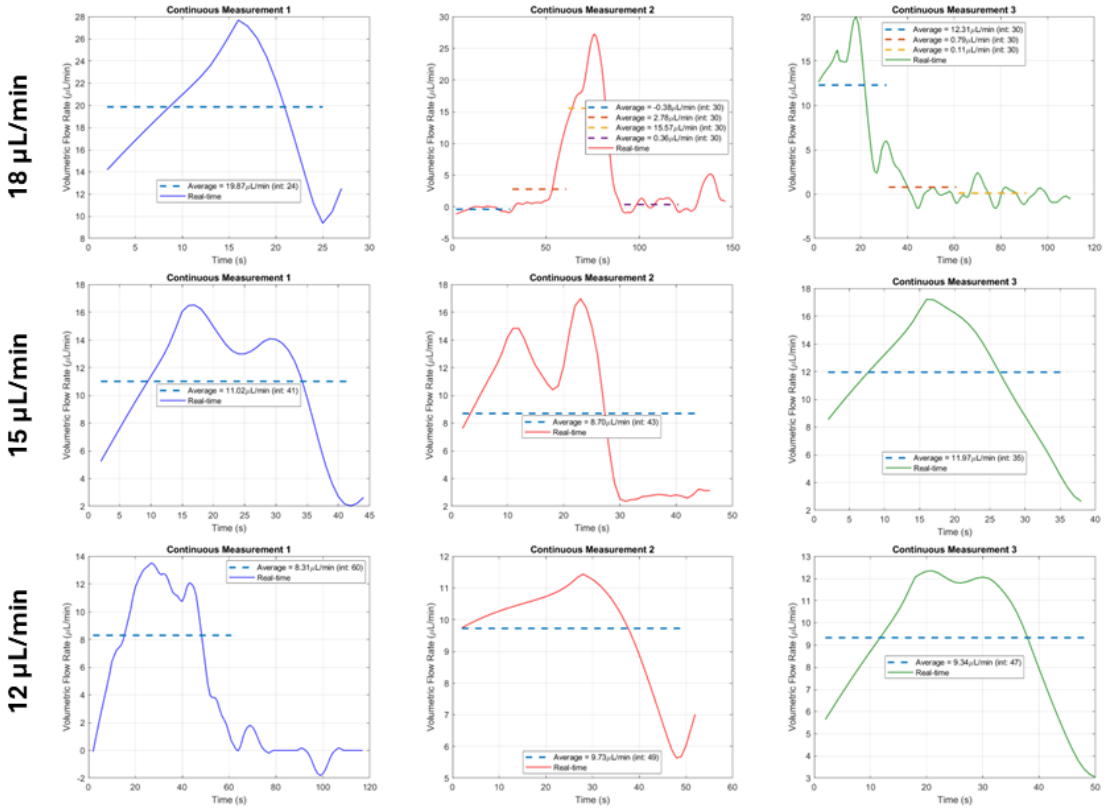

Figure D6: Flow rate estimation using F/V=-614.26 Hz/μL for flow rates 12-18 μL/min.

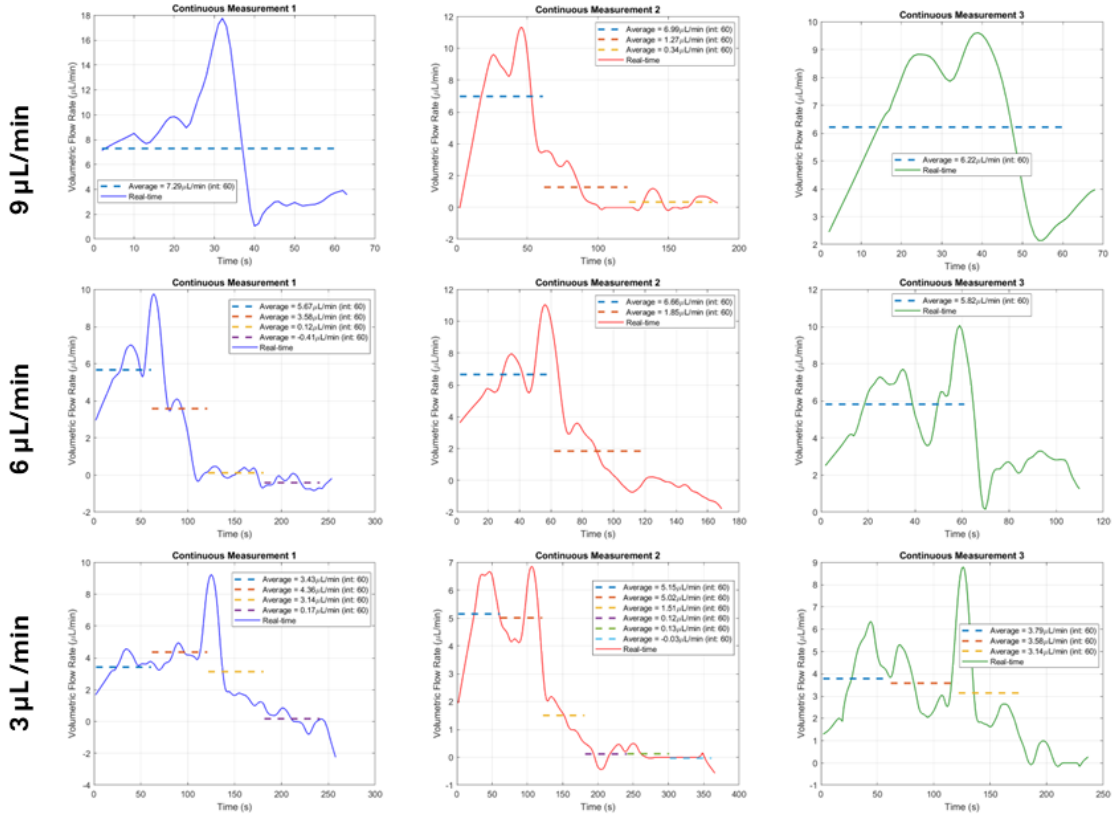

Figure D7: Flow rate estimation using F/V=-614.26 Hz/μL for flow rates 3-9 μL/min.

Bibliography

[1] Wei Gao et al. "Flexible Electronics toward Wearable Sensing". In: *Acc. Chem. Res.* (Feb. 2019). DOI: 10.1021/acs.accounts.8b00500.

[2] Fupeng Gao et al. "Wearable and flexible electrochemical sensors for sweat analysis: a review". In: *Microsyst. Nanoeng.* 9.1 (Jan. 2023), pp. 1–21. ISSN: 2055-7434. DOI: 10.1038/s41378-022-00443-6.

[3] Sam Emaminejad et al. "Autonomous sweat extraction and analysis applied to cystic fibrosis and glucose monitoring using a fully integrated wearable platform". In: *Proceedings of the National Academy of Sciences* 114.18 (May 2017), pp. 4625–4630. DOI: 10.1073/pnas.1701740114.

[4] Qing Zhang et al. "Smartphone-based wearable microfluidic electrochemical sensor for on-site monitoring of copper ions in sweat without external driving". In: *Talanta* 266 (Jan. 2024), p. 125015. DOI: 10.1016/j.talanta.2023.125015.

[5] K. Longman et al. "Noninvasive drug adherence monitoring of antipsychotic patients via finger sweat testing". In: *Front. Chem.* 11 (Aug. 2023), p. 1245089. ISSN: 2296-2646. DOI: 10.3389/fchem.2023.1245089.

[6] Noé Brasier and Jens Eckstein. "Sweat as a Source of Next-Generation Digital Biomarkers". In: *Digital Biomarkers* 3.3 (Jan. 2020), pp. 155–165. DOI: 10.1159/000504387.

[7] Carmela Niederberger et al. "Wearable sweat analysis to determine biological age". In: *Trends Biotechnology* 41.9 (Sept. 2023), pp. 1113–1116. ISSN: 0167-7799. DOI: 10.1016/j.tibtech.2023.02.001.

[8] Lindsay B. Baker et al. "Skin-interfaced microfluidic system with personalized sweating rate and sweat chloride analytics for sports science applications". In: *Sci. Adv.* (Dec. 2020). DOI: 10.1126/sciadv.abe3929.

[9] Balaji Ramachandran and Ying-Chih Liao. "Microfluidic wearable electrochemical sweat sensors for health monitoring". In: *Biomicrofluidics* 16.5 (Sept. 2022). DOI: 10.1063/5.0116648.

[10] Shruti Patle and Dinesh Rotake. "Recent advances, technological challenges and requirements to predict the future treads in wearable sweat sensors: A critical review". In: *Microchem. J.* 200 (May 2024), p. 110457. ISSN: 0026-265X. DOI: 10.1016/j.microc.2024.110457.

[11] Noelle Davis et al. "The challenges and promise of sweat sensing". In: *Nat. Biotechnol.* 42.6 (June 2024), pp. 860–871. ISSN: 1546-1696. DOI: 10.1038/s41587-023-02059-1.

[12] Alejandra Castelblanco et al. "Colorimetric Sensor Reading and Illumination Correction via Multi-Task Deep-Learning". In: *Annu. Int. Conf. IEEE Eng. Med. Biol. Soc.* 2023:1-5. (July 2023). ISSN: 2694-0604. DOI: 10.1109/EMBC40787.2023.10340185. eprint: 38083521.

[13] Andre Childs et al. "Diving into Sweat: Advances, Challenges, and Future Directions in Wearable Sweat Sensing". In: *ACS Nano* (Aug. 2024). DOI: 10.1021/acsnano.4c10344.

[14] Lindsay B. Baker and Anthony S. Wolfe. "Physiological mechanisms determining eccrine sweat composition". In: *Eur. J. Appl. Physiol.* 120.4 (Apr. 2020), pp. 719–752. ISSN: 1439-6327. DOI: 10.1007/s00421-020-04323-7.

[15] Nigel A. S. Taylor and Christiano A. Machado-Moreira. "Regional variations in transepidermal water loss, eccrine sweat gland density, sweat secretion rates and electrolyte composition in resting and exercising humans". In: *Extreme Physiol. Med.* 2.1 (Dec. 2013), pp. 1–30. ISSN: 2046-7648. DOI: 10.1186/2046-7648-2-4.

[16] Lindsay B. Baker. "Physiology of sweat gland function: The roles of sweating and sweat composition in human health". In: *Temperature* (July 2019). URL: https://www.tandfonline.com/doi/full/10.1080/23328940.2019.1632145.

[17] C Nie. "Integrated evaporation driven microfluidic device for continuous sweat monitoring". PhD thesis. Faculty of Mechanical Engineering, Technische Universiteit Eindhoven, 2016.

[18] Z. Sonner et al. "The microfluidics of the eccrine sweat gland, including biomarker partitioning, transport, and biosensing implications". In: *Biomicrofluidics* 9.3 (May 2015). DOI: 10.1063/1.4921039.

[19] Caroline J. Smith and George Havenith. "Upper body sweat mapping provides evidence of relative sweat redistribution towards the periphery following hot-dry heat acclimation". In: *Temperature* (Jan. 2019). URL: https://www-tandfonline-com.tudelft.idm.oclc.org/doi/full/10.1080/23328940.2019.1570777.

[20] Phillip Simmers et al. "Prolonged and localized sweat stimulation by iontophoretic delivery of the slowly-metabolized cholinergic agent carbachol". In: *J. Dermatol. Sci.* 89.1 (Jan. 2018), pp. 40–51. ISSN: 0923-1811. DOI: 10.1016/j.jdermsci.2017.10.013.

[21] Manabu Shibasaki and Craig G. Crandall. "Mechanisms and controllers of eccrine sweating in humans". In: *Front. Biosci. (Schol. Ed).* 2.2 (Jan. 2010), pp. 685–696. ISSN: 1945-0524. DOI: 10.2741/s94. eprint: 20036977.

[22] Noé Brasier et al. "Non-invasive Drug Monitoring of β-Lactam Antibiotics Using Sweat Analysis—A Pilot Study". In: *Front. Med.* 7 (Aug. 2020), p. 538087. ISSN: 2296-858X. DOI: 10.3389/fmed.2020.00476.

[23] Sean W Harshman et al. "Rate normalization for sweat metabolomics biomarker discovery". In: *Talanta* 223 (2021), p. 121797.

[24] Hasan M Al-Dorzi, Shmylan A Al Harbi, and Yaseen M Arabi. "Antibiotic therapy of pneumonia in the obese patient: dosing and delivery". In: *Current opinion in infectious diseases* 27.2 (2014), pp. 165–173.

[25] C. E. Tucker, A. M. Lockwood, and N. H. Nguyen. "Antibiotic dosing in obesity: the search for optimum dosing strategies". In: *Clinical Obesity* 4.6 (Dec. 2014), pp. 287–295. ISSN: 1758-8111. DOI: 10.1111/cob.12076.

[26] Noé Brasier et al. "A three-level model for therapeutic drug monitoring of antimicrobials at the site of infection". In: *The Lancet Infectious Diseases* 23.10 (2023), e445–e453.

[27] Noé Brasier et al. "Digital biomarkers from sweat analysis for therapeutic drug monitoring in soft tissue infections". In: *Proceedings of the 2021 workshop on future of digital biomarkers*. 2021, pp. 45–50.

[28] Shuqi Wang et al. "An unconventional vertical fluidic-controlled wearable platform for synchronously detecting sweat rate and electrolyte concentration". In: *Biosensors and Bioelectronics* 210 (2022), p. 114351.

[29] Xinghui Lin et al. "Daily peritoneal ultrafiltration predicts patient and technique survival in anuric peritoneal dialysis patients". In: *Nephrol. Dial. Transplant.* 25.7 (July 2010), pp. 2322–2327. ISSN: 0931-0509. DOI: 10.1093/ndt/gfq001.

[30] Maria-Eleni Alexandrou, Olga Balafa, and Pantelis Sarafidis. "Assessment of Hydration Status in Peritoneal Dialysis Patients: Validity, Prognostic Value, Strengths, and Limitations of Available Techniques". In: *Am. J. Nephrol.* 51.8 (Aug. 2020), pp. 589–612. ISSN: 0250-8095. DOI: 10.1159/000509115.

[31] Isabel Juan García et al. "Echocardiographic impact of hydration status in dialysis patients". In: *Nefrología (English Edition)* 32.1 (Jan. 2012), pp. 94–102. ISSN: 2013-2514. DOI: 10.3265/Nefrologia.pre2011.Nov.10867.

[32] Norio Hanafusa et al. "Is there a role for diaphoresis therapy for advanced chronic kidney disease patients?" In: *Journal of Renal Nutrition* 27.5 (2017), pp. 295–302.

[33] Bowen Zhong et al. "Wearable Sweat Loss Measuring Devices: From the Role of Sweat Loss to Advanced Mechanisms and Designs". In: *Adv. Sci.* 9.1 (Jan. 2022), p. 2103257. ISSN: 2198-3844. DOI: 10.1002/advs.202103257.

[34] Joy N. Hussain, Nitin Mantri, and Marc M. Cohen. "Working Up a Good Sweat – The Challenges of Standardising Sweat Collection for Metabolomics Analysis". In: *Clinical Biochemist Reviews* 38.1 (Feb. 2017), p. 13. URL: https://www-ncbi-nlm-nih-gov.tudelft.idm.oclc.org/pmc/articles/PMC5548369.

[35] Andrew Best, Daniel E Lieberman, and Jason M Kamilar. "Diversity and evolution of human eccrine sweat gland density". In: *Journal of Thermal Biology* 84 (2019), pp. 331–338.

[36] Lisa Klous et al. "The effect of sweat sample storage condition on sweat content". In: *Temperature* (July 2021). ISSN: 2332-8940. DOI: 10.1080/23328940.2020.1867294.

[37] Haixia Yu and Jintao Sun. "Sweat detection theory and fluid driven methods: A review". In: *Nanotechnology and Precision Engineering* 3.3 (Aug. 2020), pp. 126–140. DOI: 10.1016/j.npe.2020.08.003.

[38] Ayokunle Olanrewaju et al. "Capillary microfluidics in microchannels: from microfluidic networks to capillaric circuits". In: *Lab Chip* 18.16 (2018), pp. 2323–2347. DOI: 10.1039/C8LC00458G.

[39] Hansang Cho et al. "How the capillary burst microvalve works". In: *J. Colloid Interface Sci.* 306.2 (Feb. 2007), pp. 379–385. ISSN: 0021-9797. DOI: 10.1016/j.jcis.2006.10.077.

[40] Yuxin He et al. "Laser-Cutted Epidermal Microfluidic Patch with Capillary Bursting Valves for Chronological Capture, Storage, and Colorimetric Sensing of Sweat". In: *Biosensors* 13.3 (Mar. 2023), p. 372. ISSN: 2079-6374. DOI: 10.3390/bios13030372.

[41] Mengyuan Liu et al. "Adaptively resettable microfluidic patch for sweat rate and electrolytes detection". In: *Biosensors and Bioelectronics* 257 (2024), p. 116299.

[42] Xiujun Fu et al. "Microfluidic sweat patch based on capillary force and evaporation pump for real-time continuous sweat analysis". In: *Biomicrofluidics* 18.3 (May 2024), p. 034106. ISSN: 1932-1058. DOI: 10.1063/5.0208075. eprint: 38841318.

[43] Tim Shay, Michael D. Dickey, and Orlin D. Velev. "Hydrogel-enabled osmotic pumping for microfluidics: towards wearable human-device interfaces". In: *Lab Chip* 17.4 (Feb. 2017), pp. 710–716. ISSN: 1473-0197. DOI: 10.1039/C6LC01486K.

[44] Hnin Yin Yin Nyein et al. "A wearable patch for continuous analysis of thermoregulatory sweat at rest". In: *Nat. Commun.* 12.1823 (Mar. 2021), pp. 1–13. ISSN: 2041-1723. DOI: 10.1038/s41467-021-22109-z.

[45] Mengyuan Liu et al. "Perspiration permeable, textile embeddable microfluidic sweat sensor". In: *Biosensors and Bioelectronics* 237 (2023), p. 115504.

[46] Xiao-Ming Chen et al. "A Capillary-Evaporation Micropump for Real-Time Sweat Rate Monitoring with an Electrochemical Sensor". In: *Micromachines* 10.7 (July 2019), p. 457. ISSN: 2072-666X. DOI: 10.3390/mi10070457.

[47] Jing-min Li et al. "A bio-inspired micropump based on stomatal transpiration in plants". In: *Lab Chip* 11.16 (Aug. 2011), pp. 2785–2789. ISSN: 1473-0197. DOI: 10.1039/C1LC20313D.

[48] Nam-Trung Nguyen and Steven T Wereley. *Fundamentals and applications of microfluidics*. Artech house, 2002.

[49] Yu Han et al. "Sweat Sensor Based on Wearable Janus Textiles for Sweat Collection and Microstructured Optical Fiber for Surface-Enhanced Raman Scattering Analysis". In: *ACS Sens.* 8.12 (Dec. 2023), pp. 4774–4781. DOI: 10.1021/acssensors.3c01863.

[50] Jiaqi Niu et al. "A Fully Elastic Wearable Electrochemical Sweat Detection System of Tree-Bionic Microfluidic Structure for Real-Time Monitoring". In: *Small* n/a.n/a (Nov. 2023), p. 2306769. ISSN: 1613-6810. DOI: 10.1002/smll.202306769.

[51] Annemarijn S. M. Steijlen et al. "Low-Cost Wearable Fluidic Sweat Collection Patch for Continuous Analyte Monitoring and Offline Analysis". In: *Anal. Chem.* 94.18 (May 2022), pp. 6893–6901. ISSN: 0003-2700. DOI: 10.1021/acs.analchem.2c01052.

[52] Mallika Bariya et al. "Resettable Microfluidics for Broad-Range and Prolonged Sweat Rate Sensing". In: *ACS Sens.* 7.4 (Apr. 2022), pp. 1156–1164. DOI: 10.1021/acssensors.2c00177.

[53] Dong-Hoon Choi et al. "A Capacitive Sweat Rate Sensor for Continuous and Real-Time Monitoring of Sweat Loss". In: *ACS Sens.* (Dec. 2020). DOI: 10.1021/acssensors.0c01219.

[54] Jessica Francis et al. "Digital nanoliter to milliliter flow rate sensor with in vivo demonstration for continuous sweat rate measurement". In: *Lab Chip* 19.1 (Dec. 2018), pp. 178–185. ISSN: 1473-0189. DOI: 10.1039/C8LC00968F.

[55] Andrew Brueck et al. "A Real-Time Wireless Sweat Rate Measurement System for Physical Activity Monitoring". In: *Sensors* 18.2 (Feb. 2018), p. 533. ISSN: 1424-8220. DOI: 10.3390/s18020533.

[56] Hnin Yin Yin Nyein et al. "Regional and correlative sweat analysis using high-throughput microfluidic sensing patches toward decoding sweat". In: *Science Advances* 5.8 (Aug. 2019). DOI: 10.1126/sciadv.aaw9906.

[57] Murat A Yokus et al. "Wearable Sweat Rate Sensors". In: *2020 IEEE SENSORS*. IEEE. 2020, pp. 1–4.

[58] Sung Bong Kim et al. "Soft, skin-interfaced microfluidic systems with wireless, battery-free electronics for digital, real-time tracking of sweat loss and electrolyte composition". In: *Small* 14.45 (2018), p. 1802876.

[59] Haisong Lin et al. "Autonomous wearable sweat rate monitoring based on digitized microbubble detection". In: *Lab Chip* 22.22 (Nov. 2022), pp. 4267–4275. ISSN: 1473-0197. DOI: 10.1039/D2LC00670G.

[60] Mahmoud Khademi and Dominik P. J. Barz. "Structure of the Electrical Double Layer Revisited: Electrode Capacitance in Aqueous Solutions". In: *Langmuir* (Mar. 2020). DOI: 10.1021/acs.langmuir.0c00024.

[61] Yuksel Temiz and Emmanuel Delamarche. "Sub-nanoliter, real-time flow monitoring in microfluidic chips using a portable device and smartphone". In: *Sci. Rep.* 8.10603 (July 2018), pp. 1–11. ISSN: 2045-2322. DOI: 10.1038/s41598-018-28983-w.

[62] Yuki Hashimoto et al. "Wearable Microfluidic Sensor for the Simultaneous and Continuous Monitoring of Local Sweat Rates and Electrolyte Concentrations". In: *Micromachines* 13.4 (Apr. 2022), p. 575. ISSN: 2072-666X. DOI: 10.3390/mi13040575.

[63] Giusy Matzeu et al. "A Wearable Device for Monitoring Sweat Rates via Image Analysis". In: *IEEE Trans. Biomed. Eng.* 63.8 (Sept. 2015), pp. 1672–1680. DOI: 10.1109/TBME.2015.2477676.

[64] Shanliangzi Liu et al. "Soft, environmentally degradable microfluidic devices for measurement of sweat rate and total sweat loss and for colorimetric analysis of sweat biomarkers". In: *EcoMat* 5.1 (Jan. 2023), e12270. ISSN: 2567-3173. DOI: 10.1002/eom2.12270.

[65] Roozbeh Ghaffari et al. "The Gx Sweat Patch for personalized hydration management". In: *Nat. Rev. Bioeng.* 1.1 (Jan. 2023), pp. 5–7. ISSN: 2731-6092. DOI: 10.1038/s44222-022-00005-5.

[66] Gatorade. *Gx Sweat Patch Gx Sweat Patch Accessory*. [Online; accessed 26. Sep. 2024]. Mar. 2022. URL: https://www.gatorade.com/equipment/gx-sweat-patch/gx-sweat-patch-00052000052596.

[67] Jonathan T. Reeder et al. "Resettable skin interfaced microfluidic sweat collection devices with chemesthetic hydration feedback". In: *Nat. Commun.* 10.5513 (Dec. 2019), pp. 1–12. ISSN: 2041-1723. DOI: 10.1038/s41467-019-13431-8.

[68] Kyeongha Kwon et al. "An on-skin platform for wireless monitoring of flow rate, cumulative loss and temperature of sweat in real time". In: *Nat. Electron.* 4.4 (Apr. 2021), pp. 302–312. ISSN: 2520-1131. DOI: 10.1038/s41928-021-00556-2.

[69] Shree Thirumalaikumar, Matthew Douthwaite, and Pantelis Georgiou. "Design of a Calorimetric Flow Rate Sensor for On-Body Sweat Monitoring". In: *2021 IEEE International Symposium on Circuits and Systems (ISCAS)*. 2021, pp. 1–5. DOI: 10.1109/ISCAS51556.2021.9401411.

[70] Emma J. M. Moonen et al. "Wearable sweat sensing for prolonged, semicontinuous, and nonobtrusive health monitoring". In: *View* 1.4 (Dec. 2020), p. 20200077. ISSN: 2688-268X. DOI: 10.1002/VIW.20200077.

[71] Audrey Reynaerts et al. "Needle-free iontophoresis-driven β-adrenergic sweat rate test". In: *J. Cyst. Fibros.* 21.3 (May 2022), pp. 407–415. ISSN: 1569-1993. DOI: 10.1016/j.jcf.2021.08.012.

[72] *Macroduct® Advanced*. [Online; accessed 17. Nov. 2024]. Nov. 2024. URL: https://macroductadvanced.com/macroductadvanced.html.

[73] Scott L. Davis et al. "Pilocarpine-induced sweat gland function in individuals with multiple sclerosis". In: *J. Appl. Physiol.* (May 2005). URL: https://journals.physiology.org/doi/full/10.1152/japplphysiol.00860.2004.

[74] Van-Thuan Nguyen et al. "Recent advances in high-sensitivity detection methods for paper-based lateral-flow assay". In: *Biosens. Bioelectron.* 152 (Mar. 2020). [Online; accessed 24. Nov. 2024], p. 112015. ISSN: 0956-5663. DOI: 10.1016/j.bios.2020.112015.

[75] Nicholas R. Harris and Alexander Stonard. "A Printed Capacitance Sensor for Soil Moisture Measurement". In: *Proceedings* 2.13 (Dec. 2018), p. 705. ISSN: 2504-3900. DOI: 10.3390/proceedings2130705.

[76] Chari V. Kandala and Jaya Sundaram. "Nondestructive Measurement of Moisture Content Using a Parallel-Plate Capacitance Sensor for Grain and Nuts". In: *IEEE Sensors Journal* 10.7 (2010), pp. 1282–1287. DOI: 10.1109/JSEN.2010.2041446.

[77] Nuno M. Reis et al. "Gravity-Driven Microfluidic Siphons: Fluidic Characterization and Application to Quantitative Immunoassays". In: *ACS Sens.* 6.12 (Dec. 2021), pp. 4338–4348. DOI: 10.1021/acssensors.1c01524.

[78] Antonio Arnau et al. *Piezoelectric transducers and applications*. Vol. 2004. Springer, 2004.

[79] Muhammad Ali Shah et al. "Classifications and Applications of Inkjet Printing Technology: A Review". In: *IEEE Access* 9 (2021), pp. 140079–140102. DOI: 10.1109/ACCESS.2021.3119219.

[80] F. Barreras, H. Amaveda, and A. Lozano. "Transient high-frequency ultrasonic water atomization". In: *Exp. Fluids* 33.3 (Sept. 2002), pp. 405–413. ISSN: 1432-1114. DOI: 10.1007/s00348-002-0456-1.

[81] Noémie Elgrishi et al. "A Practical Beginner's Guide to Cyclic Voltammetry". In: *J. Chem. Educ.* 95.2 (Feb. 2018), pp. 197–206. ISSN: 0021-9584. DOI: 10.1021/acs.jchemed.7b00361.

[82] Maria A Komkova et al. “Mass transport limitations for electrochemical sensing in low-flux excretory fluids”. In: *Biosensors and Bioelectronics* 227 (2023), p. 115148.

[83] Mohammad Irfan Hajam and Mohammad Mohsin Khan. “Microfluidics: a concise review of the history, principles, design, applications, and future outlook”. In: *Biomater. Sci.* 12.2 (2024), pp. 218–251. DOI: 10.1039/D3BM01463K.

[84] IM Mahbubul. *Preparation, characterization, properties, and application of nanofluid*. William Andrew, 2018.

[85] Thomas Young. *III. An essay on the cohesion of fluids*. [Online; accessed 9. Nov. 2024]. Dec. 1805. DOI: 10.1098/rstl.1805.0005.

[86] Jungil Choi et al. “Thin, Soft, Skin-Mounted Microfluidic Networks with Capillary Bursting Valves for Chrono-Sampling of Sweat”. In: *Adv. Healthcare Mater.* 6.5 (Mar. 2017), p. 1601355. ISSN: 2192-2659. DOI: 10.1002/adhm.201601355.

[87] Michael Rabl, Mario Jungwirth, and Peter Zeller. “P1. 6-Development of Bending-Type Ultrasonic Transducers with Rotational Symmetry”. In: *Proceedings SENSOR 2009, Volume II* (2009), pp. 247–252.

[88] E RAY LANKESTER. “Light Produced by Rubbing Quartz Pebbles Together”. In: *Nature* 106.2662 (1920), pp. 310–310.

[89] Paddy French, Simon Middelhoek, and Maurice Audet. *Silicon Sensors and Actuators*. Delft Academic Press, Nov. 2021.

[90] Wayne Storr. “Parallel Resonance and Parallel RLC Resonant Circuit”. In: *Basic Electronics Tutorials* (Aug. 2022). URL: https://www.electronics-tutorials.ws/accircuits/parallel-resonance.html.

[91] Abdulrahman Alassi, Mohieddine Benammar, and Dan Brett. “Quartz Crystal Microbalance Electronic Interfacing Systems: A Review”. In: *Sensors* 17.12 (Dec. 2017), p. 2799. ISSN: 1424-8220. DOI: 10.3390/s17122799.

[92] Günter Sauerbrey. “Verwendung von Schwingquarzen zur Wägung dünner Schichten und zur Mikrowägung”. In: *Z. Phys.* 155.2 (Apr. 1959), pp. 206–222. ISSN: 0044-3328. DOI: 10.1007/BF01337937.

[93] K Keiji Kanazawa and Joseph G Gordon II. “The oscillation frequency of a quartz resonator in contact with liquid”. In: *Analytica Chimica Acta* 175 (1985), pp. 99–105. DOI: 10.1016/S0003-2670(00)82721-X.

[94] J-W Thies et al. “Microfluidic quartz-crystal-microbalance (QCM) sensors with specialized immunoassays for extended measurement range and improved reusability”. In: *Microelectronic Engineering* 179 (2017). [Online; accessed 11. Nov. 2024], pp. 25–30. DOI: 10.1016/j.mee.2017.04.023.

[95] MIS Verıssimo et al. “Suitability of PZT ceramics for mass sensors versus widespread used quartz crystals”. In: *Sensors and Actuators B: Chemical* 95.1-3 (2003). [Online; accessed 11. Nov. 2024], pp. 25–31. DOI: 10.1016/S0925-4005(03)00397-6.

[96] Shrinivas G Joshi and Yu Jin. “Application of a surface-acoustic-wave device for measurement of liquid flow rate”. In: *IEEE Transactions on Ultrasonics, Ferroelectrics, and Frequency Control* 37.5 (1990), pp. 475–477.

[97] Xuyang Zhou et al. "Review on piezoelectric actuators: materials, classifications, applications, and recent trends". In: *Front. Mech. Eng.* 19.1 (Feb. 2024), pp. 1–29. ISSN: 2095-0241. DOI: 10.1007/s11465-023-0772-0.

[98] Mostafa R. A. Nabawy, Ben Parslew, and William J. Crowther. "Dynamic performance of unimorph piezoelectric bending actuators". In: *Proceedings of the Institution of Mechanical Engineers, Part I: Journal of Systems and Control Engineering* (Oct. 2014). DOI: 10.1177/0959651814552810.

[99] Antonio Messineo et al. "Piezoelectric bender transducers for energy harvesting applications". In: *Energy Procedia* 14 (Jan. 2012). [Online; accessed 27. Nov. 2024], pp. 39–44. ISSN: 1876-6102. DOI: 10.1016/j.egypro.2011.12.894.

[100] Jan G. Smits, Susan I. Dalke, and Thomas K. Cooney. "The constituent equations of piezoelectric bimorphs". In: *Sens. Actuators, A* 28.1 (June 1991), pp. 41–61. ISSN: 0924-4247. DOI: 10.1016/0924-4247(91)80007-C.

[101] Yuanlin Hu, Xin Liang, and Wen Wang. "A theoretical solution of resonant circular diaphragm-type piezoactuators with added mass loads". In: *Sens. Actuators, A* 258 (May 2017). [Online; accessed 27. Nov. 2024], pp. 74–87. ISSN: 0924-4247. DOI: 10.1016/j.sna.2017.02.029.

[102] Jeong Woo Yi, Wan Y. Shih, and Wei-Heng Shih. "Effect of length, width, and mode on the mass detection sensitivity of piezoelectric unimorph cantilevers". In: *J. Appl. Phys.* 91.3 (Feb. 2002), pp. 1680–1686. ISSN: 0021-8979. DOI: 10.1063/1.1427403.

[103] Abhijeet M. Giri, S. F. Ali, and A. Arockiarajan. "Piezoelectric unimorph and bimorph cantilever configurations: Design guidelines and strain assessment". In: *Smart Mater. Struct.* 31.3 (Jan. 2022), p. 035003. ISSN: 0964-1726. DOI: 10.1088/1361-665X/ac47d5.

[104] Qing-Ming Wang et al. "Theoretical analysis of the sensor effect of cantilever piezoelectric benders". In: *J. Appl. Phys.* 85.3 (Feb. 1999), pp. 1702–1712. ISSN: 0021-8979. DOI: 10.1063/1.369314.

[105] W Li, TS Liu, and CC Hsiao. "A miniature generator using piezoelectric bender with elastic base". In: *Mechatronics* 21.7 (Oct. 2011). [Online; accessed 25. Nov. 2024], pp. 1183–1189. ISSN: 0957-4158. DOI: 10.1016/j.mechatronics.2011.07.004.

[106] Nurettin Sezer and Muammer Koç. "A comprehensive review on the state-of-the-art of piezoelectric energy harvesting". In: *Nano Energy* 80 (Feb. 2021). [Online; accessed 27. Nov. 2024], p. 105567. ISSN: 2211-2855. DOI: 10.1016/j.nanoen.2020.105567.

[107] Yang Xin et al. "Piezoelectric diaphragm as a high performance biosensor platform". In: *Appl. Phys. Lett.* 89.22 (Nov. 2006), p. 223508. ISSN: 0003-6951. DOI: 10.1063/1.2396919.

[108] Kaustav Roy, Joshua En-Yuan Lee, and Chengkuo Lee. "Thin-film PMUTs: a review of over 40 years of research". In: *Microsyst. Nanoeng.* 9.95 (July 2023), pp. 1–17. ISSN: 2055-7434. DOI: 10.1038/s41378-023-00555-7.

[109] Kaustav Roy et al. "A PMUT integrated microfluidic system for fluid density sensing". In: *Journal of Microelectromechanical Systems* 30.4 (2021), pp. 642–649.

[110] Kaustav Roy et al. "A pmut integrated microfluidic system for volumetric flow rate sensing". In: *2021 21st international conference on solid-state sensors, actuators and microsystems (Transducers)*. IEEE. 2021, pp. 172–175.

[111] Niall P. Macdonald et al. "Comparing Microfluidic Performance of Three-Dimensional (3D) Printing Platforms". In: *Anal. Chem.* 89.7 (Apr. 2017), pp. 3858–3866. ISSN: 0003-2700. DOI: 10.1021/acs.analchem.7b00136.

[112] Viraj Mehta and Subha N. Rath. "3D printed microfluidic devices: a review focused on four fundamental manufacturing approaches and implications on the field of healthcare". In: *Bio-des. Manuf.* 4.2 (June 2021), pp. 311–343. ISSN: 2522-8552. DOI: 10.1007/s42242-020-00112-5.

[113] Alvaro Mata, Aaron J Fleischman, and Shuvo Roy. "Characterization of polydimethylsiloxane (PDMS) properties for biomedical micro/nanosystems". In: *Biomedical microdevices* 7 (2005), pp. 281–293.

[114] *CUSA-TR65-065-2200-TH68 | DigiKey Electronics*. [Online; accessed 13. Nov. 2024]. Nov. 2024. URL: https://www.digikey.nl/en/products/detail/cui-devices/CUSA-TR65-065-2200-TH68/16579204.

[115] Hamid Asadi Dereshgi, Huseyin Dal, and Mehmet Emin Sayan. "Analytical analysis of a circular unimorph piezoelectric actuator in the range of low voltages and pressures". In: *Microsyst. Technol.* 26.8 (Aug. 2020), pp. 2453–2464. ISSN: 1432-1858. DOI: 10.1007/s00542-020-04786-w.

[116] R Munnig Schmidt, Georg Schitter, and Adrian Rankers. *The design of high performance mechatronics-: high-Tech functionality by multidisciplinary system integration*. Ios Press, 2020.

[117] L. B. Sharos et al. "Enhanced mass sensing using torsional and lateral resonances in microcantilevers". In: *Appl. Phys. Lett.* 84.23 (June 2004), pp. 4638–4640. ISSN: 0003-6951. DOI: 10.1063/1.1759379.

[118] T.D. Bakker. *Real-time monitoring of sweat of Cystic Fibrosis patients | TU Delft Repository*. [Online; accessed 7. Nov. 2024]. Nov. 2019. URL: https://repository.tudelft.nl/record/uuid:c483a44c-5414-441b-9cb2-599ceac2373c.

[119] Luis Teia Gomes. "Effect of damping and relaxed clamping on a new vibration theory of piezoelectric diaphragms". In: *Sens. Actuators, A* 169.1 (Sept. 2011). [Online; accessed 28. Nov. 2024], pp. 12–17. ISSN: 0924-4247. DOI: 10.1016/j.sna.2011.04.005.

[120] Yannick Le Bras et al. "Magneto-Elastic Resonance: Principles, Modeling and Applications". In: *Resonance*. Croatia: IntechOpen, Nov. 2017. ISBN: 978-953-51-3634-7. DOI: 10.5772/intechopen.70523.

[121] Craig A Grimes and Dimitris Kouzoudis. "Remote query measurement of pressure, fluid-flow velocity, and humidity using magnetoelastic thick-film sensors". In: *Sens. Actuators, A* 84.3 (Sept. 2000). [Online; accessed 29. Nov. 2024], pp. 205–212. ISSN: 0924-4247. DOI: 10.1016/S0924-4247(00)00306-X.

[122] Dimitris Kouzoudis and Craig A. Grimes. "Remote query fluid-flow velocity measurement using magnetoelastic thick-film sensors (invited)". In: *J. Appl. Phys.* 87.9 (May 2000), pp. 6301–6303. ISSN: 0021-8979. DOI: 10.1063/1.372686.

[123] Craig A. Grimes et al. "Theory, Instrumentation and Applications of Magnetoelastic Resonance Sensors: A Review". In: *Sensors* 11.3 (Mar. 2011), pp. 2809–2844. ISSN: 1424-8220. DOI: 10.3390/s110302809.

[124] John Bechhoefer et al. "Temperature dependence of the capacitance of a ferroelectric material". In: *Am. J. Phys.* 75.11 (Nov. 2007), pp. 1046–1053. ISSN: 0002-9505. DOI: 10.1119/1.2723801.

[125] Elain Fu. "Paper Microfluidics for POC Testing in Low-Resource Settings". In: *Applications of Microfluidic Systems in Biology and Medicine*. Singapore: Springer, Apr. 2019, pp. 325–352. ISBN: 978-981-13-6229-3. DOI: 10.1007/978-981-13-6229-3_12.

[126] Xian-He Huang et al. "The Exploration and Confirmation of the Maximum Mass Sensitivity of Quartz Crystal Microbalance". In: *IEEE Trans. Ultrason. Ferroelectr. Freq. Control* 65.10 (July 2018), pp. 1888–1892. DOI: 10.1109/TUFFC.2018.2860597.